University of Strathclyde Engineering

3D Biofabrication of Gelatin based Small Vascular Tissues

Yifei Wan

Supervisor: Prof. Will Shu

DEPARTMENT OF BIOMEDICAL ENGINEERING

University of Strathclyde

THE THESIS IS SUBMITTED IN PARTIAL FULFILMENT FOR THE DEGREE OF DOCTOR OF PHILOSOPHY IN BIOMEDICAL ENGINEERING

Contents

Declaration of Authenticity and Author's Rights

'This thesis is the result of the author's original research. It has been composed by the author and has not been previously submitted for examination which has led to the award of a degree.' 'The copyright of this thesis belongs to the author under the terms of the United Kingdom Copyright Acts as qualified by University of Strathclyde Regulation 3.50. Due acknowledgement must always be made of the use of any material contained in, or derived from, this thesis.'

Signed: Yifei Wan Date: March 20, 2025

Previously Published Material

Papers:

Denton, O., **Wan, Y**., Beattie, L., Jack, T., McGoldrick, P., McAllister, H., Mullan, C., Douglas, C. M., & Shu, W. (2024). Understanding the Role of Biofilms in Acute Recurrent Tonsillitis through 3D Bioprinting of a Novel Gelatin-PEGDA Hydrogel. Bioengineering, 11(3), 202.

Shi, J., **Wan, Y.,** Jia, H., Skeldon, G., Jan Cornelissen, D., Wesencraft, K., Wu, J., McConnell, G., Chen, Q., Liu, D., & Shu, W. W. Printing Cell Embedded Sacrificial Strategy for Microvasculature using Degradable DNA Biolubricant. Angewandte Chemie International Edition, e202417510.

Patent:

A novel hydrogel preparation process for Surgical meshes. (Published)

Poster presentations:

Y Wan, W Shu. (2023). Sacrificial hydrogel for 3D bioprinting branched microvasculature. Biomedical Engineering @Strathclyde. Day of Celebration, Glasgow

Manuscript in preparation:

Y Wan, W Shu. (2023). Freeze-dried dual crosslinking of gelatin with PEGDA.

Acknowledgements

Here, I would like to express my sincere gratitude to everyone who helped me with my PhD. It's a rough but memorable journal.

First, I would like to thank my supervisor, Prof. Will Shu, who gave me valuable advice and novel ideas during my PhD.

Next, I am also grateful to my colleagues and friends in the lab and office.

最后，我要感谢我的家人和朋友们。感谢他们无条件的支持和溺爱。

Special thanks to my Scottish family, Pili, Andy and my sweet boy AJ. Thanks for always keeping me a warm welcome. Special thanks to my furry friend, Dobbie.

Thanks to all my love. Tonight, we have the stars.

Abstract

The development of vascular structures is critical for advancing tissue engineering, particularly in addressing the challenges of small-diameter blood vessel (SDBV) fabrication due to the limitations in current materials and techniques. Gelatin, prized for its biocompatibility, and poly(ethylene glycol) diacrylate (PEGDA), valued for tunable crosslinking, have each been explored independently. However, the crosslinking for their combination and the fabrication methods have not been fully optimised for SDBV applications. This research introduces a novel gelatin-based biomaterial hybridised with poly(ethylene glycol) diacrylate (PEGDA) to fabricate small vascular structures that overcome current material and processing limitations. A novel freeze-drying technique enhanced mechanical properties and suitability for vascular tissue applications. The research explores the mechanical properties of gelatin/PEGDA hydrogels raising the dry-state Young's modulus of gelatin/PEGDA scaffolds to 100 MPa while porosity. Through a fast and easy method, rotational printing, this study demonstrates the feasibility of fabricating small vascular structures. The uniform tubes, measuring 0.7–2 mm in diameter with wall thicknesses of 200 μm, allow for leak-free perfusion under overpressures of 1000 mmHg. Besides, a microvasculture was attached with the small tubular structure, forming a multi-scale vascular structure. Additionally, the integration of the DNA hydrogel with 3D bioprinting technology enables the precise fabrication of complex vascular networks, breaking the limitation of the smallest vascular structure as small as 70 μm and forming confluent endothelial. This project contributes a versatile approach to small vascular tissue engineering by addressing material limitations and expanding the range of biomaterials and fabrication techniques that enable enhanced mechanical properties, biocompatibility, and functional integration with native tissues.

Keywords: small vascular tissue; 3D bioprinting; gelatin; poly(ethylene glycol) diacrylate (PEGDA)

Figures list

Tables list

Abbreviations list

Computed Tomography (CT)

Dynamic mechanical analysis (DMA)

Extracellular Matrix (ECM)

Elastin-like block polypeptides (ELP)

Expanded Polytetrafluoroethylene (ePTFE)

Gelatin Methacrylate (GelMA)

Human Coronary Artery Smooth Muscle Cells (HCASMC)

Human Umbilical Vein Endothelial Cells (HUVECs)

Magnetic Resonance Imaging (MRI)

Polycaprolactone (PCL)

Polyethylene Glycol Diacrylate (PEGDA)

Polyethylene Terephthalate (PET)

Polylactic Acid (PLA)

Poly(lactic-co-glycolic acid) (PLGA)

Polyglycerol Sebacate (PGS)

Polyurethanes (PU)

Small-Diameter Blood Vessels (SDBVs)

Solvent-Induced Phase Separation (SIPS)

Small Vessel Diseases (SVDs)

Tissue-Engineered Blood Vessel (TEBV)

University of Strathclyde Engineering

1. Introduction

1.1 Tissue Engineering for Vascular Structure

Arterial disease is a significant global health issue, causing a high death rate, with cardiovascular diseases accounting for approximately 17.8 million deaths annually worldwide and projections indicating an increase to over 23 million by 2030 (Amini et al., 2021; Zhao et al., 2019). As a vital part of the human body, the vascular structure serves as the primary network for transporting blood and nutrients. It ensures that different parts of the body function effectively and in unison. The distribution of vascular structures is extensive and reaches nearly every organ and tissue, where they play an essential role in supplying oxygen and nutrients while simultaneously removing waste products. Autologous bypass surgery remains the clinical standard but has limitations, including high morbidity and low availability (Amini et al., 2021). Some common synthetic materials like Polyethylene terephthalate (PET) and expanded polytetrafluoroethylene (ePTFE) have succeeded in larger vessels but failed in smaller ones due to low long-term patency and complications like thrombosis and lack of growth potential, particularly in vessels smaller than 6 mm in diameter. Researchers focus on improving small-diameter blood vessels (SDBVs) through advanced materials, fabrication techniques, surface modifications, and ensuring mechanical properties that match the host tissue to prevent graft failure.

In vascular tissue engineering, 3D bioprinting plays a pivotal role in revolutionising the field by enabling the precise fabrication of complex vascular networks that closely mimic natural vasculature. This technology facilitates the creation of patient-specific vascular grafts and provides an advanced platform for studying vascular biology, disease modelling, drug screening, and personalised medicine. However, despite its significant potential, several limitations remain. Current research highlights the lack of materials that simultaneously offer biocompatibility and adequate mechanical properties, as well as challenges in replicating the intricate geometry of the vascular system. Some researchers favour synthetic materials, overlooking the excellent biocompatibility of natural materials. The novel biomaterial which meets the requirements for small vascular structures is the key to expanding the application of 3D bioprinting in vascular tissue engineering.

1.2 The structure of the thesis

This PhD thesis focuses on fabricating small vessel structures using gelatin-based materials. Chapter One introduces the structure of this thesis. Chapter Two presents a literature review, mainly divided into bioprinting vessels and materials. It is about the current methods of manufacturing small vessels and the main material selection. **Chapter Three** presents the general methodology for this research, including mechanical strength tests of materials and cell cultures. Other notable methods are

scattered throughout each chapter. **Chapter Four** presents a rotational printing method, which verifies the feasibility of this approach for fabricating small vessels. **Chapter Five**, the main chapter of this study, demonstrates a novel crosslinking method of gelatin/PEGDA to achieve high-strength gelatin-based hydrogels. In **Chapter Six,** gelatin/PEGDA hydrogels were used to fabricate small tubular structures through rotational dipping printing, forming continuous endothelial networks along the tubes, validating their biocompatibility and potential for vascular tissue engineering. Besides, extrusion-based 3D bioprinting with DNA hydrogel as a sacrificial material enabled the creation of microvascular channels as small as 0.07 mm in diameter. **Chapter Seven** discusses and concludes this study, as well as outlines future work.

1.3 Innovations in this thesis

Discovering a novel approach that combines gelatin with PEGDA: The research aims to manufacture a hybrid hydrogel with enhanced mechanical properties by combining pure gelatin with PEGDA and using the freeze-drying technique. This novel approach may lead to a more robust and porous biomaterial for vascular structures.

Fabricating mini vascular structures for implantation: The ability to create mini vascular structures implanted into chips or substrates will improve in vitro testing models and improve organ transplantation's overall progress.

Integration of various techniques: By combining rod supporting and dipping and utilising a combination of materials, the study aims to establish a refined and adaptable method for fabricating vascular structures. The 3D bioprinting of vascular structures is tied to medical innovation and technological advancement.

By taking a comprehensive path that integrates various techniques and materials, the study can contribute to the field. From the novel combination of pure gelatin with PEGDA to the creation of small vascular structures, the research's innovative aspects promise to push the boundaries of what is currently achievable.

2. Literature review

In this chapter, previous research on small vascular vessel structures is reviewed, including the main techniques used to fabricate small vascular structures in blood vessel tissue engineering and the main materials used based on small vascular structures and characteristics.

2.1 Vascular structure and its requirements

2.1.1 Structure

Blood vessels, also known as vasculature, can be classified into three main categories based on their function and role in the circulatory system: arteries, veins, and capillaries (Seifu et al., 2013). Small vessel structures, which include arterioles, venules, and capillaries, are typically defined as micro-vessels with diameters less than 6 mm. Arteries are the most significant type responsible for carrying oxygen-rich blood away from the heart. Examples include the aorta and carotid arteries. Veins, often larger in diameter but with thinner walls than arteries, return deoxygenated blood to the heart; examples are the jugular and saphenous veins. Lastly, capillaries are the smallest vessels and connect arteries and veins, facilitating the exchange of oxygen, nutrients, and waste materials with surrounding tissues.

Typically, blood vessels are composed of three main layers, shown in Fig 1:

a. Tunica Intima: The innermost layer lined with endothelial cells.
b. Tunica Media: The middle layer containing smooth muscle cells.
c. Tunica Adventitia: The outer layer made of adventitial fibroblasts.

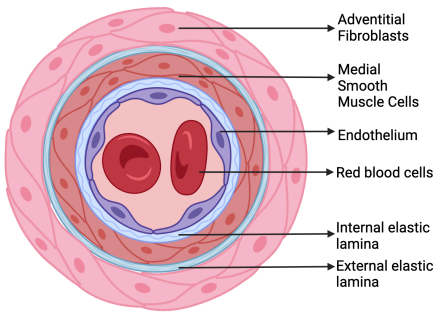

Figure 1 Blood vessel's structure

Blood vessels exhibit structural differences based on their size. Larger vessels, like arteries and veins, have thicker walls, more smooth muscle, and elastic tissue for strength and flexibility. Smaller vessels, such as arterioles, capillaries, and venules, have thinner walls and simpler structures, with

capillaries consisting only of endothelium to facilitate exchange processes (Table 1). Capillaries lack these distinct layers, and the thickness of each layer varies depending on the size and type of vessel (large, medium, or small arteries and veins). Blood vessel mechanical properties, such as compliance and elastic modulus, are essential for providing structural support and regulating blood flow (Yurdagul et al., 2016).

Table 1 Structural Comparison of Blood Vessels

	Diameter	Wall thickness	Endothelium	Elastic tissue	Smooth muscle	Fibrous tissue
Artery	0.1–10.0 mm	1.0 mm	Present	Moderate	Abundant	Small
Arteriole	10–100 μm	6.0 μm	Present	None	Moderate	None
Capillary	4–10 μm	0.5 μm	Present	None	None	None
Venule	10–100 μm	1.0 μm	Present	None	Small	Moderate
Vein	0.1–100.0 mm	0.5 mm	Present	Small	Moderate	Small

Diseases involving small vessels, collectively termed small vessel diseases (SVDs), significantly impact human health. SVDs are most commonly associated with cerebrovascular conditions, such as stroke and vascular dementia, but they also contribute to conditions like chronic kidney disease, hypertension, and diabetic microangiopathy. For example, cerebral small vessel disease accounts for approximately 25% of ischemic strokes and is a leading cause of age-related cognitive decline (Cheng et al., 2024; Pinter et al., 2015). Moreover, diabetic microvascular complications affect around 30% of individuals with diabetes, leading to kidney damage, retinopathy, and neuropathy (Aikaeli et al., 2022; Fowler, 2008). Despite the high prevalence and significant impact of small vessel-related diseases, research into small vessel structure in tissue engineering has historically lagged behind studies on large vessels, such as arteries and veins.

In contrast, small vessel research is still developing, particularly in addressing the challenges of mimicking the complex microarchitecture and function of capillaries and arterioles (Seifu et al., 2013). Creating stable, perfusable small vessel tissue is crucial for engineering large, functional tissues, but it remains an ongoing challenge, with fewer commercially available solutions compared to large vessel grafts. This gap highlights the need for increased focus on small vessel research, especially considering the widespread burden of SVD-related diseases. The development of small vessel engineering could bridge this gap and provide potential solutions to these clinical problems. However, several key hurdles must be overcome to ensure that engineered structures meet the specific requirements of the human small blood vessels.

2.1.2 Requirements

A major challenge is replicating the functional characteristics of natural small blood vessels, including appropriate mechanical properties and the ability to maintain long-term function under

physiological conditions. For engineered small blood vessels to be viable in a clinical setting, they must possess specific properties, such as sufficient strength to withstand blood pressure, biocompatibility to avoid immune rejection, and the ability to promote endothelialisation, i.e. the formation of a healthy endothelial lining on the inner surface of the vessel. A summary of the mechanical properties of human and artificial blood vessels is shown in Table 2. Together, these four properties —burst pressure, suture retention strength, ultimate tensile strength, and compliance—provide a comprehensive mechanical guide for fabricated vascular grafts. Burst pressure testing ensures the graft can withstand supraphysiological transmural loads without catastrophic rupture, while suture retention strength gauges the force required to pull a needle and thread through the wall—a critical indicator of surgical handling robustness. Ultimate tensile strength quantifies how much axial load the graft material endures before failing, reflecting its durability under pulsatile stretch, and compliance measures radial distensibility under physiological pressures, which must closely mimic native vessels (typically 10–20 % per 100 mmHg) to avoid flow disturbances or intimal hyperplasia. By benchmarking against these target values (>1,000 mmHg burst, >1 N suture pull-out, >1 MPa tensile strength), researchers can directly correlate deposition parameters (e.g. filament diameter, layer thickness, interstrand overlap) and post-processing treatments (crosslinking, annealing) with final graft performance.

Table 2 Mechanical properties of human and artificial blood vessels

Parameter	Definition	Test methods	Target/Reference Values	Citation
Burst pressure	The pressure at which one end of the vascular graft is closed and liquid is slowly and uniformly injected from the other end until the vessel expands and ruptures	Bursting tester	Desirable burst pressure > 1,000 mmHg. Natural blood vessels can withstand burst pressure exceeding 3,000 mmHg.	(Konig et al., 2009; L'Heureux et al., 2006)
Suture retention strength	Defined as the peak strength when the surgical wire is pulled out the wall of the tube	Universal tensile tester	Desirable suture retention strength exceeds 1 N.	(Bergmeister et al., 2013)
Ultimate tensile strength	The maximum stress that the vascular graft can withstand when stretched before rupture	Universal tensile tester	Desirable ultimate tensile strength is higher than 1 MPa.	(Konig et al., 2009; L'Heureux et al., 2006)
Compliance	The ability of the vascular graft to expand radially due to internal pressure	Compliance tester	Desirable compliance should match as closely as possible to natural blood vessels, with a value of 10%–20%/100 mmHg.	(Montini-Ballarin et al., 2016)

2.2 Biomaterials

When it comes to the biomaterial world, most researchers face an apparent dilemma (Fig 2): while natural materials are favoured for their biocompatibility, they often lack the necessary mechanical strength for long-term functionality. On the other hand, synthetic materials offer the required strength but struggle to replicate the complex biological functions of blood vessels. This trade-off between material strength and biological performance remains a critical challenge in developing small vascular structures and other tissue-engineered structures.

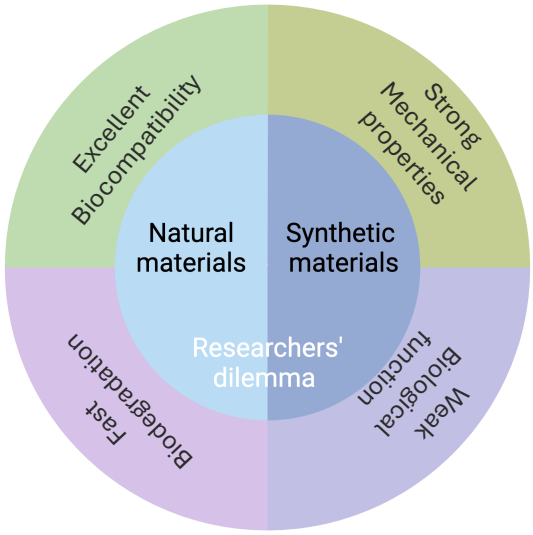

Figure 2 The researchers' dilemma in tissue engineering

Natural polymers, such as collagen and elastin, are ideal for constructing small vessel structures due to their compatibility with human tissues and biodegradability. These materials can effectively mimic the properties of the extracellular matrix, thus supporting cell attachment and proliferation. However, it is often challenging to meet the requirements in terms of mechanical properties using natural materials alone, so researchers usually compound them with synthetic polymers to enhance the mechanical strength of the materials (Liu et al., 2019). For small vessels, the mechanical properties of the tissue-engineered vascular grafts are critical for their long-term success, particularly when matching the host tissue's flexibility, strength, and elasticity.

2.2.1 Natural materials

Collagen is one of the most commonly used natural polymers. It is a major component of human tissues and has superior biocompatibility. Jiang et al. used collagen to fabricate transplanted arterial vasculature by electrospinning, and the grafts demonstrated an effective ability to promote the growth, migration, and proliferation of HUVECs (Jiang et al., 2017). To increase the burst pressure, the collagen was cross-linked with heparinisation. However, the rapid degradation limits the application of collagen.

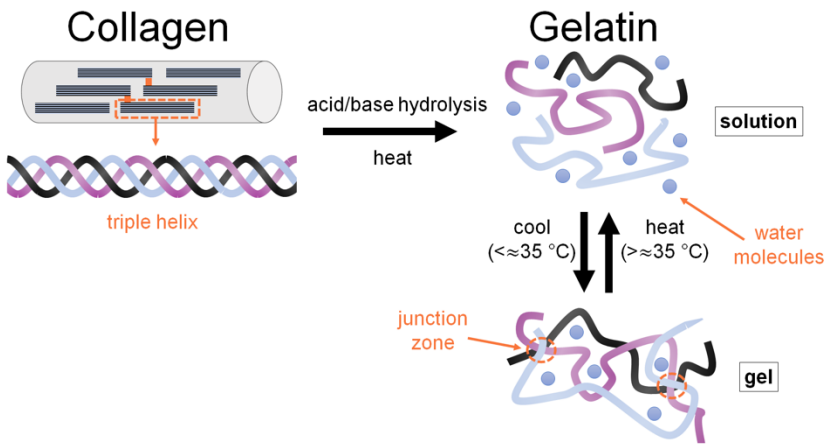

Figure 3 The chemistry of gelatin (from ChemBAM website)

Hydrolysed from collagen, gelatin is a highly water-soluble biopolymer. Depending on the pretreatment procedures of collagen I, two primary gelatin forms can be derived: type A (from acidic treatment) and type B (from alkaline or enzymatic treatment) (Fig 3). Consisting of approximately 20 amino acids connected via peptide bonds, gelatin has a molecular weight ranging between 15,000 and 400,000 Da. Its structure is dominated by the Gly-Pro-Hyp amino acid triplet, although the specific composition and sequence can differ widely based on its source, ultimately influencing its properties. Over the past decade, pig and bovine gelatin have been prominently used in regenerative medicine, notable for their polypeptide structures akin to human gelatin. In contrast, fish gelatin has fewer peptide repetitions, which results in distinct thermal properties and viscosities compared to mammalian gelatin (Andreazza et al., 2023; Echave et al., 2017).

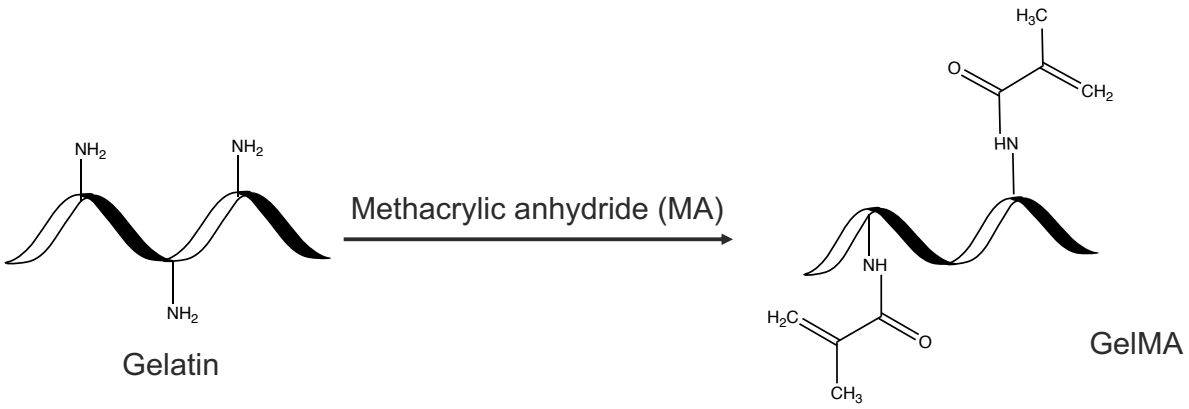

Figure 4 Synthesis of GelMA

To overcome gelatin's limitations, such as insufficient mechanical strength and temperature-sensitive transitions, many studies use chemical modifications that react with specific moieties, blend with other polymers, or do both simultaneously. One prominent approach to improving gelatin's mechanical properties is through chemical changes, such as methacrylation (Fig 4). Liu et al. (2017) developed gelatin methacryloyl (GelMA), significantly enhancing mechanical strength and structural

fidelity during bioprinting applications. The shear-thinning and self-healing properties of GelMA facilitate the creation of complex physiological microenvironments, demonstrating its potential in tissue engineering and regenerative medicine (Liu et al., 2017). This study highlights how chemical modifications can address gelatin's weaknesses by enabling bioprinting at lower concentrations while maintaining cell viability. Building on this, Gao et al. (2019) developed a composite hydrogel by integrating GelMA with a cleavable polyethylene glycol-based polymer. This hybrid hydrogel exhibited not only enhanced mechanical strength but also tunable degradation properties, making it particularly suitable for load-bearing tissue applications such as cartilage or bone repair. Their study demonstrated that the dual-crosslinking strategy—comprising both photopolymerisation and enzyme-cleavable bonds—offered a balance between structural integrity and controlled resorption, thereby addressing two major challenges in designing biomaterials for mechanically dynamic environments. In another study, Gao et al. (2019) showcased the development of a hydrogel using GelMA combined with a cleavable polymer, resulting in improved mechanical properties suitable for load-bearing applications. The cross-linking of GelMA stabilises the hydrogel network, allowing for tunable biodegradability and enhanced strength, emphasising the benefits of chemical modifications in creating advanced biomaterials for tissue repair (Gao et al., 2019).

Alginate, a natural polysaccharide sourced from brown algae, is one of the common biomaterials for biomedical uses due to its biocompatibility, capacity to form hydrogels and adaptability for modification. Alginate hydrogels can be created by crosslinking with divalent cations like calcium, magnesium, or barium ions (Fig 5). Gao et al. (2015) showcased the effectiveness of coaxial printing that employs alginate-based bioinks to produce vascular structures essential for facilitating blood flow and nutrient transfer in tissue engineering (Gao et al., 2015). Besides, Gao et al. (2020) presented a hybrid bioink featuring alginate, which serves as a supportive matrix for endothelial progenitor cells. This hybrid strategy fosters cell growth and transports therapeutic agents to ischemic sites, underscoring the promise of alginate-based scaffolds in treating vascular diseases.

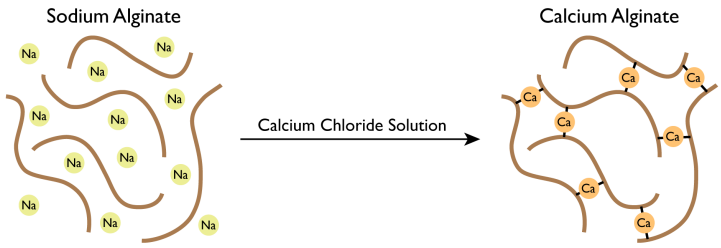

Figure 5 Crosslinking of Sodium Alginate

Silk fibroin (SF) is a fibrous protein from silkworm cocoons. It exhibits high tensile strength, tailorable biodegradability, and low inflammatory profile. In TEVGs, SF provides a robust scaffold that can be engineered for elasticity and cell compatibility (Maleki et al., 2022). It is less thrombogenic than many synthetics and supports endothelial cell adhesion when properly modified. SF's mechanical

properties can approach those of native vessels. Electrospun SF grafts can achieve the burst pressure and suture retention required for arteries while supporting cell growth. Blending SF with elastic or bioactive components can improve compliance. For example, Yang et al. (2024) electrospun composite scaffolds of SF and fibrin (various ratios). The optimal SF/fibrin scaffold had higher tensile strength than pure fibrin, yet retained excellent blood compatibility and supported mesenchymal stem cell growth. Inspired by native elastin's elasticity and bioactivity, self-assembling elastin-like block polypeptides (ELP) have been engineered into nanofibrous scaffolds. Natsume et al. (2023) demonstrated that modified ELP nanofibers inhibit platelet adhesion, promote endothelial proliferation, and maintain smooth-muscle contractile phenotype—key properties for hemocompatible small grafts.

Some biomaterials can be used as sacrificial material for fabricating the vascular network; for example, agarose, a biopolymer derived from seaweed, is known for its biocompatibility and ability to form hydrogels. Bertassoni et al. (2014) highlighted the significant role of agarose in developing vascular networks within engineered tissue constructs. Their research demonstrated the efficacy of bioprinted agarose template fibres in creating microchannel networks embedded within photocrosslinkable hydrogels (Bertassoni et al., 2014). The successful formation of endothelial monolayers within these channels underscores the utility of agarose in enhancing cell viability and differentiation, making it a valuable material for complex tissue engineering applications.

Some biomaterials play a role in enhancing the performance of the small vessel structure as incorporated with hybrid hydrogel. Elastin is one of the candidates, a vital extracellular matrix protein, and is known for its elasticity and resilience, essential in the design of vascular grafts. As highlighted by Hasan et al. (2014), incorporating elastin or elastin-like peptides into the design of vascular grafts significantly improves the adhesion and function of endothelial cells, resulting in increased haemocompatibility and reduced risk of thrombosis (Hasan et al., 2014). This is particularly important for small-diameter vessel structures, as establishing the endothelial layer is critical to the success of the blood vessel structure (Radke et al., 2018; Ren et al., 2015).

2.2.2 Synthetic material

Synthetic material is widely utilised in vascular grafts, particularly for medium to large diameters. However, it has shown inadequate performance in small-diameter vessels like PET, ePTFE. Radke et al. (2018) emphasise that the inflammatory responses elicited by PET can significantly hinder endothelialisation, which is crucial for the long-term success of vascular grafts (Radke et al., 2018). This indicates that although PET is useful for larger vessel structures, its application in smaller contexts poses challenges, highlighting the need for further investigation into appropriate alternatives.

Poly(ε-caprolactone) (PCL) is a semi-crystalline, aliphatic polyester known for its excellent biocompatibility, slow biodegradation (over months to years), and FDA approval for certain

implantable devices. PCL presents a promising biodegradable alternative for small-diameter vascular structures. Its low melting point (~60 °C) and good solubility allow fabrication via electrospinning, melt electrowriting (MEW), and 3D printing. Its favourable mechanical properties and slow degradation rate make it an attractive candidate for tissue engineering applications. Recent research on PCL fabrication for small vascular structures through electrospinning has shown remarkable results. Furthermore, incorporating PCL with other materials has been shown to enhance scaffold performance, which is crucial for developing effective small vessel structures (Norotte et al., 2009; Skardal et al., 2010). However, the hydrophobic nature of PCL tends to reduce cell adhesion because most cells prefer more hydrophilic surfaces for attachment.

Beyond PCL, several other fully synthetic polymers have shown promise for small-diameter vascular grafts. Segmented polyurethanes (PU) are block copolymers combining hard and soft segments to yield elastomeric materials with tunable strength, compliance, and excellent fatigue resistance. Their elasticity closely matches that of native arteries, and they can be electrospun into nanofibrous scaffolds. Surface modifications (e.g., sulfated alginates) reduce thrombogenicity and encourage endothelialisation (Amiri Heydari et al., 2024). Additionally, Poly(lactic-co-glycolic Acid) (PLGA) and Polylactic Acid (PLA) can provide initial mechanical integrity and are amenable to electrospinning or 3D printing. Poly (glycerol sebacate) (PGS) has emerged as a new potential in TEVGs. Its high elasticity and rapid in vivo degradation allow host cells to remodel the graft into a neoartery rich in collagen and elastin. A pure PGS tube reinforced by an external PGA braid was implanted in rats. After 3 months, the constructs transformed into neoarteries with ECM composition and organisation comparable to native aorta and elicited minimal inflammatory response (Fukunishi et al., 2022).

Polyethylene Glycol Diacrylate (PEGDA) is a synthetic polymer known for its non-immunogenic and hydrophilic properties, which contribute to its application in hydrogel formation. Bahney et al. (2011) demonstrate that PEGDA can effectively support cell viability and functionality in tissue engineering applications. Using PEGDA with other materials, such as hyaluronic acid (HA), further enhances its mechanical and biological properties, making it a strong candidate for small-diameter vessel structures (Shanjani et al., 2015). The versatility of PEGDA, particularly in the context of bioprinting and hybrid constructs, indicates its potential for creating complex tissue scaffolds that mimic natural tissue behaviour (Guarino et al., 2013). The development of bioinks incorporating both GelMA and PEGDA has been of significant interest in the field of 3D bioprinting. Moreover, Gao et al. (2019) reported improved mechanical properties and cell adhesion in GelMA/PEGDA hydrogels, specifically for guided bone regeneration applications (Gao et al., 2019). The study underscores the importance of this combination in enhancing the performance of tissue engineering materials. Similarly, the work by Wang et al. (2018) reiterates the advantages of GelMA/PEGDA hydrogels, confirming their effectiveness in supporting cell viability and improving mechanical performance (Wang et al., 2018).

2.2.3 Summary

Combining natural and synthetic materials is common when selecting biomaterials, with the cross-linking strategy being a key consideration. GelMA and PEGDA are frequently used together due to their compatibility with UV-induced free radical polymerisation, a common cross-linking technique (Chen et al., 2023). Irgacure 2959, a vital photoinitiator in such processes, is gaining recognition in biomedical applications like 3D bioprinting and hydrogel formation. Its ability to absorb UV light (365 nm) and produce free radicals facilitates the polymerisation of acrylate and methacrylate groups, forming crosslinked hydrogels (Fig 11). With low toxicity and water solubility, Irgacure 2959 is ideal for bioink development involving living cells.

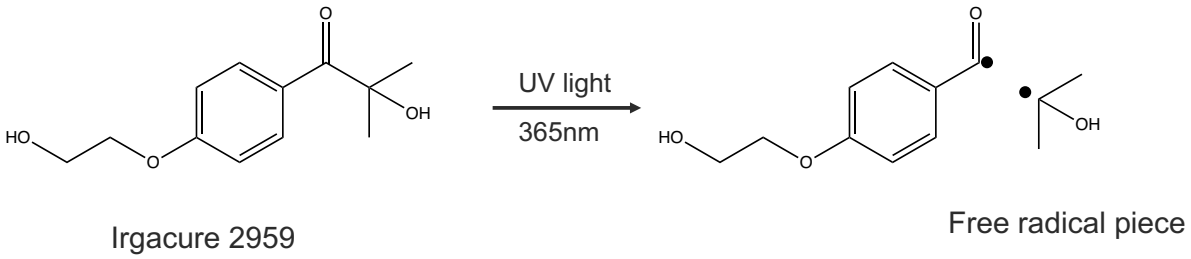

Figure 6 The free radical polymerisation started from Irgacure 2959

Under ultraviolet light excitation, Irgacure 2959 undergoes photolysis, resulting in the generation of free radicals. These radicals initiate a chain reaction by attacking the carbon-carbon double bonds in GelMA and PEGDA, forming new carbon-carbon bonds while creating additional free radicals. These newly formed radicals subsequently propagate the reaction by attacking other carbon-carbon double bonds, facilitating the crosslinking process (Fig 12).

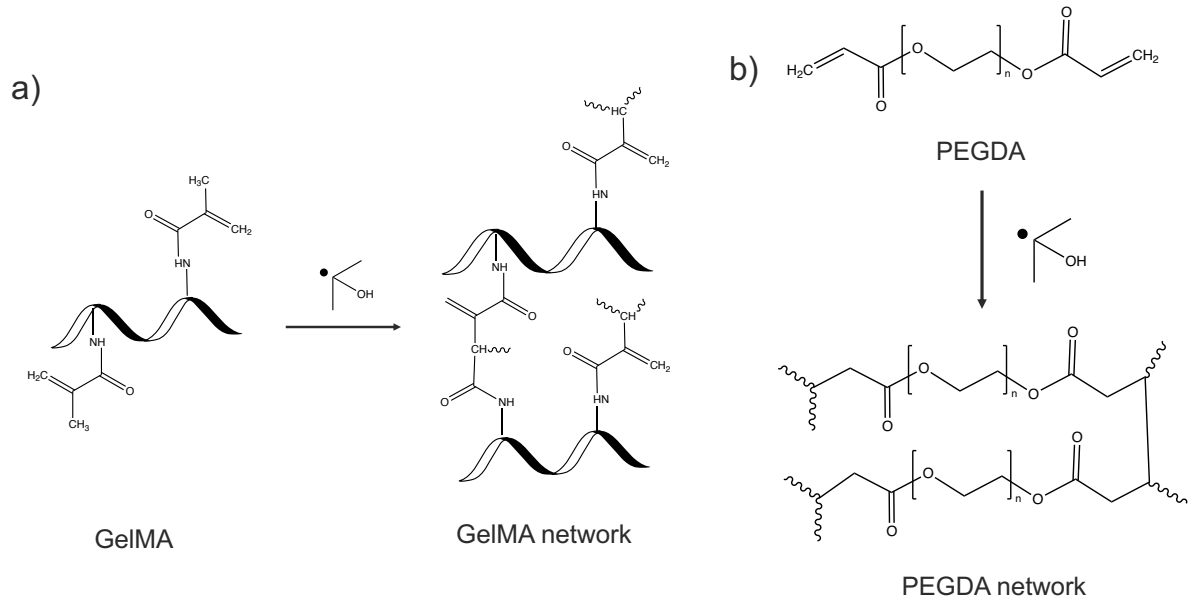

Figure 7 GelMA a) and PEGDA b) polymer network

When GelMA and PEGDA hydrogels are mixed, the free radicals generated during polymerisation allow their monomers to interact, forming a unique single cross-linked network composed of both monomers. This approach eliminates phase boundaries, unlike double cross-linked networks that rely on distinct polymer components, resulting in a more uniform and mechanically robust material, but wastes the advantage of the hybrid hydrogel. Gelatin, the precursor to GelMA, is an essential natural biomaterial with high biocompatibility. At room temperature, gelatin undergoes physical crosslinking through hydrogen bonding with water molecules; however, these bonds dissociate with increasing temperature, transforming the gelatin into a liquid. Stabilising the crosslinked network of gelatin and PEGDA is critical to address this limitation. The study aims to retain gelatin's intrinsic biocompatibility while leveraging PEGDA's chemical crosslinking to enhance mechanical performance, ultimately advancing the design of hybrid hydrogels for biomedical use.

When selecting materials, in addition to considering tensile mechanical strength to meet the burst pressure and tensile strength of small blood vessels, researchers should also consider rheological and dynamic properties, such as viscoelasticity, shear thinning, and surface rheology. Specifically, viscoelasticity describes the combined elastic (solid-like) and viscous (fluid-like) response of a material during deformation. In a purely elastic solid, stress is proportional to strain and recovery is instantaneous; in a purely viscous fluid, stress is proportional to strain rate and deformation is permanent. Native arteries are not perfectly elastic; they suppress pulsatile pressure waves and protect downstream microvessels. Grafts that are excessively stiff or lack viscous damping can cause wave reflections, leading to increased stress at the anastomosis and potentially resulting in intimal hyperplasia. Piszko et al. (2022) used Dynamic mechanical analysis (DMA) to show how varying crosslinking time in poly(glycerol sebacate) (PGS) elastomers tunes storage and loss moduli: longer cures raised both E′ (up to $\approx$1 MPa) and shifted tan δ peaks, demonstrating a route to match arterial viscoelasticity (Piszko et al., 2022). Non-Newtonian shear-thinning behaviour refers to fluids whose apparent viscosity decreases as the applied shear rate increases. In other words, under higher flow or agitation, the fluid "thins" and flows more easily, then recovers its viscosity when the stress is removed. Shear-thinning is a key characteristic in extruded printing. In extrusion-based printing, inks must flow under the high shear in nozzles but rapidly recover solidity ("shape-fix") once deposited to form fine lumens without collapse. After embedded with cells, lower viscosity under shear reduces shear-induced cell stress during printing or injection. Besides, surface dynamics refers to the time-dependent interfacial behaviours of a material's luminal surface when in contact with blood or physiological fluids. In small-diameter vascular grafts, these dynamics critically influence hemocompatibility and long-term patency. The luminal surface must minimise platelet activation under high shear. Micro- and nano-texturing (e.g. aligned electrospun fibres) help establish a lubricious, endothelialised lining that maintains low-friction flow (Amiri Heydari et al., 2024). Major et al. (2022) used a cone-and-plate analyser to apply controlled

wall shear stresses (0.3–7 Pa) to polymer films, measuring dynamic detachment of adhered blood cells and quantifying the interfacial viscoelastic response that correlates with thrombosis risk (Major et al., 2022).

2.3 The current manufacturing strategies of the artificial vessel

The foundation of vascular tissue engineering can be traced to the creation of synthetic vascular grafts in the mid-20th century. In the 1950s and 1960s, materials like Dacron and expanded ePTFE were introduced for large-diameter vascular grafts (Chan and Leong, 2008). However, these synthetic options encountered significant issues in small-diameter vessels (under 6 mm) due to thrombosis and insufficient biocompatibility. The 1980s and 1990s signalled the initial application of tissue engineering principles to develop small vessel structures. In 1986, Weinberg and Bell were the first to report their attempts to design in vitro tissue-engineered blood vessel (TEBV) using collagen gel scaffold and bovine aortic cells (Weinberg and Bell, 1986). In 1993, Langer and Vacanti raised the broader concept of tissue engineering by integrating biodegradable scaffolds with cellular biology to regenerate tissues (Langer and Vacanti, 1993). This approach provided the theoretical framework for subsequent advancements in vascular tissue engineering. Researchers began investigating natural biomaterials and cellular components to enhance the functionality and integration of vascular grafts. A more natural and functional vessel structure could be achieved by developing scaffolds using collagen and other biopolymers infused with endothelial cells. The technology for manufacturing small vessel structures in tissue engineering has two main categories based on the resource of the scaffold: decellularisation and scaffold-based techniques. Decellularisation is a process used in tissue engineering that involves removing all cellular components from a tissue while preserving the extracellular matrix (ECM). In scaffold-based techniques, different biomaterials are applied using various methods, including 3D printing and electro-spinning.

2.3.1 Decellularisation

In small vessel engineering, decellularisation involves removing cells from donor blood vessels (human or animal vessels) while preserving the ECM (Fig 8). This provides a natural scaffold for regenerating new cells, promotes biocompatibility, and reduces the risk of immune rejection. The diameter mostly ranges from 1.5 mm to 6 mm (Ding et al., 2024). It also addresses the challenges of creating functional, small-diameter vascular grafts prone to thrombosis and neointimal hyperplasia. The acellular small vessel structure includes superior biocompatibility and reduced immunogenicity. The process minimises the risk of immune rejection, as the cellular antigens that trigger a host response are removed.

Furthermore, the ECM retains essential structural proteins, such as collagen and elastin, which support the attachment and proliferation of new cells, promoting rapid endothelialisation and integration

with host tissues. However, the drawbacks of decellularisation include potential mechanical instability, as the process may weaken the ECM, affecting the vessel structure's ability to withstand physiological pressures. Lu et al. prepared elastic scaffolds from the aorta of adult pigs and showed that the removal of the collagen network can maintain the compliance of the native aorta, but it is less elastic than that of the fresh artery (Lu et al., 2004). Besides, incomplete decellularisation can also lead to residual cellular debris, which might provoke an immune response (Mancuso et al., 2014). Additionally, decellularised vessels are prone to thrombosis and neointimal hyperplasia, where excessive tissue growth can cause vessel blockage, limiting long-term patency.

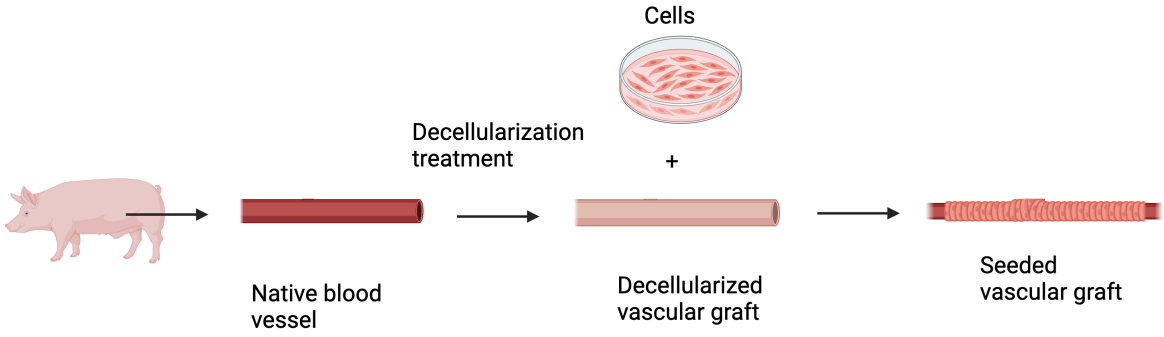

Figure 8 Decellularization and Recellularization Process for Vascular Graft Engineering

2.3.2 Cast

Mould casting is a well-established technique in tissue engineering used to fabricate small vessel scaffolds by casting polymers or gels into vascular moulds (Fig 9). One of the earliest successful examples of this approach was reported by Weinberg and Bell in 1986, who developed the first tissue-TEBV, mimicking all three histological layers of an artery (Weinberg and Bell, 1986). They used a collagen-coated Dacron mesh scaffold, onto which they seeded cultured bovine aortic endothelial cells, smooth muscle cells, and adventitial fibroblasts. The medial layer was cast with collagen mixed with smooth muscle cells and culture media, while adventitial fibroblasts were applied for mechanical support by embedding them in the Dacron mesh. This process resulted in a contiguous endothelial lining that acted as a large-molecule permeability barrier and exhibited biochemical activity, including the production of von Willebrand factor and prostacyclin. Although this method successfully formed a vessel with a functional endothelium, it achieved a burst strength of only 120–180 mmHg, far below the physiological requirement of 2000–3000 mmHg observed in human vessels (Konig et al., 2009).

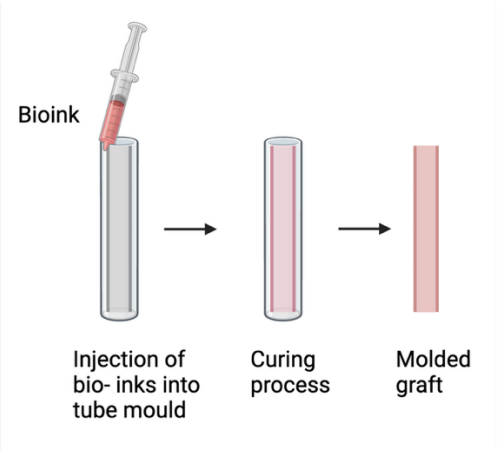

Figure 9 Mould casting for Vascular Graft Engineering

Mould casting offers several advantages in the fabrication of vascular grafts, including its simplicity, cost-effectiveness, and ability to produce vessels with complex geometries. For instance, Syedain et al. employed this technique to fabricate fibrin-based scaffolds seeded with fibroblasts, which, after dynamic conditioning, achieved burst pressures as high as 4,200 mmHg, significantly improving their mechanical strength (Syedain et al., 2014). However, one of the major limitations of early mould-cast scaffolds, as seen in the study by Weinberg and Bell, was the low initial burst strength, which was only a fraction of what is needed for clinical use (Weinberg and Bell, 1986). Additional post-processing steps, such as long-term dynamic culture or the incorporation of reinforcing materials like braided fibres, are often necessary to enhance the mechanical properties. Guan et al. demonstrated that embedding braided PET fibres into a hydrogel scaffold improved the graft's mechanical integrity, though the reinforcement reduced overall compliance (Goudie et al., 2023). Thus, while mould casting remains a versatile method, improving the balance between mechanical strength and biological function remains challenging.

2.3.3 Rod dipping

An efficient method for constructing vascular tissues involves using a rod that is alternately dipped into a cell-infused hydrogel. This repeated dipping creates multiple layers, potentially consisting of various hydrogels (Fig 10). Tabriz et al. employed this technique to produce layers incorporating viable human embryonic kidney and mouse fibroblast cells. Each layer's thickness ranged from 126 to 220 µm, determined by the wettability of the coated surface and the composition of the hydrogel applied before cross-linking. The authors suggest their method could be adapted for various vascular tissue types (Ghanizadeh Tabriz et al., 2017). Wilkens et al. built on this methodology by introducing motors to rotate the dip rods, enhancing control over the layer thickness. The thinnest layer achieved was approximately 25 µm, significant as it corresponds to the medial collagen and smooth muscle cell layers found in native arterial tissue (Wilkens et al., 2016).

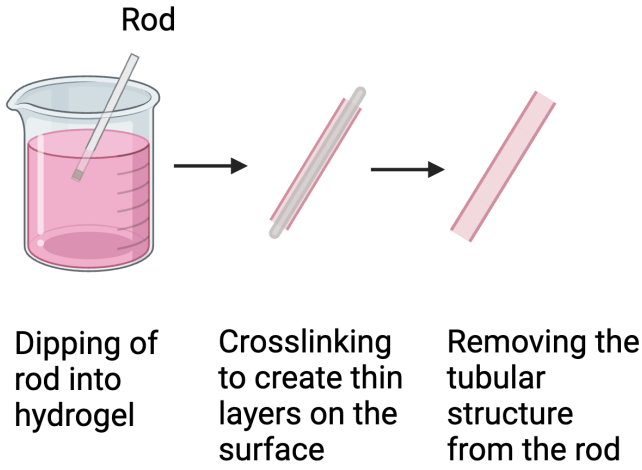

Figure 10 Dipping cast for Vascular Graft Engineering

2.3.4 3D printing

3D printing, particularly in vascular tissue engineering, refers to an additive manufacturing technique that constructs small vessel scaffolds by sequentially depositing biomaterial layers (Fig 5). This method is advantageous for creating complex geometries that replicate the natural curvature and branching of blood vessels. The process involves using bioinks, which typically consist of a combination of natural or synthetic polymers, cells, and hydrogels, allowing for the development of functional, tissue-like structures. In vascular graft fabrication, 3D printing facilitates high precision in scaffold design, enabling the accurate recreation of native arteries using magnetic resonance imaging (MRI) or computed tomography (CT) data, which can be imported into computer-aided design software. Unlike conventional mould-based techniques, 3D printing offers the ability to produce patient-specific scaffolds, making it a promising tool for personalised medicine. Several 3D printing techniques have been developed to fabricate small vessels, including extrusion 3D printing, stereolithography, and coaxial 3D printing.

Extrusion 3D printing is another common technique, where bioink is extruded through a nozzle to build up the scaffold layer by layer (Fig 11). This technique utilises various bioinks and fabrication methods to create functional vascular grafts with enhanced structural and biological properties. One study tested a catechol-functionalized Gelatin Methacrylate (GelMA/C) scaffold embedded with human coronary artery smooth muscle cells (HCASMC), where the internal and external layers were printed using different bioinks. The GelMA/C layer, combined with HCASMCs, showed reduced degradation compared to standard GelMA after 16 weeks of implantation in mice. Inflammatory responses diminished over time, and the scaffold became encapsulated in fibrotic tissue, with vascularisation observed by six weeks post-implantation (Cui et al., 2019). Similarly, a bilayer vascular construct developed at Soochow University used GelMA bioinks with hyaluronic acid to encapsulate human

umbilical vein endothelial cells (HUVECs) in the internal layer and smooth muscle cells (SMCs) in the external layer. This construct achieved a tensile strength of 12 kPa, with high cell proliferation and distinct layer-specific markers detected after seven days (Xu et al., 2020). Another approach utilised a gelatin-fibrinogen bioink with fibroblasts, printed using a rotary three-axis bioprinter, which showed enhanced burst pressure (1,110 mmHg) and realignment of fibroblasts after 45 days of culture. The printed grafts also demonstrated significant structural and mechanical stability over the course of two months (Freeman et al., 2019). However, extrusion is rugged because of low resolution (hundreds of micrometre extrusion needle) and low cell viability (due to shear damage from ink extrusion) (Norotte et al., 2009; Skardal et al., 2010).

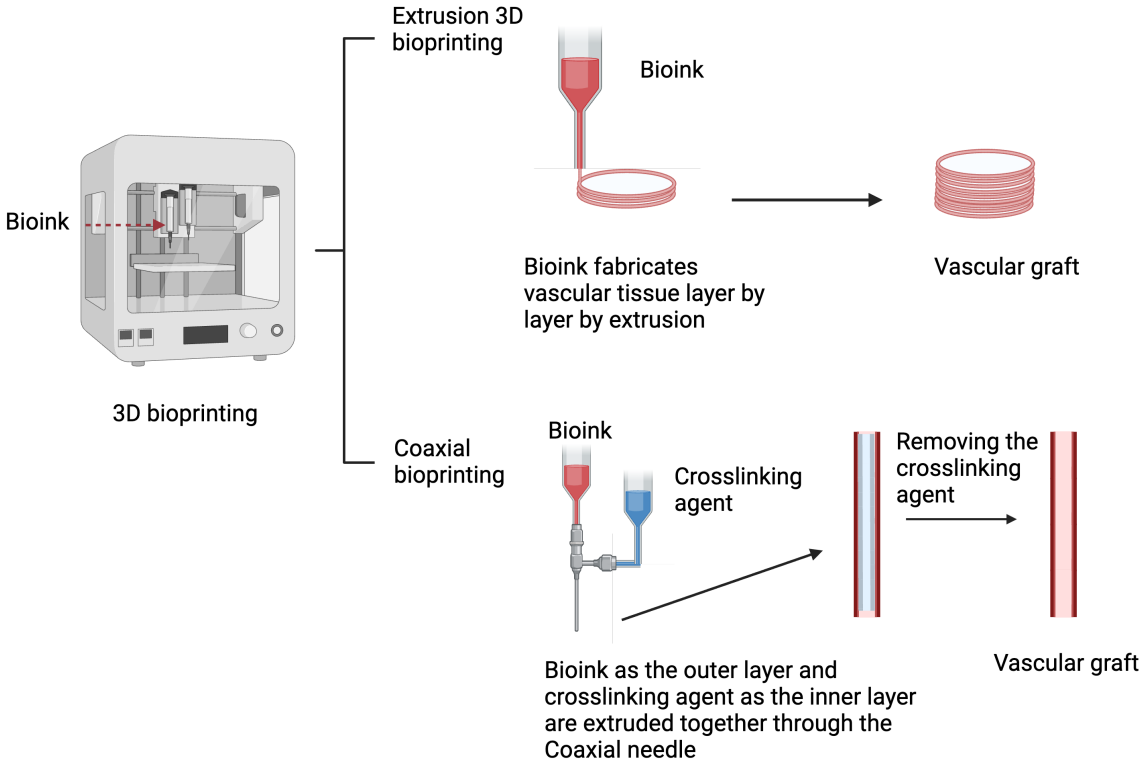

Figure 11 Two types of 3D bioprinting for Vascular Graft Engineering

Coaxial bioprinting is another method where a concentric nozzle creates a vascular structure with distinct inner and outer layers (Fig 11). For example, one study bioprinted a vascular graft using human umbilical vein SMCs embedded in alginate as the outer layer, with calcium chloride crosslinking in the inner layer, producing a 0.65 mm thick graft (Norotte et al., 2009). Triple coaxial bioprinting creates biomimetic blood vessels by combining vascular smooth muscle cells and vascular tissue-derived extracellular matrix for the media layer, with alginate and endothelial cells for the intima layer. After 3 days of static culture and 2 weeks of pulsatile maturation, constructs achieved good endothelialisation, and in vivo testing in rats showed patency for 3 weeks (Gao et al., 2019). The

technique improved further with an adventitia layer bioprinted into a pre-gel bath with fibroblasts, yielding a complete three-layer vessel (Kolesky et al., 2016).

2.3.5 Electrospinning

Electrospinning has emerged as a key technique in tissue engineering for the fabrication of nanofibrous scaffolds that mimic the natural extracellular matrix (ECM). This process involves the application of high voltage to a polymer solution, generating fibres that can be collected to form a scaffold with customisable architecture and fibre diameter (Fig 12). Recent advancements have enhanced electrospinning by enabling the co-spinning of multiple materials and producing complex structures, such as hollow fibres, which further increase its potential for use in tissue regeneration applications. The electrospinning's ability to control fibre size and porosity makes it an attractive approach for creating vascular grafts that support cell adhesion and proliferation while mimicking the mechanical properties of native tissues.

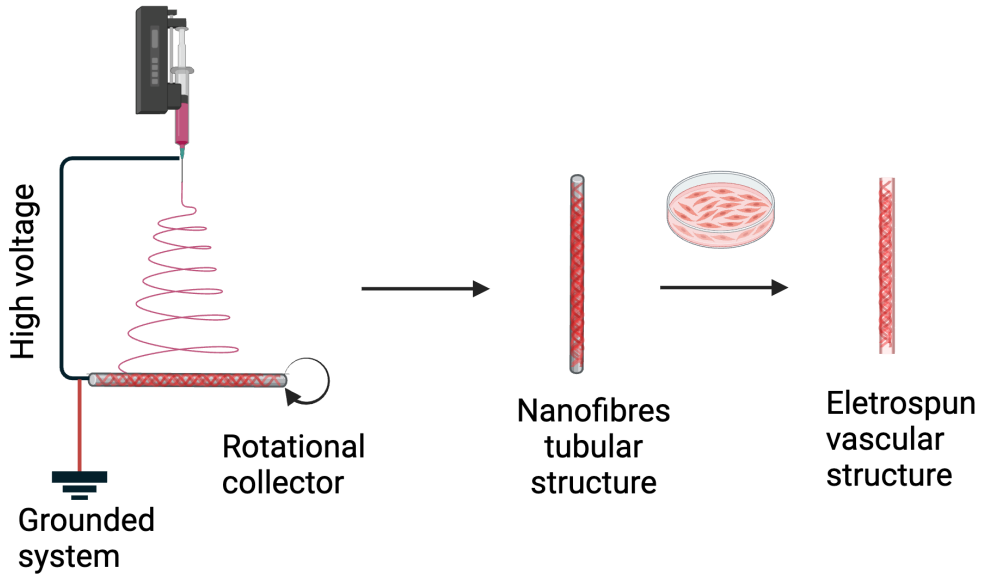

Figure 12 Electrospinning for Vascular Graft Engineering

Electrospun scaffolds have been widely explored in vascular graft development due to their mechanical tunability, biocompatibility, and cost-effectiveness. For example, polycaprolactone (PCL) blended with chitosan has shown promising results in producing SDBVs with anti-thrombogenic properties and enhanced endothelialisation (Rocha Neto et al., 2022). Studies have demonstrated that varying the chitosan concentration allows for fine-tuning of mechanical resistance and compliance, addressing the haemodynamic needs of vascular conduits. Moreover, composite materials, such as Polyglycerol sebacate (PGS) with tropoelastin, have been explored to mimic the non-linear mechanical behaviour of native arteries. While these constructs closely replicate specific properties of natural vessels, the challenge of creating consistent mechanical performance across different polymer blends

remains (Wang et al., 2024). Despite the benefits of electrospinning in vascular tissue engineering, several challenges persist. One significant limitation is the small pore size of electrospun scaffolds, which restricts cellular ingrowth and limits effective tissue integration. Maleki et al. (2022) fabricated a bilayer 4 mm graft with an inner co-electrospun SF/thermoplastic polyurethane (TPU) layer (loaded with heparin) and an outer chitosan/gelatin hydrogel. The inner SF fibres imparted high strength (burst pressure $\approx$1140 mmHg, suture retention ~6.7 N) and quickly formed an endothelial monolayer in vitro. The heparinised SF fibres significantly reduced platelet adhesion, improving hemocompatibility. The outer porous hydrogel supported smooth muscle cell (SMC) infiltration, mimicking a two-layer vessel wall..

Additionally, the chemical solvents used in the electrospinning process can leave behind toxic residues, posing a risk to biocompatibility. Further advancements in material composition and processing techniques, such as the use of biodegradable polymers like PCL or Poly(lactic-co-glycolic acid) (PLGA), have shown potential to overcome these barriers. However, variability in burst pressure and long-term mechanical performance in vivo continues to be a major concern, necessitating further research to optimise the electrospun scaffolds for clinical applications.

2.3.6 Summary

Manufacturing technologies play a critical role in the fabrication of vascular structures, especially in fields such as tissue engineering and vascular graft development, where the inner diameter of the structure is vital for mimicking natural biological conditions. The 1-6 mm diameter range is particularly significant for these applications because it aligns with the size of small to medium blood vessels, frequently targeted in regenerative medicine. In reviewing the various technologies available for this purpose, it becomes evident that most of them are capable of producing vascular structures within this diameter range, but each has specific advantages and limitations depending on the material properties and the intended application.

Different technologies impose distinct material requirements. For instance, 3D extrusion printing is a powerful tool in the creation of complex geometries; however, it requires bioinks with shear-thinning properties to ensure smooth extrusion and precise deposition. Shear-thinning bioinks behave in a way that allows them to flow more easily under pressure, which is critical for maintaining structural integrity during printing. This limits the range of materials that can be used in 3D extrusion, particularly in applications where mechanical strength or biocompatibility may be paramount. Conversely, electrospinning, another widely used technology, is particularly suited for producing polymerised fibres that mimic the extracellular matrix of tissues. Electrospun fibres have nanoscale dimensions, which are ideal for cell attachment and proliferation, but this method often requires specific polymer solutions that may not be suitable for all tissue engineering applications (Khalili and Ahmad,

2015; Yang et al., 2024). Additionally, the mechanical properties of electrospun materials, though beneficial for some applications, may not be strong enough for vascular grafts or load-bearing tissues.

Given these material-specific limitations, it is essential to select a fabrication method that offers versatility while minimising operational complexities. In this context, casting emerges as a particularly advantageous option. Casting is a simple, rapid, and flexible manufacturing technique that can accommodate a wide range of materials, including hydrogels, polymers, and composites. Unlike 3D extrusion printing and electrospinning, casting does not impose stringent material requirements such as shear-thinning behaviour or polymer compatibility (Ghanizadeh Tabriz et al., 2017). Instead, it relies on the physical process of pouring a liquid material into a mould and allowing it to solidify. This makes casting particularly suitable for working with materials that may not be easily processed through other methods, such as brittle hydrogels or hybrid materials that combine organic and synthetic components.

One of the key benefits of casting is its ability to produce uniform vascular structures with high precision, which is crucial for applications requiring consistent mechanical and biological performance. For instance, research has shown that casting methods can produce vascular grafts with excellent structural integrity and minimal variability in wall thickness, leading to better performance in vivo. Furthermore, casting allows for the incorporation of various additives, such as growth factors or reinforcing fibres, which can enhance the mechanical properties and bioactivity of the final product. Studies have demonstrated that the inclusion of braided fibre reinforcements within cast hydrogels can significantly improve their compliance and burst pressure, making them more suitable for load-bearing applications.

In 3D bioprinting methods, the rod is a common element for easily creating hollow structures. Conventional tissue engineering often uses models or mandrels to cast, roll, or dip tubular structures (Holland et al., 2018). For the fabrication of the tubular structure, a simplified, efficient method is the use of a rod dipped into bioink. Using this method, Tabriz et al. successfully fabricated layers with viable human embryonic kidney and mouse fibroblast cells. The layer thickness, measured between 126 and 220 μm, was determined by the surface wettability and the hydrogel composition applied prior to cross-linking (Ghanizadeh Tabriz et al., 2017). In rod-supporting printing or electrospinning, the biomaterials or fibres are extruded orderly onto a rotating rod (Akentjew et al., 2019). Wilkens et al. further advanced this approach by adding motors to rotate the dip rods, significantly enhancing control over the thickness of the layers (Wilkens et al., 2016). This technique has potential applications in creating a variety of tubular tissues. The rotational speed is the key factor in facilitating a uniform film on the rod. However, achieving a monolayer of small vascular structures remains a challenge. To further scaffold the implant vascular tissue, there is a need for combination methods to fabricate customisable vascular structures with variable thickness during bioprinting. Therefore, the application of the simple element of the rod allows for the fabrication of a universal method of structuring small blood vessels.

2.4 Research gap

The development of vascular structures in tissue engineering has made significant progress over the years, yielding promising results for various applications. However, the fabrication of small-diameter blood vessels, particularly those with diameters less than 6 mm, remains a substantial challenge. This complexity arises from the need to balance three critical factors: the function of the ECM, the structural integrity required for small-sized vessels, and the material properties, particularly elasticity, necessary to mimic natural blood vessels. To achieve these requirements, past studies have focused on synthetic materials or combinations thereof, thereby neglecting natural materials such as gelatin. Furthermore, there is a lack of research on cross-linking modes for unmodified gelatin, and many studies have treated gelatin as a secondary material. Depending on the material selected, researchers determine the appropriate technique to construct small blood vessel structures. However, the properties of the materials limit the range of fabrication techniques available for small vessels. The diameter of human vascular structures ranges from 10 mm to capillaries, with the smallest vessels measuring as little as 1 mm, and smaller capillaries relying more on endothelial cells for their movement. This range of 50 μm to 1 mm has been addressed by limit studies. To address this literature gap, this PhD research addresses these challenges by focusing on three key areas, as outlined in Figure 13, which serves as a visual roadmap of the thesis structure:

1. **Structural requirements & rapid fabrication (Chapter 4):** This research aims to select and optimise a rapid and precise 3D printing method to construct vascular structures replicating the small vascular blood vessels.
2. **Performance requirements and material improvement (Chapter 5):** The printed vessels can support cellular growth and integration with host tissue by utilising gelatin, a natural biomaterial that closely mimics the extracellular matrix (ECM). To enhance the mechanical properties of the gelatin-based structures without compromising their flexibility, a small amount of polymer is incorporated into the gelatin matrix. This approach aims to balance strength and elasticity, ensuring the printed vessels can withstand physiological conditions while maintaining their functionality.
3. **Fabrication of small and microvascular structure (Chapter 6):** Gelatin/PEGDA hydrogels were used to fabricate small tubular structures with a diameter from 0.7 to 2 mm through rotational dipping printing. A smart hydrogel is used as a sacrificial template to print a microvascular with a diameter of 70 μm to achieve the macro to micro vessel tissue.

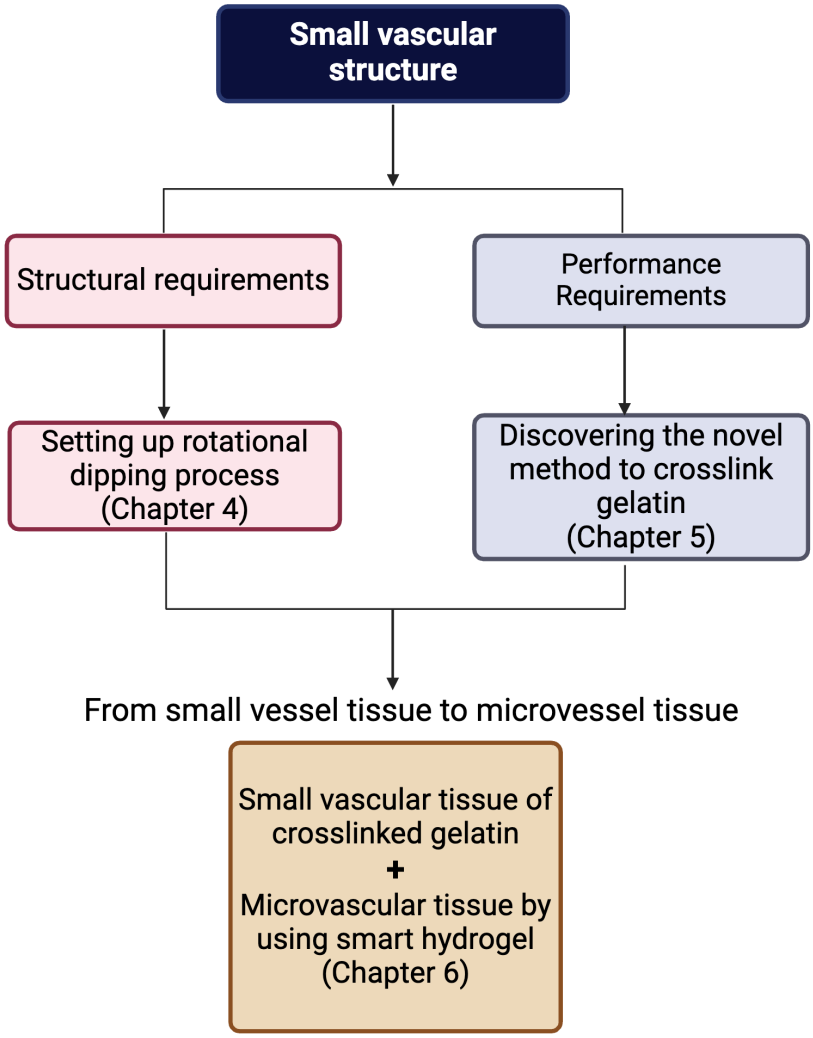

Figure 13 The structure of the thesis

3. Methodology

In this chapter, the general material preparation and tests were described.

3.1 Material

3.1.1 Gelatin solution

Different concentrations of gelatin solution were prepared in deionised water using gelatin from porcine skin (G1890, Sigma, UK). After dissolving the gelatin powder under magnetic stirring of 300rpm at 40 °C, then the solutions were kept at 37 °C. The gelatin solution is used as fresh, avoiding biodegradation.

3.1.2 Synthesis of GelMA

10.0 g of type A porcine skin gelatin (Sigma-Aldrich, St. Louis, MO) was added to 100 mL of Dulbecco's phosphate-buffered saline (DPBS) (Invitrogen, San Diego, CA) and dissolved by stirring at 60 °C using a magnetic stirrer. After dissolving the gelatin solution, keep it at 55 °C. 1.25mL of methacrylic anhydride was then added to react with the gelatin solution under vigorous stirring for 3 h at 1000rpm/min at 55 °C. [Adding methacrylic anhydride drop by drop and slowly (100uL/min)]. Then, the reaction was stopped by 100mL warm (40 °C) DPBS. All solution was kept with 12–14 kDa dialysis tube and stored in dH_2O at 37 °C. Salts and unreacted methacrylic anhydride were removed from the mixture by one week of dialysis with a 12–14 kDa cut-off in distilled water at 40 °C. After one week, solution was dispensed in centrifuge tubes (about 15 mL each tube). Place in the -80°C freezer for freezing. White porous foam was then obtained by lyophilising the solution for 48 hours and was stored at −20 °C until further use.

Methacryloyl substitution groups were grafted onto the reactive amine and hydroxyl groups (Fig 14, a). This reaction is characterised by ^{1}H-NMR. 10 mg GelMA powder was dissolved in 650 µL deuterium oxide and characterised using Bruker AVIII-HD-500 NMR Spectrometer. In the ^{1}H-NMR spectrum, the phenylalanine signal (6.50–8.00 ppm) represents the concentration of gelatin. If the phenylalanine signal is normalised, the degree of methacrylation is calculated as follows:

$$DM(\%) = \left(1 - \frac{A[\text{lysine methylene in GelMA}]}{A[lysine\ methylene\ in\ gelatin]}\right) \times 100$$

In this equation, A[lysine methylene in GelMA] is the area of lysine methylene signals (3.10–3.25 ppm) in GelMA, and A[lysine methylene in gelatin] is the area of lysine methylene signals (3.10–3.25 ppm) in gelatin.

Compared with gelatin, there are three new peaks for GelMA at δ = 2.10 ppm, δ = 5.62 ppm and δ = 5.87 ppm, which is assigned to introduced methacrylate (usually the vinyl protons in the range of 5.5–6.5 ppm) (Fig 14, b). This result indicates that methacrylate has been successfully grafted to the gelatin molecules, and the degree of methacrylation was calculated to be 57.4%.

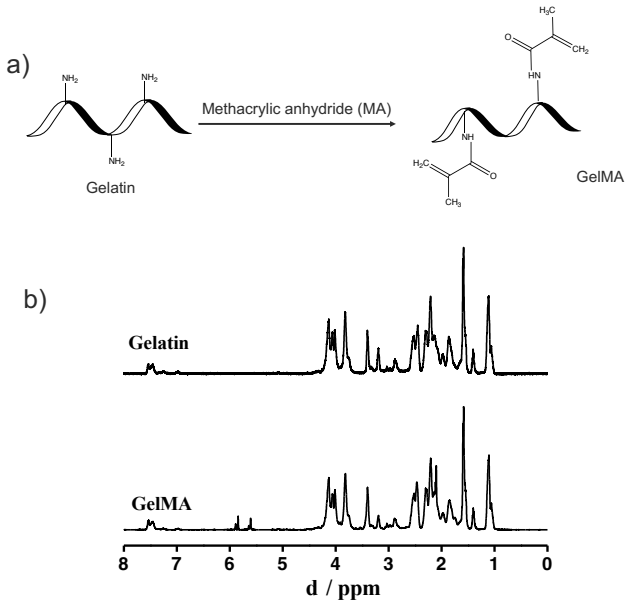

Figure 14 Synthesis a) and Characterisation b) of GelMA compared with gelatin

Different concentrations of GelMA powder was first dissolved deionised water containing desirable photoinitiator Irgacure 2959 (Sigma). The solution was sonicated at 37 °C until fully dissolved. Then the solution was kept at 37 °C overnight to remove air bubbles prior to use.

3.1.3 Alginate solution

Alginate solutions were prepared in deionised water without $CaCl_2$ or $MgCl_2$, using sodium alginate (W201502, Sigma, UK). After dissolving alginate under magnetic stirring at 60 °C, solutions were kept at room temperature. To crosslink alginate hydrogels, 100mM $CaCl_2$ crosslinking solution (C5670, Sigma, UK) was prepared in deionised water.

3.2 Material properties tests

3.2.1 Mechanical tests

Mechanical testing was a significant part of the thesis, and aimed at evaluating the mechanical properties of the developed biomaterials to ensure their suitability for small vascular tissue engineering. To evaluate the mechanical properties of the material, tensile tests were conducted following ISO-527-1-2012. These tests were performed to determine the material's tensile strength, elongation at break, Young's modulus, and maximum force, which are critical for assessing the material's mechanical performance in clinical use:

- Tensile strength: maximum stress at rupture
- Young's modulus: slope of the linear elastic region
- Elongation at break: strain at the point of failure
- Maximum force: peak force applied prior to fracture

The material was cast into a Dumbbell shape (Fig 15, a), whose size is based on ISO-527-2-2012. The parameter is shown in Fig 15b. Based on this parameter, a 3D model was set up in the stl. file (Fig 15, c) and printed with Polylactic Acid (PLA, the black piece in Fig 15 d). Ten black PLA samples were prepared and used in casting the green silicon mold (BBDINO Super Elastic Silicone Mould Making Kit) (Fig 15, d). The hydrogel material was cast into the silicon mold and mounted onto a Biomomentum Mach-1 (*Biomomentum Inc., Canada*) equipped with a load cell of 100N and two tensile grippers (Fig. 15, f). The test was conducted at room temperature, with a velocity of 0.1mm/s, ensuring the strain rate was consistent across all samples.

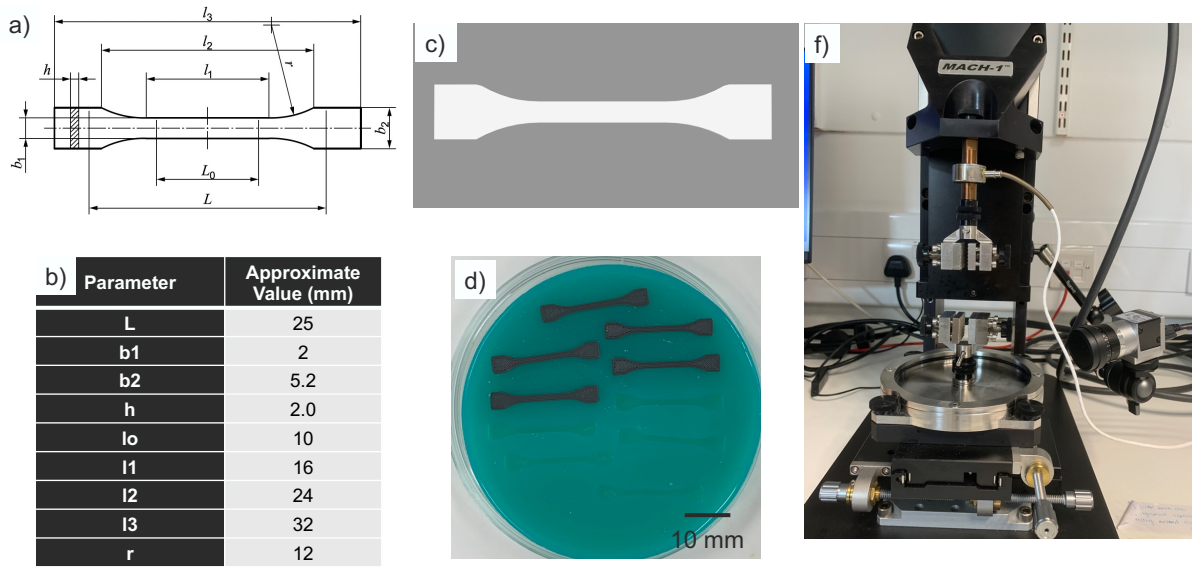

b)

Parameter	Approximate Value (mm)
L	25
b1	2
b2	5.2
h	2.0
lo	10
l1	16
l2	24
l3	32
r	12

Figure 15 The sample preparation for tensile test

The tensile test was initiated by applying an increasing uniaxial load to the samples until failure. The force and corresponding displacement were recorded continuously throughout the test. This data was used to generate the material's stress-strain curve. The Young's modulus (E), a measure of material stiffness, was determined from the initial 20% linear region of the stress-strain curve. The elastic modulus was calculated using the formula:

$$E = \frac{\Delta\sigma}{\Delta\epsilon}$$

Where:

E is the Young's modulus (in MPa),

$\Delta\sigma$ is the change in stress (in N/m²),

$\Delta\epsilon$ is the change in strain (dimensionless).

The tensile strength σ_{tensile} of the material was calculated as the maximum stress the material could withstand before breaking. The maximum force was recorded as the highest force applied to the material before fracturing, representing its ultimate load-bearing capacity. It was determined from the highest point on the stress-strain curve, using the formula:

$$\sigma_{\text{tensile}} = \frac{F_{max}}{A}$$

Where:

σ_{tensile} is the tensile strength (in MPa),

F_{max} is the maximum force applied (in N),

A is the cross-sectional area of the sample (in mm²).

Elongation at break ϵ_{break} measures the extent to which the material stretched before failure. It was calculated as the ratio of the total elongation to the original length of the sample at the point of fracture:

$$\epsilon_{\text{break}} = \frac{\Delta L_{\text{break}}}{L_0}$$

Where:

ϵ_{break} is the elongation at break (dimensionless),

ΔL_{break} is the increased length at the point of break (in mm),

L_0 is the original gauge length of the sample (in mm).

3.2.2 Degradation percentage

To evaluate material's biodegradation behaviour, a controlled experiment was conducted. The samples were immersed in diluted water and continuously incubated in a CO_2 incubator over 4 weeks, with removal at weekly intervals. All the samples were cut into 10mmX10mmX2mm. After freeze-dried, each sample was measured to obtain the initial dry weight W_0. The dried samples were then immersed in water, placed in sealed containers, and incubated at 37°C. The samples were removed from the incubator at weekly intervals (week 1, 2, 3, and 4). After removal, each sample was rinsed with distilled water to eliminate any remaining solvent and freeze-dried to obtain the post-degradation

dry for each time point W_t. The percentage of weight loss due to biodegradation was calculated using the following formula:

$$\text{Biodegradation percentage } = \frac{W_0 - W_t}{W_0} \times 100$$

Where:

W_0 is the initial dry weight,

W_t is the dry weight after degradation at the time (in weeks).

3.2.3 Water absorption percentage

The swelling behaviour was investigated by weighing the samples before (Wo) and after (Wt) immersion in PBS solution at 37 °C at various time points. The swelling ratio was calculated using the formula:

$$\text{Swelling ratio \%} = \frac{\text{Wt} - \text{Wo}}{\text{Wo}} \%$$

Where:

Wt represents the weight of different time points.

Wo represents the weight of origin.

3.2.4 Gelatin release

To quantify gelatin release into the buffer at various time points, the concentration of gelatin in the buffer was determined using the Bicinchoninic Acid (Micro BCA Protein Assay Kit, Thermo Scientific). The BCA assay is a colorimetric technique used to quantify the concentration of protein in a sample, relying on the biochemical reduction of Cu^{2+} to Cu^{+} under alkaline conditions. This reduction is a two-step process facilitated by peptide bonds in gelatin. When gelatin is present in an alkaline environment, it reduces Cu^{2+} ions to Cu^{+}, creating a proportional amount of reduced copper in the solution. Then, bicinchoninic acid, a chromogenic reagent, complexes with the Cu^{+} ions to produce a stable, water-soluble purple complex. This complex absorbs light at a wavelength of 562 nm, making it detectable via spectrophotometry. The intensity of the colour is directly proportional to the protein concentration, allowing for quantification by comparing the absorbance to a standard curve generated using known protein concentrations, such as bovine serum albumin (BSA).

A standard curve was established using gelatin solutions in Phosphate-Buffered Saline (PBS) at varying concentrations (200, 40, 20, 10, 5, 2.5, 1, 0.5 µg/mL), described by the quadratic equation Y = -2.587 + 32.39*X + 76.79*X^2, R^2 = 0.998. At each time point, the buffer samples collected from each experimental group were mixed with the working reagent provided in the BCA assay kit and

subsequently incubated for two hours. Following this incubation period, the samples were cooled down to room temperature. The absorbance of these samples was then measured at 562 nm using a spectrophotometric plate reader. The gelatin concentration in each sample was determined by referencing these absorbance values against the established standard curve. The Gelatin release were calculated by

$$\text{Gelatin release } \% = \frac{W_{(\text{gelatin detected})}}{W_{(\text{gelatin printed})}} \%$$

$W_{(\text{gelatin detected})}$ represents the weight of gelatin detected in BCA assay;

$W_{(\text{gelatin printed})}$ represents the weight of gelatin printed in the sample.

3.3 In Vitro Cytotoxicity Testing

To evaluate the cytocompatibility of the material, two in vitro cytotoxicity tests were performed: (1) the direct contact test for qualitative analysis using live/dead staining and (2) the extractable test for quantitative analysis using the MTT assay. All the materials in dry condition were sterilised by autoclaving and exposed under UV light for 20 mins and then immersed in sterilised PBS solution at 37°C to reach water equilibrium for biological tests. For non-contact cytotoxicity, the extra medium is prepared with the extraction ratio (surface area or mass/volume) of 3 cm^2/ml followed by ISO-10993-12:2012. For direct-contact cytotoxicity, the sample is cut into 1cm^2 and placed in a 24-well plate with 1mL medium. Three different cells were chosen for different applications in this research.

3.3.1 Cells staining

Propidium Iodide (PI) is a red-fluorescent nucleic acid stain that selectively binds to DNA by intercalating between base pairs. However, PI is impermeable to live cell membranes, making it useful for identifying dead cells. Fluorescein Diacetate (FDA) is a non-fluorescent compound that can diffuse across cell membranes. In live cells, intracellular esterases hydrolyse FDA, converting it into the highly fluorescent compound fluorescein. This process highlights viable cells. After incubation, live/dead staining was performed using propidium iodide (PI) and fluorescein diacetate (FDA) to assess cell viability qualitatively. The staining solution was prepared by diluting PI and FDA in phosphate-buffered saline (PBS) at final concentrations of 20 µg/mL for PI and 2.5 µM/mL for FDA. The cells on the material were incubated with the PI solution for 1 minutes at room temperature in the dark and then washed with PBS three times. And then, the cells were incubated with FDA solution for 5 mins at room temperature in the dark and then washed with PBS three time. Following washing with PBS, fluorescence microscopy was used to visualise the live and dead cells using a ZOE fluorescence microscope.

DAPI (4′,6-diamidino-2-phenylindole) is a fluorescent stain that binds strongly to adenine-thymine (A-T)-rich regions of DNA. DAPI staining was used to visualise nuclei in fixed HUVEC cells. Firstly, cells were washed with PBS to remove any residual medium. Then, 4 wt% paraformaldehyde (PFA) in PBS was added to fix cells for 10–15 minutes at room temperature. The fixed cells were washed three times with PBS to remove excess fixative and stored at 4°C for further staining. The working concentration of DAPI is 300 mM. The fixed cells were incubated with DAPI solution for 10 mins in room temperature avoiding light and then removed the DAPI solution and washed with PBS. Following washing with PBS, fluorescence microscopy was used to visualise the live cells using a ZOE fluorescence microscope.

3.3.2 MTT assay

200 µL of cells were seeded in a 96-well flat-bottom microtiter plate at a density of 1×10^4 cells/well and allowed to adhere for 24 hours at 37°C in a CO^2 incubator. After 24 hours of incubation, 200 µL culture medium was replaced with an extract medium. Cells were then treated with extract medium for 24 hours at 37°C in a CO^2 incubator. After 24 hours of incubation, the culture medium was replaced with a fresh medium of 100 µL. Subsequently, 100 µL of MTT working solution (10mM MTT prepared in PBS (pH 7.4) then sterile filtered. This solution can be stored at 4°C for up to 2 weeks.) was added to each well, and the plate was incubated for 4 hours at 37°C in a CO^2 incubator. The 100 µL medium was then aspirated, and the formazan crystals formed were solubilized by adding 100 µL of DMSO per well for 30 min at 37°C in a CO^2 incubator. Finally, the intensity of the dissolved formazan crystals (purple colour) was quantified using the Skanlt GO plate reader at 540 nm.

3.3.3 Fibroblast cells

The red fluorescent human dermal fibroblasts (Red TTFLUOR HDF) were chosen as a pre-test for their rapid growth and self-fluorescence for easy viewing (Fig 16 a). All red-channel fluorescence in the HDF study derives from constitutive expression of RFP within the cytosol of the fibroblasts (Fig 16 b). No additional nuclear or cytoskeletal stains were applied. HDFs were cultured in Dulbecco's Modified Eagle Medium (DMEM) supplemented with 10% fetal bovine serum (FBS) and 1% penicillin-streptomycin. Cells were maintained at 37°C in a humidified incubator with 5% CO_2. Passage 3-5 cells were used for all experiments. Before seeding onto scaffolds, fibroblasts were trypsinised using 0.25% trypsin-EDTA, counted with a hemocytometer, and resuspended at the desired concentration.

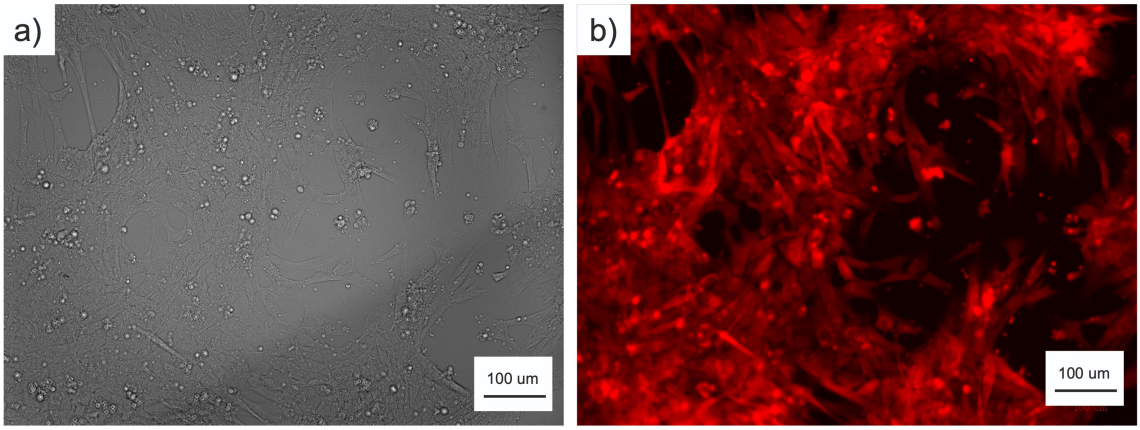

Figure 16 The red fluorescent human dermal fibroblasts under the brightfield a) and the red channel b) without any staining

3.3.4 Human umbilical vein endothelial cells

Human umbilical vein endothelial cells (HUVECs), as the main cells in the vasculature, were obtained from human umbilical cords by collagenase digestion (Fig 17 a & d). They were cultured in endothelial cell growth medium (EGM-2), supplemented with 2% FBS, vascular endothelial growth factor (VEGF), basic fibroblast growth factor (bFGF), and hydrocortisone. Cells were incubated at 37°C in a humidified atmosphere of 5% CO_2, with medium changes every two days. Cells between passages 3 and 6 were used for experiments. Before the experiments, HUVECS were detached using 0.05% trypsin-EDTA and then seeded onto prepared scaffolds for further analysis. After live/dead staining, the nuclear of the live HUVECs is green (Fig 16 b), dead is red (Fig 16 c). After DAPI staining, the nuclear of the live HUVECs is blue (Fig 16 e). Some dead cells could be caused by handling stress (trypsinisation, centrifugation, and medium changes).

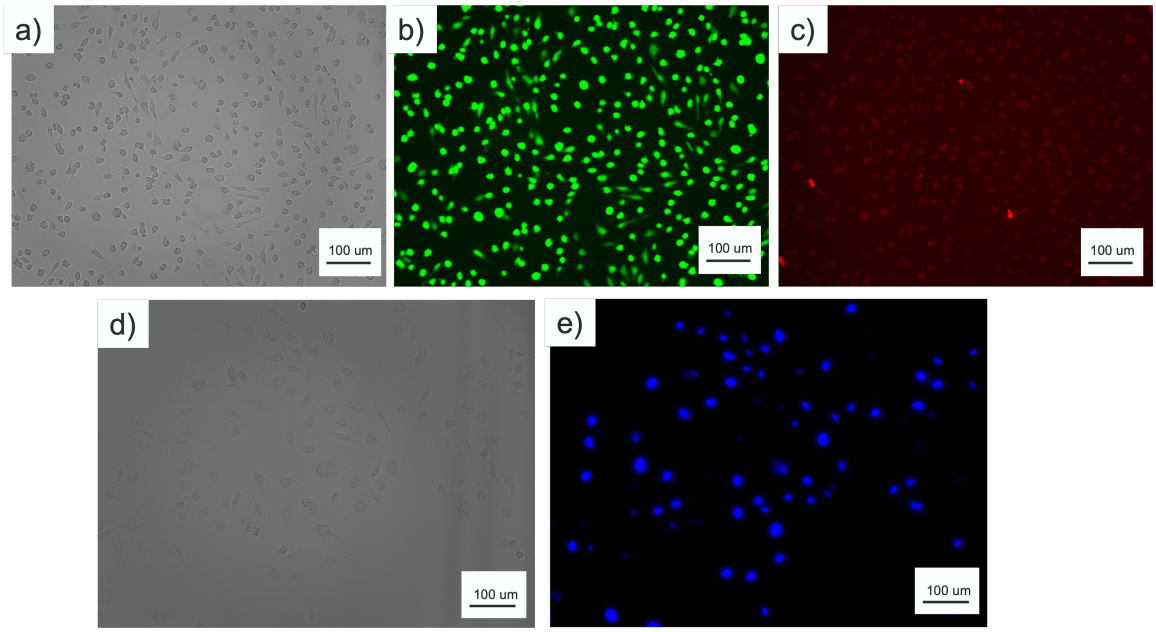

Figure 17 The HUVECs under the brightfield a and d) with the live cells in green b) and the dead cells in red c) after live/dead staining and the nuclear of the cells in blue e) after DAPI staining

3.3.5 Human osteosarcoma cells

Human osteosarcoma cells (MG-63 line) were chosen as expanded research (Fig 18 a)and cultured in DMEM supplemented with 10% FBS and 1% penicillin-streptomycin. Cells were incubated at 37°C with 5% CO_2 and 95% relative humidity. Cells between passages 4 and 8 were used for experimentation. Prior to seeding on scaffolds or plates, the osteosarcoma cells were detached with 0.25% trypsin-EDTA, centrifuged, resuspended, and counted. Seeding density was adjusted depending on the requirements of individual experiments. After live/dead staining, the nuclear of the live HUVECs is green (Fig 18 b), dead is red (Fig 18 c). Some dead cells (Fig18 c) could be caused by handling stress (trypsinization, centrifugation, and medium changes) and over-confluency.

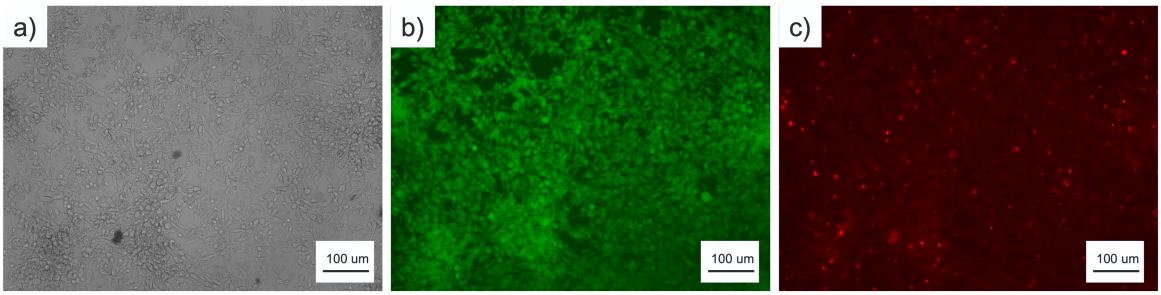

Figure 18 Human osteosarcoma cells under the brightfield a) with the live cells in green b) and the dead cells in red c) after live/dead staining

3.4 Image

The optical microscope (Brunel Microscopes Ltd) and scanning electron microscope (HITACHI, TM-1000) recorded the material's microstructure. Bio-Rad ZOE fluorescent cell imager (Bio-Rad Laboratories, Inc., United Kingdom) with three channels used to observe cell morphology. All images are analysed in ImageJ software. To generate the final composite images, each source image (originally acquired at 12- or 16-bit depth) is first converted to 8-bit based on the current Brightness & Contrast settings and then combined into a single 24-bit RGB image. This conversion unavoidably compresses the dynamic range and remaps pixel intensities, leading to an apparent reduction in fluorescence signal in the merged overlay.

3.5 Statistical analysis

All experiments were conducted in five replicates, except for the live/dead staining, which was performed in triplicate. The results are expressed as mean ± standard deviation (SD). Data were analysed using Prism 10 software (GraphPad Software, Inc.), and all datasets were confirmed to follow a normal distribution using the Shapiro-Wilk test. For comparisons between two groups, a two-tailed unpaired t-test was performed. For comparisons among more than two groups, a one-way analysis of variance (ANOVA) was conducted, followed by Tukey's post hoc test for multiple comparisons. A p-value of < 0.05 was considered statistically significant. Statistical significance was indicated as follows: $p < 0.05$ (*), $p < 0.001$ (**), $p < 0.0001$ (***), $p < 0.00001$ (****). All tests were performed with a 95% confidence interval.

4. Rotational dipping printing to fabricate the vascular structure

This chapter examines the potential of rotational dipping printing to create vascular structures. Specifically, adjustments in parameters such as rotational speed, material consistency, and the dipping process significantly affect the structure of the resulting tubes. The objective is to illustrate how this technique might establish a new standard for producing small vascular grafts that meet the demands of the field.

4.1 The design of the rotational printing

The proposed design aims to integrate rotational printing with a dipping process to fabricate vascular structures using biomaterials, referred to as "Rotational Dipping Printing" (RDP). The central element of this methodology is a stainless-steel mandrel, which serves as the substrate for the deposition of biomaterials. As shown in Fig 19, the mandrel's rotation is precisely controlled by a motor, allowing for uniform application and thickness of the biomaterial layers. The process begins with the mandrel being rotated at a predetermined speed (Fig 19, a). Concurrently, it is dipped into a polymer solution, ensuring the biomaterial coats the mandrel's surface uniformly (Fig 19, b). As the mandrel is withdrawn from the solution, the rotation facilitates even distribution and smoothing of the polymer (Fig 19, c), minimising anomalies such as drips or uneven coating commonly observed in static dipping processes. Once the mandrel is extracted from the solution coated with a thin layer of polymer, the polymer undergoes crosslinking (Fig 19, d). This is a critical phase where the polymer transforms from a liquid state to a gel yet flexible vascular structure, conforming to the shape of the mandrel (Fig 19, e). The crosslinking mechanism can be initiated or accelerated by various means, including chemical agents, temperature changes, or UV radiation, depending on the nature of the polymer used. In this chapter, alginate prepared as in section 3.1.3 was used.

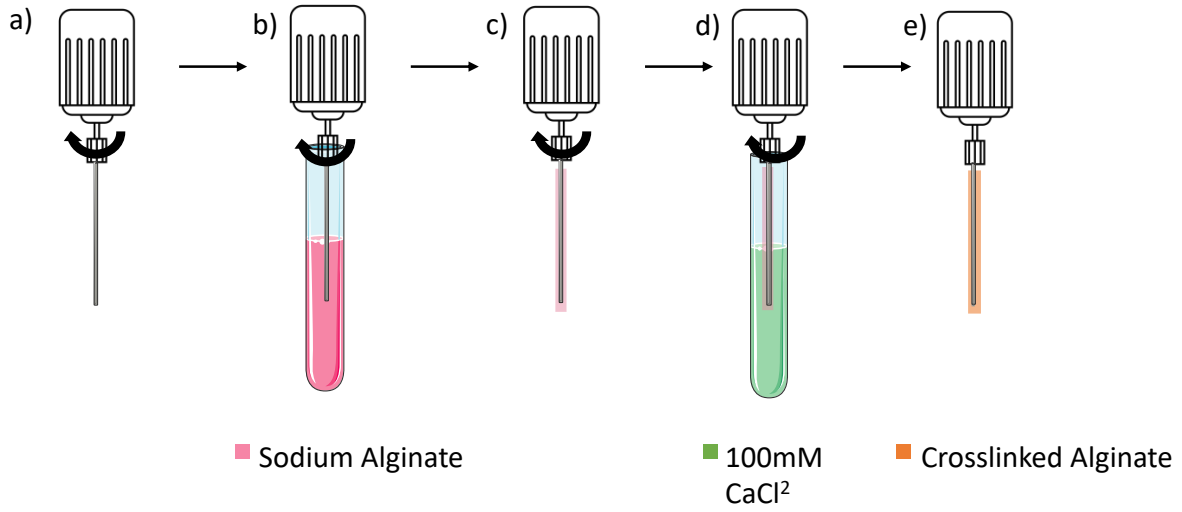

Figure 19 The process of Rotational Dipping Printing: a) rotation motor; b) dipping into alginate; c) removing from the alginate; d) dipping into $CaCl_2$; e) a crosslinked alginate tube.

The design of the RDP system aims to gain the benefits of rotational printing - primarily the ability to produce uniform, concentric layers of material - and combine it with the simplicity and versatility of the dipping process. This hybrid technique is particularly suited for fabricating vascular structures with precise dimensional control, uniformity in wall thickness, and customised surface properties, making it an ideal choice for applications in biomedical engineering, such as the creation of vascular grafts or stents. Furthermore, the choice of biomaterials and the optimisation of process parameters like rotational speed, dipping duration, and crosslinking conditions are pivotal in determining the mechanical and biological properties of the fabricated vascular structures. Such parameters can be adjusted to meet the specific requirements of the intended application, ensuring biocompatibility, structural integrity, and functionality of the vascular structure.

4.2 Material and method

Three different concentrations of sodium Alginate solutions were prepared in deionised water without $CaCl_2$ or $MgCl_2$ using sodium alginate (W201502, Sigma, UK). After dissolving alginate under magnetic stirring at 60 °C, the solutions were kept at room temperature. To crosslink alginate hydrogels, a 100mM $CaCl_2$ crosslinking solution (C5670, Sigma, UK) was prepared in deionised water.

The printing process is described in Figure 19. The fabrication of the alginate tube is shown in Fig 20. Driven by a motor (B01LXCSBPQ, SWHstore, UK), the speed of the mandrel was linear relation with the voltage of the motor. A stainless-steel rod (22G) was used as a mandrel, rotationally dipped into the alginate solution and kept for 5 min. The mandrel coated with alginate was withdrawn slowly and soaked in the $CaCl_2$ crosslinking solution for 15 min. After rinsing with deionised water, the tube was removed for air drying for 5 min.

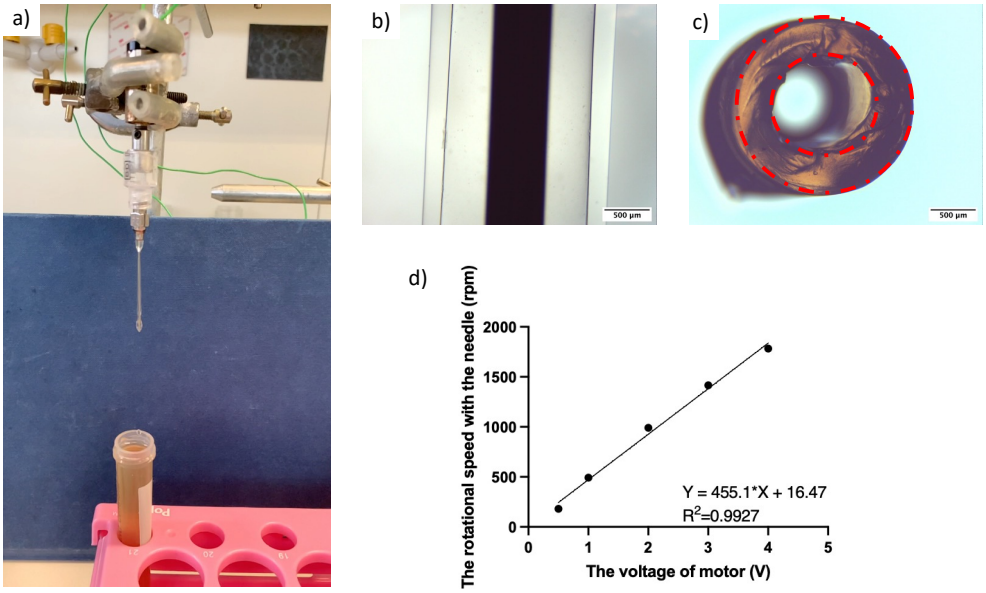

Figure 20 The fabrication of the alginate tube with a motor a): the diameter b) and the even wall c) was measured under the microscope with the determined speed d)

In Wilkens's research, they investigated the effects of different viscosities and pull-out speeds on the uniformity and thickness of tubular structures (Wilkens et al., 2016). However, their research did not explore the impact of rotational speed on the structure of the biomaterial. In this research, several factors, including viscosity, needle size, and rotational speed, were examined for their effect on the tubular structure (Table 3). Under different conditions, the alginate tubes were observed under an optical microscope. The wall thicknesses of the small tubular structures were recorded and analysed for their relationship with the factors. Since the crosslinking of alginate is not the focus of this research, the concentration of the $CaCl_2$ is fixed.

Table 3 Factors Affecting Diameter and Wall Thickness

Factors Affecting Diameter and Wall Thickness:	Description	Conducting Rotational Dipping Experiments
Needle Size	The diameter of the needle serves as the mold around which the tubular structure is formed. A larger needle will naturally result in a larger tube diameter.	Different size of needle: 14Ga, 16Ga, 18Ga, 20Ga, and 22 Ga. The range from 0.72 mm to 2.11 mm in diameter, which matched arterioles and venules.
Rotational Speed	The speed at which the needle rotates influences the shear rate and centrifugal forces. Higher speeds can lead to thinner films due to increased centrifugal force.	Different voltage of motor: 0.5V, 1V, 2V, 3V and 4V
Viscosity	The fluid's resistance to flow will affect how it coats the needle. More viscous fluids will form thicker layers and thus potentially thicker walls, given the same rotational speed and needle size.	Different concentration of alginate solution: 1%, 2%, 3%, 4%, and 5% (w/v) alginate. In 1% group, there is no material remained on needle, no result display.
Concentration of Cross-Linking Agent	In the case of materials that undergo cross-linking (like alginate with CaCl2), the concentration of the cross-linking agent can affect the rate at which the liquid solidifies, thus affecting the thickness.	Fixed concentration of $CaCl_2$:100mM
Ambient Conditions	Temperature and humidity can affect the viscosity of the liquid and the drying or curing rate, which in turn influences the tube's wall thickness and strength.	Same lab room temperature of 25 ℃
Density (ρ) of the Liquid	The density will affect the centrifugal forces acting on the liquid. A denser liquid will exert more outward force, potentially leading to a thinner film on the needle.	Different concentrations of alginate solution: 1%, 2%, 3%, 4%, and 5% (w/v) alginate. In the 1% group, there is no material remaining on the needle, and no result is displayed.
Duration of Exposure to Cross-Linking Agent	For materials that require cross-linking, the duration for which the material is exposed to the cross-linking agent will determine the degree of solidification, potentially influencing wall thickness.	Fixed time immersing to $CaCl_2$ solution: 5 mins

4.3 Results

4.3.1 The uniformity of alginate tubes

The study compares alginate tubes fabricated using traditional dipping and rotational dipping methods at 493 rpm, highlighting the superiority of the rotational method in achieving uniformity. Visual comparisons (Fig 21, a) show that traditional dipping results in irregularities and deformations due to gravity-induced sagging. In contrast, rotational dipping produces consistent tube diameters, as supported by the accompanying graphical data. The traditional graph shows significant diameter variability (Fig 21, b), whereas the rotational method displays tightly grouped data points (Fig 21, c), indicating uniform material distribution aided by the centrifugal force. This consistency is critical for applications requiring precise dimensional control, such as tissue engineering scaffolds and microfluidic devices, where wall thickness can compromise mechanical performance. The results further suggest that adjusting rotational speed can fine-tune tube dimensions, offering a scalable and reproducible fabrication approach for biomedical use.

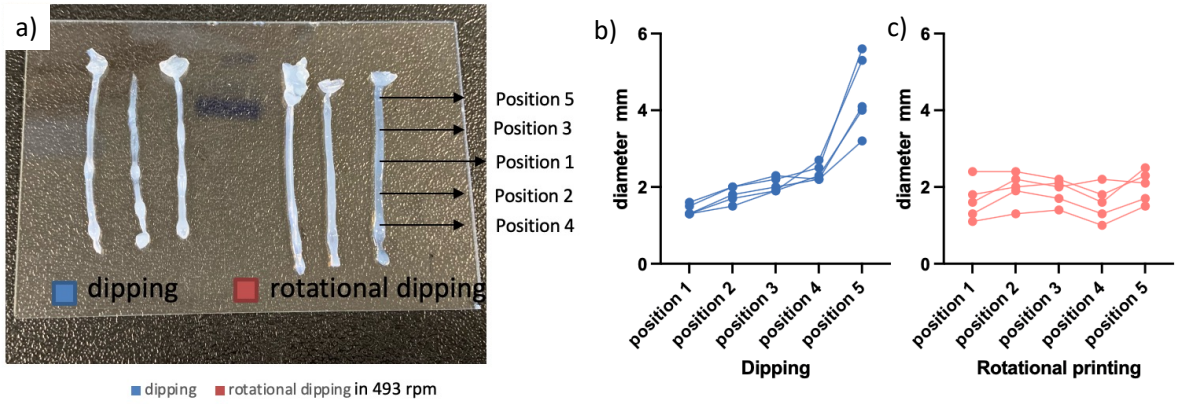

Figure 21 The consistency of alginate tubes a) of different dipping methods of dipping b) and rotational printing c).

4.3.2 The effect parameters of the vascular structure

Three important factors that affect the small tubular structure were analysed. When the different voltages were tested, the concentration of the alginate was fixed at 5% (w/v) and the needle size was fixed at 18 Ga. When the different needle sizes were tested, the concentration of the alginate was fixed at 5% (w/v) and the voltage was fixed at 1V. When the different concentrations of the alginate were tested, the needle size was fixed at 18 Ga and the voltage was fixed at 1V.

In Fig 22, the figure presents a study on the relationship between the voltage applied to the motor in a rotational dipping fabrication method and the resulting wall thickness of the produced alginate tubes. The plotted data points show a negative linear relationship (Fig 22, a), as indicated by the trend line with the equation Y = -78.69X + 354.6, where 'Y' represents the wall thickness and 'X' represents the voltage. The coefficient of determination, R^2 = 0.8365, suggests a strong inverse correlation between the voltage applied to the motor and the wall thickness of the tubes. The quantitative analysis depicted in the graph establishes a clear inverse relationship between the voltage of the motor—which directly correlates to the rotational speed—and the wall thickness of the fabricated tubes.

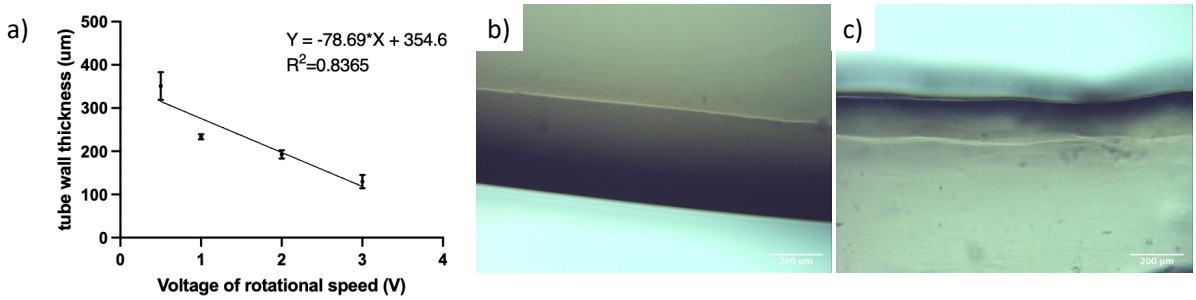

Figure 22 The effect of the voltage of the rotational speed with a negative linear relationship a). One sample was with at a low voltage of 0.5V (b) and another was at a higher voltage of 3V (c).

Two samples of the alginate tubes were shown. One was with at a low voltage of 0.5V (Fig 22, b) and another was at a higher voltage of 3V (Fig 22, c). Under low voltage, the tube exhibits a relatively

thick and consistent wall, suggesting less influence of centrifugal forces at lower rotational speeds. Another one demonstrates a thinner and less uniform wall thickness, with visible undulations and irregularities, implying that higher rotational speeds induced by greater voltage result in the spread of the material and a reduction in wall thickness.

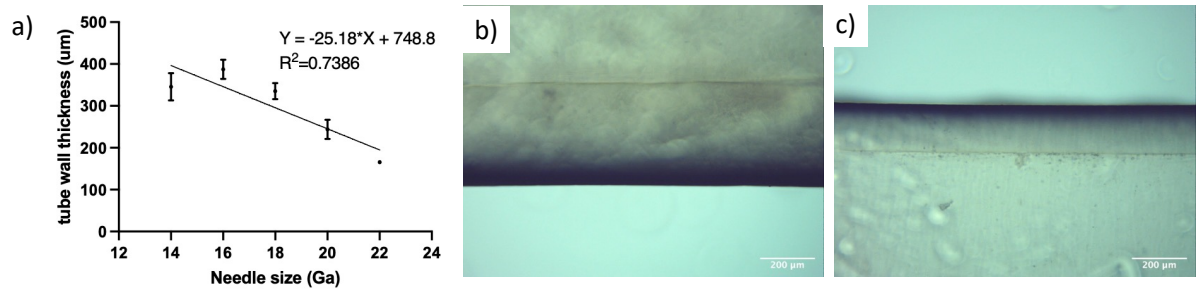

Figure 23 The effect of the needle size with a negative linear relationship a). One sample was with a low needle size of 14Ga (b) and another was at a higher needle size of 22Ga (c).

The influence of needle size on the wall thickness of alginate tubes created via a rotational dipping method was displayed in Fig 23. A negative linear relationship is observed (Fig 23, a), indicated by the descending trend line and described by the equation Y = -25.18X + 748.8, where 'Y' is the wall thickness and 'X' is the needle size. The coefficient of determination, R^2 of 0.7386, suggests a moderate to strong inverse correlation, implying that smaller needle sizes (which correspond to larger diameters) result in thicker tube walls. With a larger needle size, corresponding to a thinner gauge, the tube has a thinner wall, which aligns with the trend indicated in the graph (Fig 23, b). Using a smaller needle size, corresponding to a thicker gauge. This sample has a visibly thicker wall, which supports the graph's indication that larger needle diameters contribute to increased wall thickness.

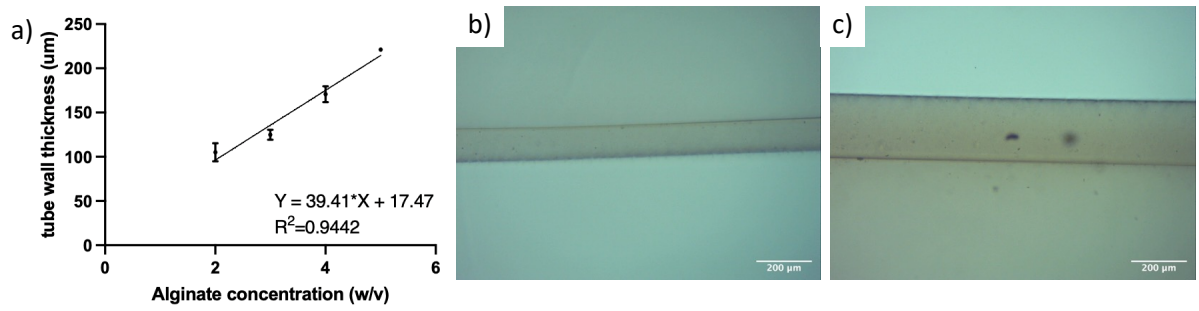

Figure 24 The effect of the alginate concentration with a linear relationship a).). One sample was with a lower concentration b) and and another was at a higher concentration c).

An analysis of the relationship between alginate concentration and the structural characteristics of tubes was shown in Fig 24. The graph delineates a clear linear relationship, suggesting that as the alginate concentration increases (Fig 24, a), there is a proportional increase in the thickness of the tube walls by the equation Y = 39.41X + 17.47, where 'Y' is the wall thickness and 'X' is the alginate concentration. The lower concentration sample exhibits a slender and more consistent wall profile (Fig 24, b), indicative of a smoother gelation process and less material deposition per layer. In contrast, the

higher concentration sample shows increased wall thickness and potential aggregation of alginate (Fig 24, c), which may contribute to the observed irregularities.

4.4 Discussion

Successful tissue-engineered SDBV require precise control over biological and mechanical properties, including the concentric positioning of different layers to mimic natural blood vessels. Rotational rod dipping, combined rod supporting, and rotational printing. The article by Wilkens et al. (2017) explores an automated layer-by-layer rotational printing approach for constructing SDBVs. This methodology enables the formation of multilayer cylindrical structures with controlled thickness, lumen diameter, and precise cell distribution. The study thoroughly examines factors such as material viscosity and upward speed, focusing on their impact on construct uniformity and structural properties. However, while these parameters are extensively assessed, the effect of rotational speed on layer alignment—a critical factor for circumferential material organisation—remains unexplored. Addressing this gap, the present study demonstrates that controlling rotational speed significantly enhances alignment, an essential aspect of replicating the natural structure of vascular layers.

Without rotational speed, in dipping casting, as the stick is withdrawn, the adhering liquid may form either a column or a film due to surface tension (Maillard et al., 2016; Zhang et al., 2022). When a liquid column forms along the stick, **gravitational force** ($Fg = \rho gV$) acts downward on it, while viscous and adhesive forces exert an upward force, counteracting gravity. Additionally, **surface tension** around the liquid column's perimeter supports it, further countering gravitational pull. In the classical Landau–Levich–Derjaguin (LLD) regime, lubrication theory predicts a steady-state film thickness. A stable film is maintained only when the combined upward viscous, capillary, and adhesive forces exceed the film's weight; otherwise, the liquid drains off as discrete droplets. Maintaining this delicate equilibrium under gravity alone is challenging, since slight variations in withdrawal speed or surface wettability can precipitate film rupture. Introducing substrate rotation at angular speed and induces shear-driven leveling of the entrained layer. These rotation-driven effects redistribute the liquid circumferentially, counteract gravitational instability, and thus afford enhanced control over film uniformity and adhesion (Quéré, 1999). These dynamics reach equilibrium when the forces balance: if gravity and the liquid's weight surpass the combined viscous adhesive, and surface tension forces, the liquid will slide off. Conversely, if these upward forces are dominant, the liquid will remain adhered to the stick for a longer duration. It is challenge to keep balance of force stable; however, is introduced, and a rotational force can counteract gravity's effects, offering greater control over liquid adhesion.

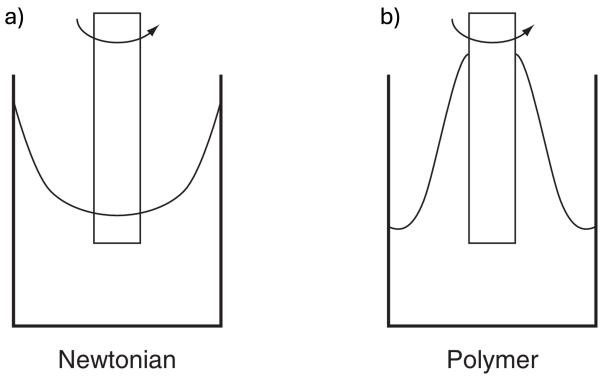

Figure 25 The physical phenomenon when dipping casting rotational speed in Newtonian fluid (a) and in polymer solution (b) (Vlachopoulos and Polychronopoulos, 2011).

The physical phenomenon changes if it comes to a dip with a rotational speed ω. As the stick rotates in the liquid, it will generate a shear flow in the liquid due to its motion (Quéré, 1999). This will create a velocity gradient in the liquid from the surface of the stick outward. The liquid closest to the stick will move with the stick, while the liquid farther from the stick will move more slowly. Because of the viscous nature of the fluid, a **resistive torque** will act against the rotation of the stick. This torque is proportional to the viscosity μ of the liquid and the shear rate. For a Newtonian fluid with constant viscosity, the resistive torque will increase linearly with the rotational speed ω (Emslie et al., 1958). Therefore, the liquids will be ejected outward from the rotational rod (Fig 25 a). In many biomaterials the fluid is non-Newtonian, e.g., shear-thinning, so μ effectively decreases with shear rate, altering both the torque and the velocity profile. One must then consider the apparent viscosity and possibly fit a power-law model (Bird et al., 1987, Barrulas and Corvo, 2023). The rotation will introduce centrifugal forces that will push the liquid outward, radially from the stick. This phenomenon is known as the Weissenberg effect (Vlachopoulos and Polychronopoulos, 2011). This means the liquid will tend to move away from the wall and climb up the sides if the stick is sufficiently immersed (Fig 25 b). Due to both adhesion and centrifugal effects, a rotating stick will pull out with a film of liquid around it. Centrifugal pressure drives thinner films near the axis, but thicker buildup toward the rim. The resulting film thickness is governed by a balance between centrifugal stress, viscous resistance, and capillarity, and can be solved from the thin-film equation. The thickness of this film might vary based on the balance between adhesion, viscosity, centrifugal forces, and surface tension. At high rotational speeds, centrifugal forces might dominate at high rotational speeds, causing the film to break apart and droplets to be thrown off.

This study selected alginate as the primary material for rotational rod dipping due to its lack of temperature sensitivity, unlike gelatin. The results show this rotational dipping method's versatility and scalability, which present it as a promising tool for producing functional SDBVs, even moving to other hydrogels. Further research is recommended to optimise the mechanical properties and functionality of the constructs, which may include experimenting with various photoinitiators and biomaterials.

Additionally, the automated dipping system, equipped with programmable microprocessors and stepper motors, enables precise control over the fabrication process.

5. Dual freeze drying of gelatin with poly(ethylene glycol) diacrylate

This chapter discussed a novel method for crosslinking pure gelatin with PEGDA. Firstly, the novel crosslinking method was initially evaluated against the traditional crosslinking approach to assess its effectiveness. Results from this comparison indicated that the new method not only led to successful crosslinking but also resulted in an improvement in the mechanical strength of the gelatin/PEGDA hydrogel. This preliminary evaluation examined key variables potentially affecting the cross-linking process. This study aimed to clarify the fundamental mechanisms to determine the best conditions for maximising crosslinking efficiency and enhancing the biomaterial's properties.

5.1 Discovering a novel method to crosslinking pure gelatin with PEGDA

Gelatin, a biocompatible and biodegradable natural polymer, is obtained by the partial hydrolysis and denaturation of collagen. Its applications range from scaffolding in tissue engineering to serving as a drug delivery carrier. Specifically, incorporated gelatin scaffolds provide interim support for three-dimensional cell culture, facilitating cell attachment, differentiation, and proliferation. Yet the mechanical strength of gelatin limits its application. Recent studies have elucidated that composite scaffolds' mechanical and biological properties are markedly superior to those made from pure gelatin (Young et al., 2020; Zeinali et al., 2021). The gelatin composite scaffold was explored by R. Govindan, who focused on bone tissue engineering applications (Govindan et al., 2020). The research utilised gelatin and phosphate glass (PG) in various concentrations to fabricate composite scaffolds via freeze-drying techniques. The findings highlighted a significant enhancement in the mechanical integrity of the scaffolds with the incorporation of PG, where the compressive modulus ranged between 0.6 and 2.3 MPa. Besides, freeze-drying, or lyophilisation, is a pivotal process that finds application in the enhancement of gelatin. Research led by Hunger et al.demonstrated the influential role of freezing rates on the mechanical attributes of alumina composites chitosan–gelatin solution (Hunger et al., 2013). The study revealed that higher freezing rates in small and bimodal slurries resulted in a structure akin to a honeycomb, enhancing mechanical efficiency through an increase in Young's modulus up to 20.05 ± 2.45 MPa. Therefore, incorporating gelatin in a hybrid polymer with the help of freeze-drying technology not only expands the biological applications but also enhances the mechanical strength.

Another material that is hugely popular in composites with gelatin is poly(ethylene glycol) diacrylate (PEGDA). Polyethylene glycol (PEG)-based hydrogels, with tunable cross-linking densities, have therefore been increasingly used in tissue engineering and drug delivery applications over the last two decades. In particular, acrylate or methacrylate PEG derivatives can be easily UV-cured to obtain hydrogels with complex shapes and microstructural crosslinking density gradients. Different crosslinking modalities were applied in gelatin and then hybridised with PEGDA. The most widely used is gelatin methacrylate (GelMA) (GhavamiNejad et al., 2020). The GelMA/PEGDA hydrogel exhibited higher mechanical strength, longer degradation time, faster diffusion rate, and lower swelling

rate than pure GelMA hydrogel. In Y Wang's research, the GelMA/PEGDA hydrogel exhibited higher compressive stress compared to pure GelMA hydrogel (Wang et al., 2018). Specifically, the stress of 10(w/v) %GelMA with 5(w/v) %was 70.6 kPa, almost 6 times that of 10(w/v) %GelMA, which was 12.1 kPa. The study conducted by Mamaghani et al. had a similar conclusion. GelMA, PEGDA and graphene oxide (GO) were synthesised and utilised in varying concentrations to create an interpenetrating network (IPN) hydrogel, employing techniques such as the modified Hummers' method for GO synthesis and UV radiation for hydrogel formation (Mamaghani et al., 2018). A 5 wt% GelMA hydrogel's modulus increased noticeably when 10 wt% PEGDA was added to it, rising to 192.1±22.9 kPa. This significant improvement is due to the interpenetrating polymer network (IPN) hydrogels forming a dense polymerised network. There is other research investigating different crosslinking of gelatin with PEGDA. Yao Fu explores the synthesis and characterisation of crosslinked thiolated gelatin-based hydrogels and PEGDA, utilising photo-crosslinking for applications in cartilage tissue engineering and drug delivery matrices (Fu et al., 2012). In this study, a physically incorporated gelatin hydrogel was tested as the control group. The Swelling and degradation profiles show that gelatin chains in untreated gelatin, when dissolved in a solution, undergo relaxation, becoming soluble and causing them to slowly disperse out of the polyethene glycol (PEG) network.

To preserve the exceptional biocompatibility of pure gelatin, researchers have paid less attention to the physical cross-linking between pure gelatin and PEGDA. Upon reviewing various techniques to improve the mechanical strength of hybrid materials, it was discovered that lyophilisation serves as an effective linking method between pure gelatin and PEGDA. As previously mentioned, lyophilisation enhances the mechanical properties of gelatin-based hybrid materials. Furthermore, freezing, a critical step in the lyophilisation process, also impacts the properties of PEGDA. Additionally, using cryopolymerization, the mechanical characteristics of PEGDA itself can be enhanced. In a study by Marta Madaghiele, PEGDA cryogels were synthesised at varying concentrations using UV irradiation for fast cryopolymerization of 30 or 60 seconds (Madaghiele et al., 2018). The mechanical investigation revealed that the elastic modulus of the cryogels ranged from 10 to 158 kPa, with stiffness being exclusively dependent on PEGDA concentration, thereby underscoring the concentration as a pivotal factor in tailoring the mechanical properties of the cryogels.

Considered as physically incorporated gelatin hydrogel in PEGDA, the study of composite hydrogel of pure gelatin with PEGDA was limited. Freeze-drying as a technique to improve the mechanical properties of hybrid hydrogel has not been mentioned. In this study, a novel technique was used to prepare gelatin/PEGDA hybrid hydrogel to enhance incredible mechanical strength and maintain biocompatibility. Untreated gelatin and PEGDA were trapped together using freeze drying. The water within the IPN undergoes crystallization and subsequent withdrawal. The composite hydrogel exhibits the property of porosity. Then the cryopolymerization properties of PEGDA as

cryogels were used. The dry state hybrid hydrogel was UV-cured to maintain the physical crosslinking between PEGDA and untreated gelatin.

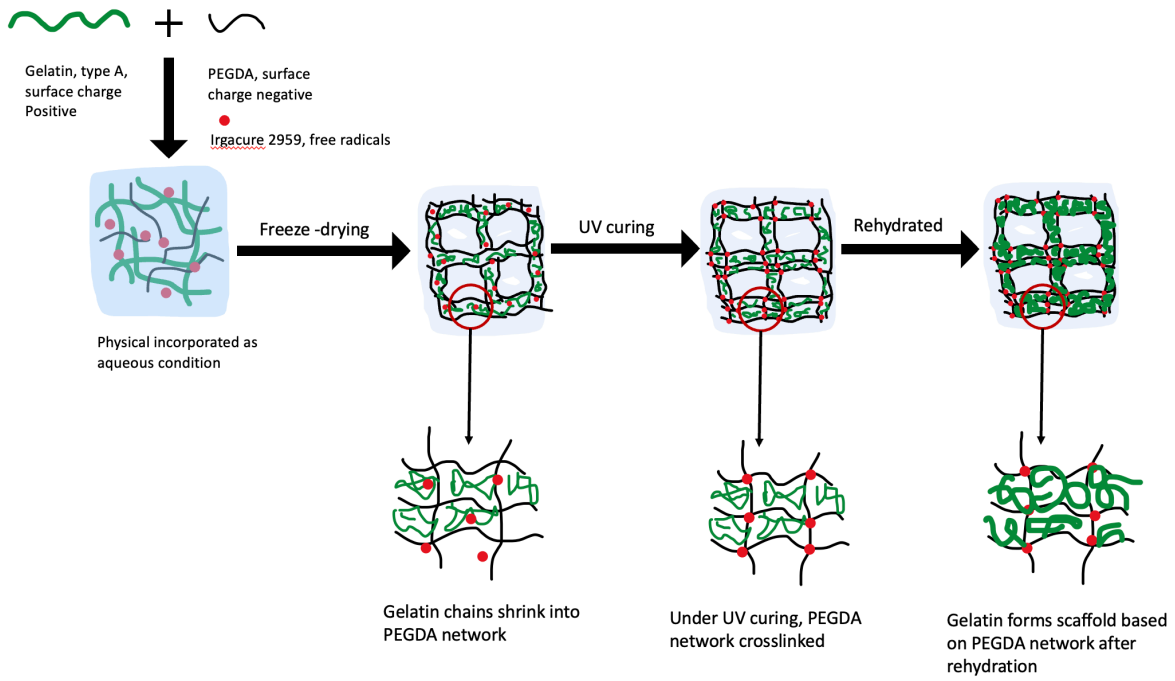

Figure 26 The scheme of dual freeze-drying crosslinking of gelatin and PEGDA

The process of preparing gelatin/PEGDA porous matric was described as Figure 26. The gelatin solution and PEGDA solution were physically mixed to form a homogeneous hydrogel. During the freeze-drying process, the solvent phase (deionised water) was crystallised and evacuated from the hydrogel. The polymer phase (gelatin & PEGDA) was separately left, enriched to form a porous network. Under this dry condition, the photopolymerisation of PEGDA formed a chemically cross-linked polymer network, which tightly locked incorporated gelatin. Dry state gelatin/PEGDA undergoes this dual freeze-dry technique and exhibits high tensile strength. Even after rehydrating, the swollen gelatin chain was limited by the cross-linked PEGDA network, avoiding to gradually diffusing into solvent. Meanwhile, the rehydrated gelatin/PEGDA matric keeps porous network constructed by UV-cured PEGDA.

5.2 Method

5.2.1 Materials

The hydrogel is prepared using gelatin from porcine skin (G1890, Sigma, UK), Poly(ethylene glycol) diacrylate (PEGDA, average Mn 700, acrylate, 100 ppm MEHQ as inhibitor, 300 ppm BHT as inhibitor), Irgacure 2959, 2-Hydroxy-4'-(2-hydroxyethoxy)-2-methylpropiophenone and purified water. Phosphate-buffered saline (PBS, Gibco™, pH 7.4) was used in rehydrating material.

5.2.2 Material preparation

In this study, an abbreviation is used to label the hydrogel solutions. G10%_P10% is abbreviated for 10 (w/v)% gelatin/ 10 (w/v)% PEGDA; G15%_P5% is abbreviated for 15 (w/v)% gelatin/ 5 (w/v)% PEGDA; and so on. Before use, PEGDA should be heated in the solution to a temperature of 25°C. Preparation of 10 mL 10 (w/v)% gelatin/ 10 (w/v)% PEGDA in purified water, with 0.5 (w/v)% Irgacure 2959 is done by mixing 1 g gelatin, 1 g PEGDA, 50 mg Irgacure 2959 with 8.88 g purified water. It should be noted that PEGDA is a solution with a 1.12 g/mL density at 25 °C. So at room temperature, 1g PEGDA takes 0.89 mL in the whole polymer volume. Preparation of 10 mL 15 (w/v)% gelatin/ 5 (w/v)% PEGDA in purified water, with 0.5 (w/v)% Irgacure 2959, is done by mixing 1.5 g gelatin, 0.5 g PEGDA, 50 mg Irgacure 2959 and 9.445 g purified water. It should be noted that at room temperature, 0.5g PEGDA takes 0.445 mL in whole polymer volume. All materials need to be dissolved under magnetic stirring of 300 rpm at 40 °C for 1h, avoiding light. Then the samples were cast into a dogbone shape silicon mould (as in section 3.2.1) and gelled at 4 °C to keep a stable gelation and for further use. The whole process need to be avoiding light.

Table 4 Different polymer compositions

Total polymer ration: 20 w/v%	Gelatin	PEGDA	The ratio of gelatin/PEGDA
G19%_P1%	19 w/v%	1 w/v%	* This group to examine the small amount of PEGDA
G16%_P4%	16 w/v%	4 w/v%	4:1
G15%_P5%	15 w/v%	5 w/v%	3:1
G13.3%_P6.6%	13.3 w/v%	6.6 w/v%	2:1
G10%_P10%	10 w/v%	10 w/v%	1:1
G6.6%_P13.3%	6.6 w/v%	13.3 w/v%	1:2
G5%_P15%	5 w/v%	15 w/v%	1:3
G4%_P16%	4 w/v%	16 w/v%	1:4
G1%_P19%	1 w/v%	19 w/v%	* This group to examine the small amount of gelatin.

10 (w/v)% gelatin and 10 (w/v)% PEGDA (polyethene glycol diacrylate) was prepared for the following comparison test. 0.5 (w/v) % Irgacure 2959 added as a photoinitiator to facilitate UV-initiated crosslinking. Three distinct crosslinking techniques were applied to this solution—traditional

crosslinking, freeze-drying with UV curing, and air-drying with UV curing—to evaluate each method's effect on the final material properties.

The first method, **Traditional Crosslinking**, involved directly exposing the solution to UV light to initiate crosslinking, producing a standard gelatin-based biomaterial that served as a baseline for comparison. The second method, Freeze-Dry with UV Curing, introduced an initial UV exposure to initiate crosslinking, followed by freeze-drying to remove moisture from the matrix. A second UV curing step was then applied to enhance crosslinking density, aiming to improve the structural integrity and stability of the biomaterial by creating a tighter network of crosslinked polymers. This dual-step process sought to provide a scaffold with enhanced mechanical properties while maintaining the structural framework critical for biomaterial applications. In the third method, Air-Dry with UV Curing, the solution was exposed to an initial UV curing step, followed by air-drying to allow for gradual moisture evaporation. A final UV exposure was then applied to complete the crosslinking process. This approach was developed as a potentially simpler alternative to freeze-drying, aiming to balance ease of fabrication with optimal mechanical strength in the resulting material. In the last two methods, drying and curing steps were exchanged to examine the effects of the water content for UV curing.

For UV curing step, the samples were UV cured in 10 mins under Cole-Parmer Handheld UV Lamp (6 Watt, 254/365 nm, AC Operated; 110 VAC, 50/60 Hz) with a distance of 1cm. For the freeze-drying process, the samples were frozen at -20°C for 24h and freeze-dried at a vacuum pressure of 0.05 bar at -80°C (Labconco FreeZone 4.5-Liter Benchtop Freeze Dryers) for 24h. For the airdrying process, the samples were airdried under a fume hood with a flowrate of 0.92 m/sec for 24h. All samples before UV-cured need to be avoiding light. The order of these steps for different groups is shown in Figure 27.

Following crosslinking, all samples were immersed in phosphate-buffered saline (PBS) at 37°C for 24 hours to reach water equilibrium. This step ensured that each biomaterial achieved a stable, hydrated state, mimicking physiological conditions and rendering the materials suitable for further testing and analysis. The process of all groups was described in Fig 26.

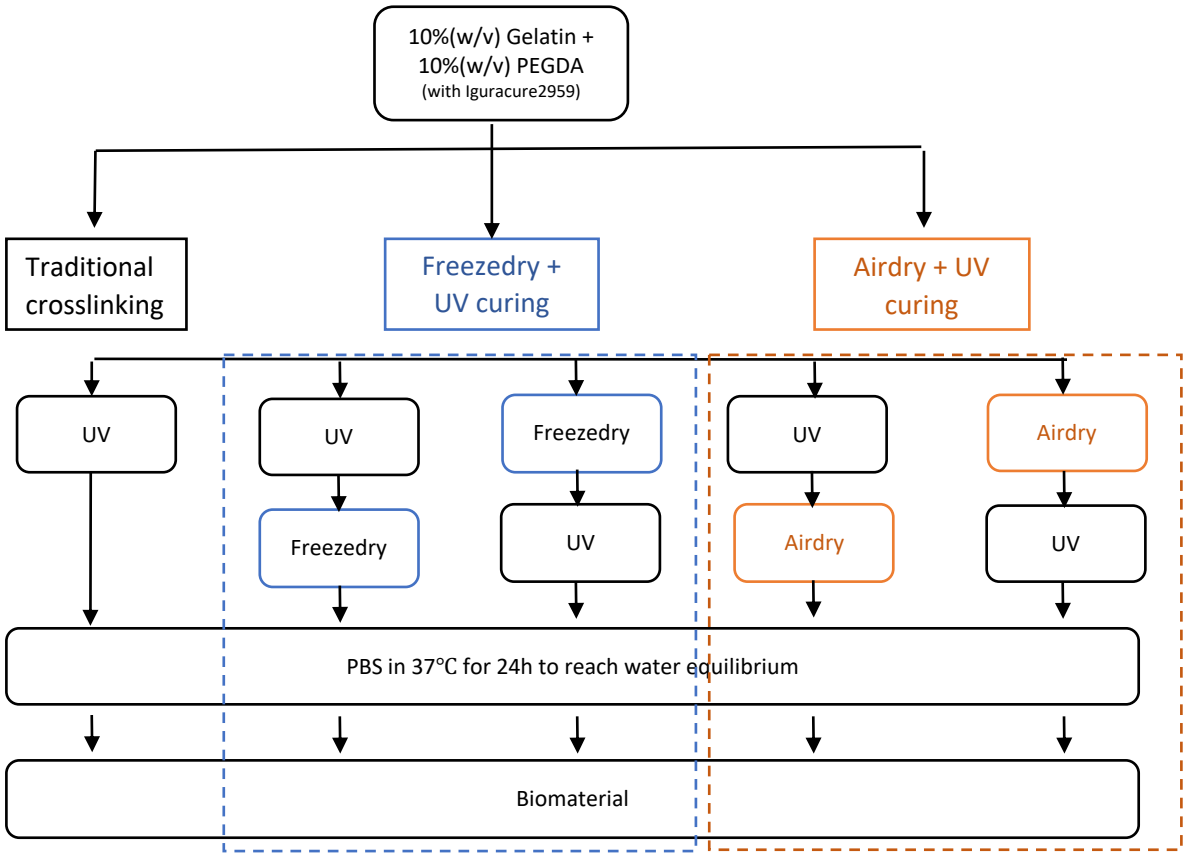

Figure 27 The process of preparing different crosslinking gelatin/PEGDA hydrogel

5.2.3 Study of factors affecting crosslinking

Several important factors affecting crosslinking were examined. To match the mechanical requirements of the small vascular tissue, the tensile strength, elongation at break, and Young's modulus were tested. Since the water content would affect the mechanical properties, samples were tested in dry conditions. Firstly, Gelatin and PEGDA concentrations are crucial as they directly affect the material's stiffness, elasticity, and tensile strength. Repeating crosslinking could result in a more resilient structure with increased mechanical strength due to the formation of additional bonds within the hydrogel matrix. However, excessive crosslinking might lead to brittleness, reducing the material's flexibility. The different types of gelatin could also affect the character of hybrid polymers. Since PEGDA is photocrosslinkable, upgrading gelatin into photocrosslinkable gelatin (GelMA) could increase the polymer density of hybrid polymers. Besides, changes in pH can influence the surface activity of gelatin molecules, resulting in changes to the material properties.

5.3 Results

5.3.1 Comparison of the effects of UV curing and different drying techniques on the mechanical properties of gelatine/PEGDA cushions

To investigate the impact of freeze-drying and UV cross-linking on the mechanical properties of a gelatin/PEGDA hybrid material (Fig 28, a), the Young's modulus was measured both before and after incubating the samples at 37 °C for 24 hours (Fig 28, b). For comparison, a control group consisting of physically mixed gelatin and PEGDA (Group A) was subjected to UV-curing. This control group exhibited poor mechanical strength, lower than the other composite, and disintegrated completely when immersed under 37°C due to its loosely structured gelatin.

By adding freeze-drying and photopolymerization, we observed a significant improvement in mechanical strength. Regardless of the order of UV-curing and freeze-drying, the Young's modulus of the hybrid materials approached 100 MPa. However, differences emerged after immersion in PBS solution. The UV-then-freeze-dry group (Group B) maintained its shape post-incubation but was weak for mechanical test. In contrast, the freeze-dry-then-UV group (Group C) displayed a Young's modulus of up to 5 MPa, even though this was significantly reduced compared to its dry state. The maintenance of mechanical strength is highly beneficial for cell seeding applications. Similarly, in the air-dry group, the UV-then-air-dry group (Group D) showed Young's modulus comparable to those achieved through freeze-drying, exceeding 100 MPa. However, upon immersion, these structures disintegrated. Conversely, the air-dry-then-UV group (group E) experienced a reduction in Young's modulus from 4 MPa to 2 MPa after immersion.

Samples from all five groups with a cube with around 25mg were immersed in dH2O. The gelatin concentration released was determined via BCA assay (Bicinchoninic acid kit for protein, Pierce, USA). The standard curve was established using gelatin solution in dH2O with concentrations of 1500, 1000, 500, 250, 125, 62.5 ug/mL ($Y=215.2-329.3*x+225.9*X2$ $R^2=0.9837$). The released gelatin concentration was in correspondence with the mechanical tests (Fig 28, c). Groups A and B both released more than half of the gelatin. Consequently, they relied solely on the PEGDA network to maintain their shape, but at the expense of mechanical strength. In contrast, Group C released significantly less gelatin than the other groups, resulting in the highest mechanical strength with a difference that was statistically significant. On the other hand, Group D released a far greater amount of gelatin compared to other groups, causing the samples to dissolve entirely with a difference that was statistically significant. As for Group E, it released gelatin at rates similar to Groups A and B; however, the air-drying process allowed the remaining gelatin to integrate with the PEGDA network, thereby preserving some mechanical strength. Mechanistically, free radicals activated by UV light can integrate PEGDA but not gelatin into an interpenetrating polymer network (IPN); they merely result in a physical mixture. The physical mixed hybrid hydrogel undergoes any drying technique merely for removing the solvents. Unexpectedly, pre-drying before UV cross-linking effectively compacts the chemical chains of PEGDA and gelatin, which can be described as a physical crosslinking. Subsequent UV exposure enables the free radicals to form a robust network with PEGDA, locking the gelatin into place,

enhancing the physical crosslinking. Among the drying methods, freeze-drying was found to result in a tighter intermolecular network than air-drying, due to the cryopolymerization of PEGDA.

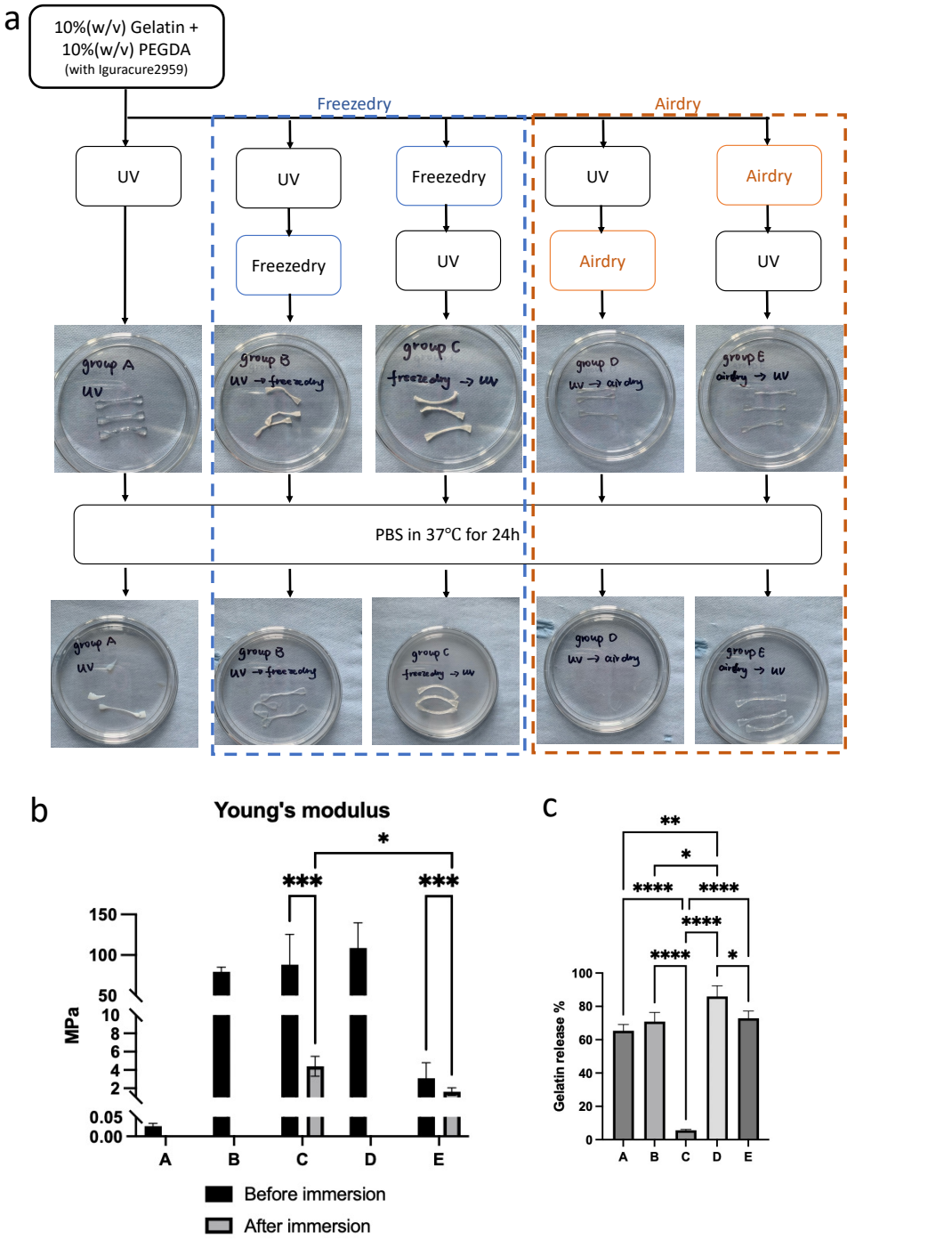

Figure 28 Preliminary experiments were exploring the method of preparing gelatin/PEGDA matrix. a) Visual presentation of five different groups of preparing gelatin/PEGDA matrix techniques, b) Young's modulus of the five groups of materials before and after immersion; c) Different gelatin release percentages of five groups after immersion group with different UV curing sequences.

5.3.2 The effect of different proportions of gelatin with PEGDA

To investigate the effects of varying concentrations of gelatin and PEGDA on hybrid materials using the Dual Freeze-Dry UV technique, the concentrations were adjusted as follows: using G5%_P5% as control group, gelatin was increased to 10% and 20% (Fig 29 a), PEGDA was raised to 10% and 20% (Fig 29 b), and both were increased simultaneously (Fig 29 c). These samples were then evaluated for Young's modulus and stress-strain curve. The results indicated a statistically significant variation with gelatin concentration changes. Specifically, elevating the gelatin concentration from 5% to 10% and 20% enhanced tensile strength while reducing strain. On the other hand, adjusting the PEGDA concentration did not significantly impact the Young's modulus. Only the G5%_P20% group exhibited lower tensile strength and elongation at break. Moreover, the curve also showed a general trend: as the concentration of the overall material increased, tensile strength improved.

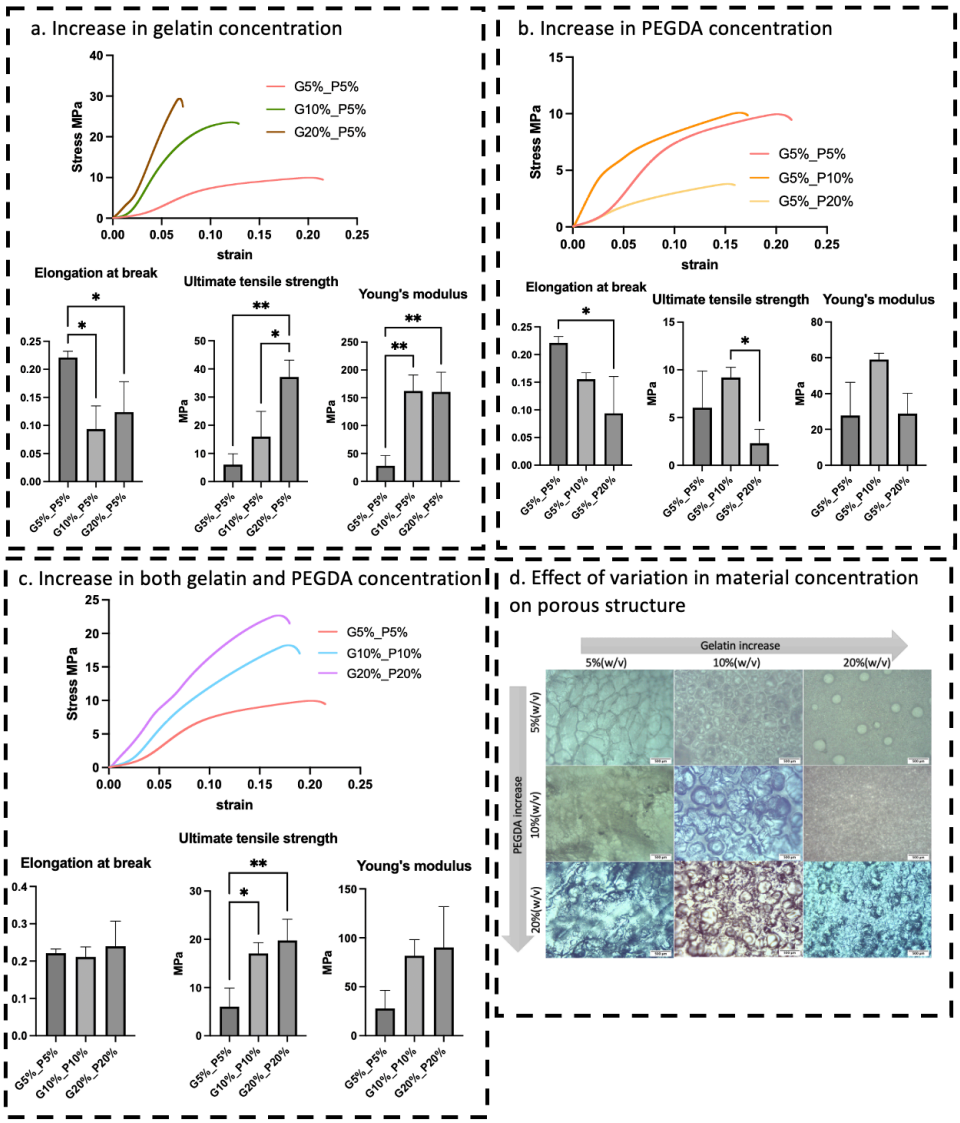

Figure 29 Effect of different concentrations of gelatin or PEGDA on the mechanical strength of the material. a) Increasing gelatin concentration decreases elongation at break and increases ultimate strength; b) Increasing

PEGDA concentration decreases elongation. c) Increasing gelatin and PEGDA in the same time. d) optical images that show the surface diversity of the different concentrations of gelatin and PEGDA. Scale bar: 500 µm.

The blend consists of four main components: gelatin, PEGDA, Irgacure 2959, and water. During the pre-freezing process, the water's solidifying crystals expel both the polymer precursor and Irgacure 2959. Concurrently, the chains of gelatin and PEGDA contract and become concentrated in the remaining liquid phase. The vacuum pressure applied in the freeze-drying process not only removes the water crystals but also intensifies the entanglement of the Gelatin and PEGDA chains. This results in hybrid gels that boast a highly interconnected macroporous structure with rigid pore walls. Furthermore, when subjected to UV light, crosslinking reactions take place within these PEGDA networks, leading to chemical crosslinking. This process solidifies the macroporous structure and secures the gelatin within the PEGDA network. The mechanical property of this hybrid material, derived from the blend of gelatin and PEGDA, is influenced by the dual freeze-dry UV crosslinking technique. This strength is primarily attributed to the rigid pore walls, determined by the ratio of gelatin concentration to the PEGDA network. The porous structure is also related to the concentration of the two materials. Observations under an optical microscope revealed that gelatin and PEGDA influence the material's void structure differently (Fig 29 d). As the concentration of gelatin rises and the concentration of PEGDA is fixed, the size of each void decreases, but their number increases. That means the total void volume increases. The increase of gelatin leads to more voids in this scaffold. Conversely, a higher concentration of PEGDA with a fixed concentration of gelatin reduces the number of void structures. The entire scaffold becomes a nearly solid state. When both gelatin and PEGDA concentrations are increased simultaneously, the size and number of voids decline. This situation could be connected to the density of the PEGDA network. Gelatin contributes to the pore structure, while the PEGDA network density influences the walls of this structure.

5.3.3 The effect of secondary dual freeze-dry UV crosslinking

When examining the structure of mixed materials containing low concentrations of gelatin and PEGDA, significant void structures were observed. These voids offer the potential for secondary dual freeze-dry UV crosslinking.

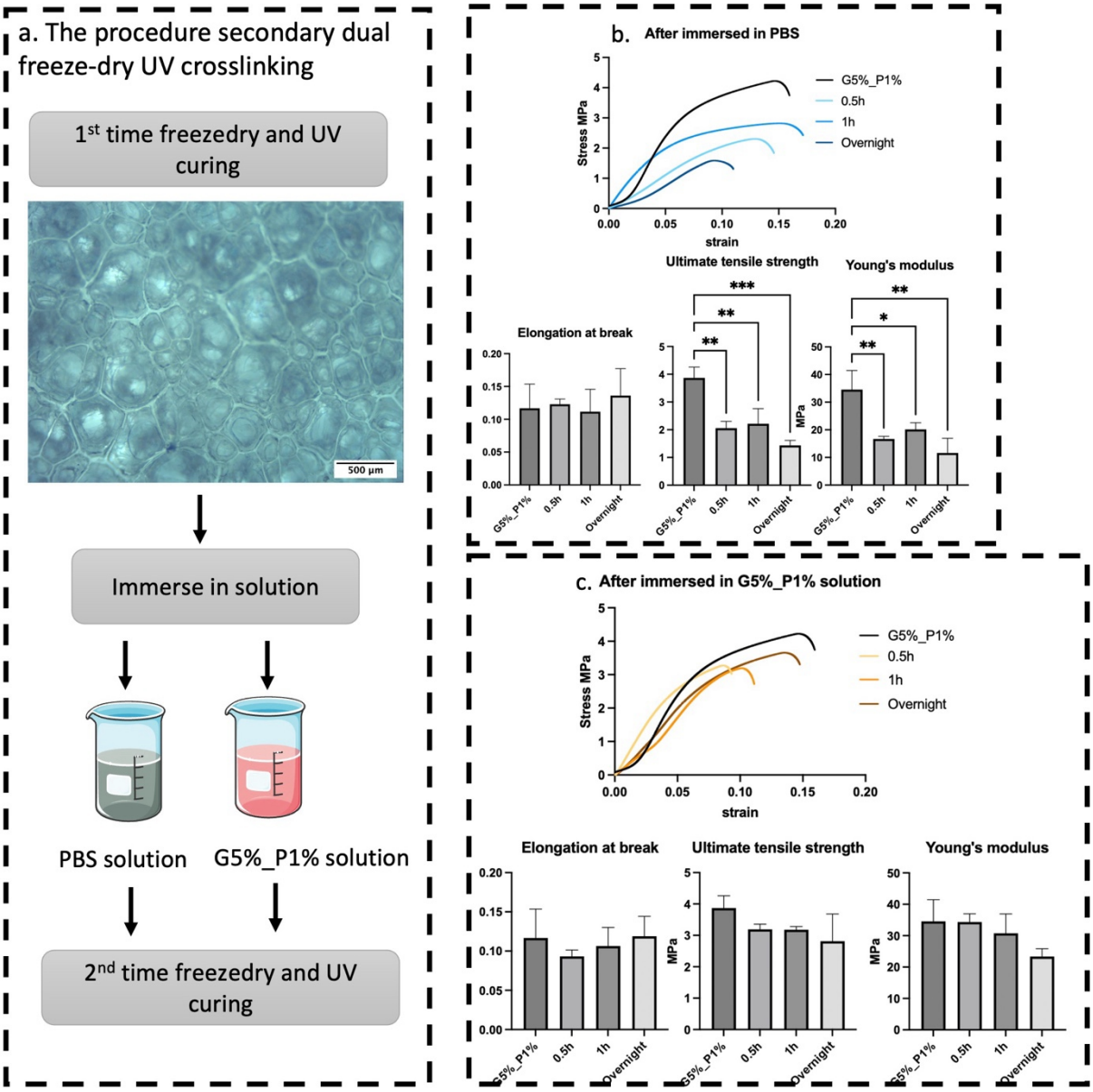

Figure 30 Examination of secondary Freeze-drying UV curing. a) For materials that have been dual freeze-drying UV crosslinking rehydrate after re-freezedrying-UV-crosslinking; with PBS solution, rehydrate the mechanical strength of the matrix. (b) The mechanical stress strength of the matrix is inevitably reduced, and the mechanical strength of the matrix rehydrated with gelatin/PEGDA solution (c) remains unchanged.

To investigate the effects of multiple crosslinking, the dual freeze-dry UV crosslinked G5%_P1% material was soaked in two distinct solutions (Fig 30 a): PBS solution and a G5%_P1% solution identical to the crosslinked material. Following immersion, the material underwent another round of dual freeze-dry UV cross-linking. It was noted that the material's mechanical strength decreased after re-crosslinking post-immersion in PBS (Fig 30 b). However, when soaked in the G5%_P1% solution, the material's mechanical properties remained consistent (Fig 30 c). During the immersion phase, the material absorbs water, causing the gelatin chain to loosen compared to its dry state. This leads to a loss of some gelatin content. Even after a subsequent freeze-drying process, the material's mechanical strength diminishes. However, when immersed in the G5%_P1% solution, the lost gelatin is replenished,

maintaining the material's mechanical strength. It's also evident from secondary dual freeze-drying UV crosslinking that existing freeze-dried UV crosslinked structures remain unaffected by additional freeze-drying.

5.3.4 The effect of hybrid material compositions

The mechanical strength of the hybrid material is influenced by the type of gelatin and the composition of the PEGDA network, both of which are key components of the rigid pore walls. Using a G10%_P10% mix of type A gelatin as the control group, type A was substituted with a softer type B gelatin and a UV-crosslinkable GelMA modified from type A gelatin (Fig 31 a).

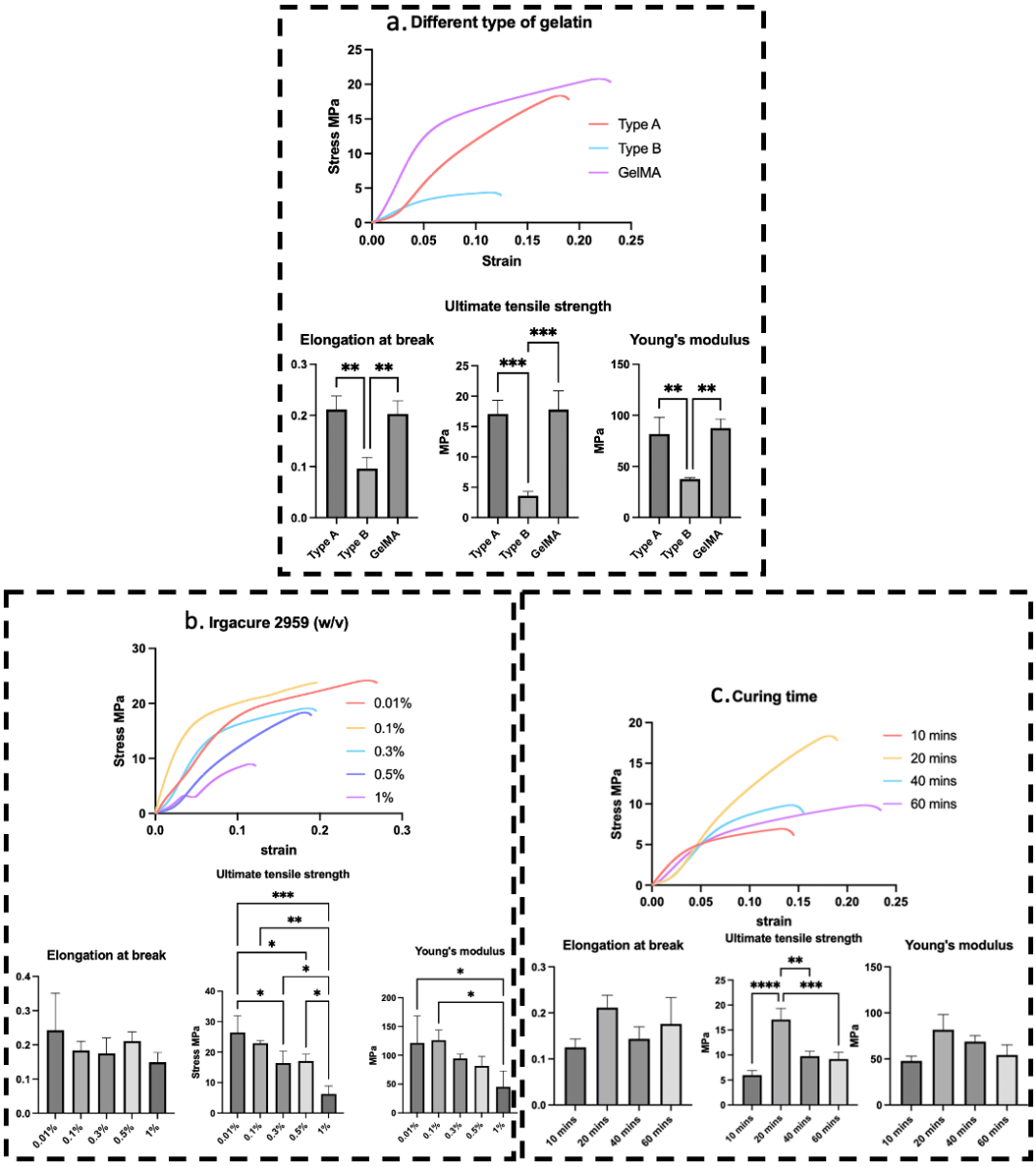

Figure 31 The effects of gelatin type, PI concentration, and UV curing time on the mechanical strength of matrix. a) Three different types of gelatin were mixed with 10% (w/v) PEGDA at 10% (w/v) concentration after dual freezedry UV curing crosslinked; the mechanical strength of type B gelatin was the weakest; b) based on G10%_P10%, the UV curing time was fixed at 20mins, and the mechanical strength was decreased by increasing

the concentration of PI; c) the mechanical strength was also decreased by increasing the light time when the concentration of PI was kept constant at 0.1% (w/v).

The type B gelatin exhibited reduced elongation at break and diminished tensile strength, distinctly setting it apart from the other two groups. While there was no significant difference in mechanical strength between Type A and GelMA, the stress-strain curve revealed that the GelMA group had slightly superior stress and strain levels. Elongation at break remained relatively consistent as the PI concentration increased, but mechanical strength decreased. Notably, materials with a high concentration of 1 (w/v)% were more brittle due to the surplus of free radicals, which result in a shorter PEGDA chain formation. The duration of curing, which impacts the PEGDA network formation, also affects the material's strength. As the material turns, porous and white post-freeze-drying, UV curing is applied to both sides, with 10 minutes of curing translating to 5 minutes on each side. UV curing didn't alter the Young's modulus. However, materials subjected to 20-minute curing exhibited superior tensile strength. This could be attributed to the extended UV exposure and heating durations. The gelatin matrix's stability is predominantly due to hydrogen bonds. Heating compromises these bonds, undermining the gel's structural integrity. Exposing gelatin to extreme temperatures can lead to protein chain denaturation, causing them to lose their inherent structure. Once denatured, these proteins might cluster together, forming larger aggregates, and this alteration may not revert upon cooling.

5.3.5 The effect of solvent pH on gelatin/PEGDA matrix

During freeze-drying, the gelatin and PEGDA chains collapse, despite the absence of a direct chemical reaction between them. This contraction may result from surface charge difference. Consequently, the solvent pH plays a role in determining the hybrid material's strength. The G10%_P10% mix of Type A gelatin with PEGDA in distilled water (pH 7) served as the control group (Fig 32 a). The solvent pH was altered using HCl and NaOH, and similar tests were conducted on Type B gelatin (Fig 32 b), as well as the G15%_P5% (Fig 32 c) and G5%_P15% groups (Fig 32 d).

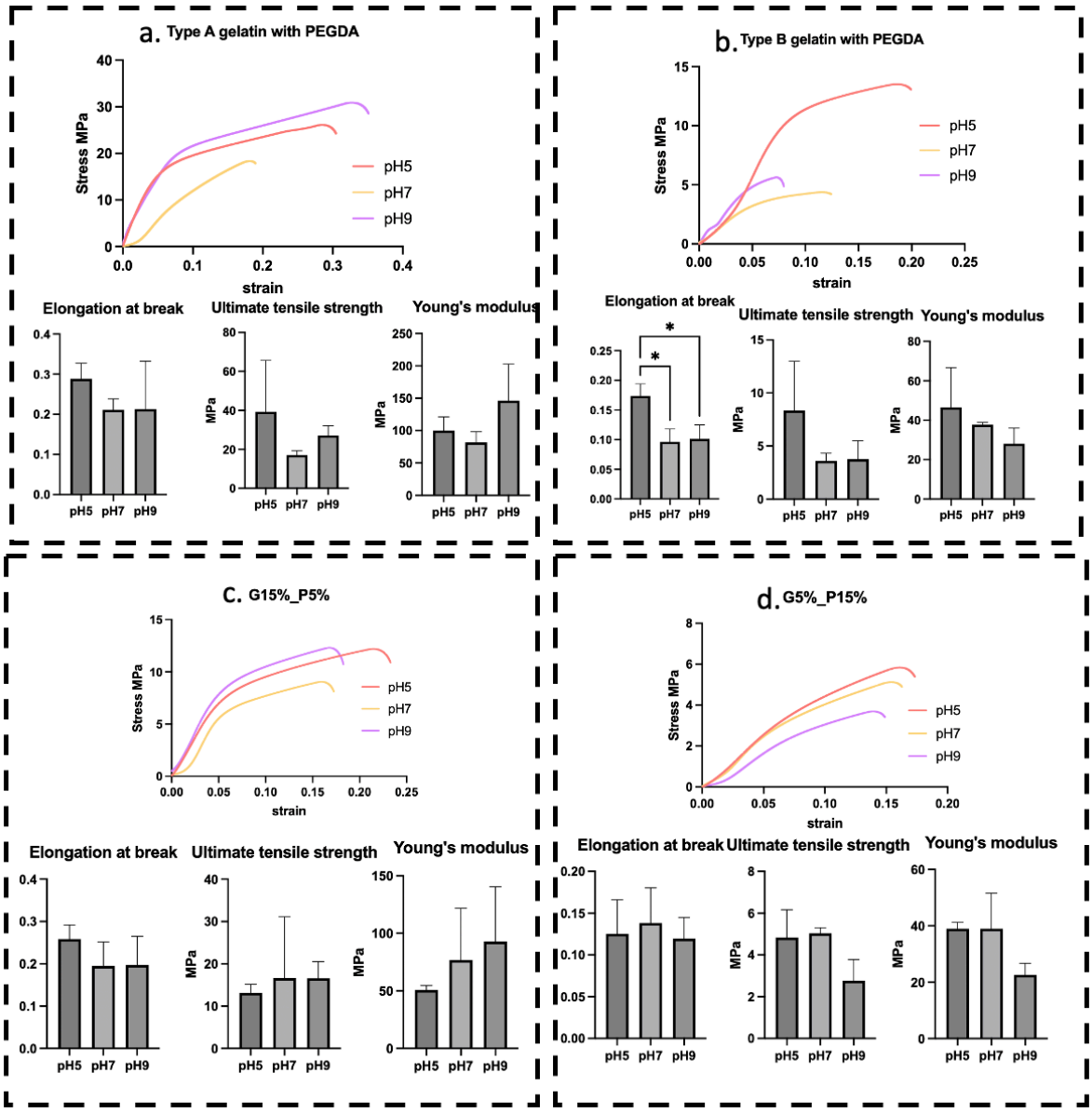

Figure 32 Effect of Solvent pH on Matrix Strength. Variations in solvent pH influence the surface charge, affecting the gelatin-PEGDA linkage and mechanical strength. With a constant G10%_P10% concentration, strength differed based on gelatin type and pH. Type A gelatin had the highest strength at pH 9, while type B peaked at pH 5. Gelatin and PEGDA interactions depend on their concentrations; for instance, increasing type A gelatin with PEGDA reduces strength at pH 5, whereas higher PEGDA concentrations decrease strength at pH 9.

Most groups displayed no significant differences in strength, likely due to the solution's acidity not being potent enough to influence the hydrogel's strength. Notably, only in solutions with pH2 and pH12 were there observed alterations in the hydrogel structure. Within the Type A gelatin group, the maximum Young's modulus was achieved at a solvent pH of 9. Conversely, in the Type B gelatin group, the material exhibited the greatest elongation at break at pH 5. For a weight ratio of 1:1, the strength of Type A gelatin at pH 9 surpassed that of Type B gelatin. Post pH 9, Type A gelatin attains isoelectronic sites, enhancing the chain interaction within the hydrogel. Type B gelatin demonstrates the similar enhancing but at pH 5. For the G15%_P5% group, the Young's modulus augments with pH, whereas in

the G5%_P15% group, it intensifies with elevating pH but is at its nadir when the pH reaches 9. This variation could be attributed to the combined influences of surface charge and surface electron adsorption modulated by pH. In the G15%_P5% group, with a higher gelatin percentage and a reduced pH, the gelatin has a positive surface charge. This causes repulsion, reducing the chain entanglement. In the G5%_P15% group, where the gelatin content is diminished, the gelatin repulsion due to the lower pH is attenuated. However, a heightened pH could affect PEGDA. Existing research lacks data on PEGDA's surface charge, but it has been noted that PEGDA's aqueous solution holds a negative zeta potential. In high pH conditions with elevated PEGDA content, the adhesive strength of the PEGDA network to gelatin might be hindered.

5.4 Discussion

Gelatin, the most widely used material in tissue engineering, is limited by its weak mechanical strength. Based on the contribution of PEGDA to the mechanical strength and stability of the material structure, it is not surprising that PEGDA is often chosen for applications in blends with other materials, especially natural materials like gelatin with weak mechanical strength. This study provides a novel technique for crosslinking gelatin and PEGDA. Freeze-drying and then UV curing was used to physically compress the material structure before locking it with photocrosslinking. It combines the mechanical strength of PEGDA network with the porous structure of gelatin. The mechanical strength and void structure of this matrix are influenced by changes in the concentration of gelatin or PEGDA. Conditions included the type of gelatin, the concentration of PI, and UV curing time also impact the matrix's mechanical strength. While the exact mechanism of gelatin and PEGDA linking within the matrix remains unexplored, this study suggests it may be linked to their surface charges. Notably, the surface charge of gelatin varies with the solvent pH.

Cryogels have emerged as a significant focus in biomaterials research, particularly for their unique properties and applications in tissue engineering and regenerative medicine. Cryogels, as defined by their macroporous structure and ability to retain high water content, allow for enhanced cellular interactions and nutrient transport, making them ideal for various biomedical applications. Among the diverse types of cryogels, those synthesised from poly(vinyl alcohol) (PVA) and poly(ethylene glycol) diacrylate (PEGDA) have gained considerable attention due to their mechanical properties and biocompatibility. Cryogels are synthesised via cryogelation, a process that involves freeze-thaw cycles leading to aggregation cross-linking of polymers. Rodrigues et al. (2013) emphasise the significance of cryogels made from collagen and nanohydroxyapatite (HA) for bone repair, highlighting their mechanical properties and ability to promote cell adhesion and proliferation, which are essential for effective biomaterial applications in tissue engineering. Similarly, the mechanical anisotropy of PVA cryogels can be enhanced through freeze/thaw cycles, making them suitable for mimicking soft tissues (Dubbin et al., 2017). This aligns with findings from Hu et al. (2013), who

optimised PVA cryogels for liver elastography, indicating the potential for tailoring mechanical properties to replicate various biological tissues. The versatility of PEGDA cryogels is also notable, particularly in the context of photocrosslinking. Jin et al. (2015) explore the integration of conductive materials into PEGDA cryogels for cardiac applications, discussing the challenges of UV crosslinking and how the addition of gelatin can improve cryogel properties. In this research, freeze-drying is innovatively used as an enhanced form of freezing, with water or ice playing a crucial role in the formation of the cryogel structure by facilitating the gathering and linking of the polymer network. By first removing the water through freeze-drying and then crosslinking the gelatin/PEGDA composite, this approach effectively improves the mechanical properties of the material, as demonstrated in the air-dried group. Furthermore, applying a vacuum pressure of 0.05 mbar during the freeze-drying process yields optimal results, enhancing the structural integrity of the cryogel.

The role of gelatin is particularly essential in this freeze-drying process due to the low freezing point of PEGDA, which would otherwise hinder the formation of a stable frozen matrix. Gelatin not only stabilises the freezing process but also transforms the material's temperature sensitivity into an advantage, promoting the formation of a well-defined hydrogel structure under freeze-drying conditions. This technique highlights the benefits of integrating gelatin for its role in freezing support, which, combined with the controlled environment of freeze-drying, facilitates a robust hydrogel with enhanced mechanical properties suitable for various biomedical applications.

The dual freeze-drying crosslinking approach for gelatin/PEGDA is regarded as a form of physical crosslinking, where no chemical bonds are formed between the two materials to create a polymer network. Instead, one plausible explanation for the observed structural integrity is phase separation. Phase separation phenomena in polymer blends, such as those observed here, are critical for influencing the material's mechanical properties by inducing microstructural organisation and distribution of components. Supporting this concept, Brennan Bailey's research on PEGDA hydrogels, produced using the solvent-induced phase separation (SIPS) method, demonstrated that phase separation techniques can yield hydrogels with adjustable physical properties, including macroporous morphology, increased modulus, and faster degradation rates—all properties that enhance their suitability for tissue engineering applications. However, the applicability of these findings to the gelatin/PEGDA system requires further experimental validation and characterisation. Moreover, tests such as the small-angle neutron scattering (SANS) analysis utilised by Shibayama (2011) to study phase behaviour in polymer gels provide a powerful foundation for investigating material inhomogeneities and understanding crosslinking mechanisms. Applying similar techniques to the gelatin/PEGDA system could yield valuable insights into the structural organisation and the phase separation dynamics within the cryogel, ultimately aiding in optimising the material for biomedical applications by revealing its detailed internal morphology and performance under stress.

In this chapter, all mechanical tests were conducted while the material was in a dry state to keep all material in its original condition after dual freeze-drying crosslinking, which avoids the effect of rehydration degree. The main ultimate tensile strength and Young's modulus were summarised in Table 5. However, the biomaterial applied in tissue engineering should achieve a water equilibrium. To be specific, all materials need to be immersed in a suitable solution, including PBS solution or cell culture medium. Based on Fig. 28 b, the Young's modulus of gelatin/PEGDA scaffold decreased after immersion, which could be affected by the swollen chain of gelatin. Therefore, to further use it as a biomaterial, the relevant tests, including biodegradation, water absorption ratio, and cell attachment, were investigated in Chapter 6.

Table 5 Summarisation of ultimate tensile strength and Young's modulus of gelatin/PEGDA in dry state

Figure citation	Gelatin w/v%	PEGDA w/v%	Irgacure 2958 w/v%	Curing time(mins)	other conditions	Ultimate tensile strength (MPa)	Young's modulus (MPa)
Figure 28 a: increasing gelatin concentration	5	5	0.5	20	-	6.032±3.847	27.79±18.49
	5	10	0.5	20	-	15.98±8.963	162.1±28.85
	5	20	0.5	20	-	37.15±5.984	160.5±35.55
Figure 28 b: increasing PEGDA concentration	10	5	0.5	20	-	9.198±1.055	59.05±3.497
	20	5	0.5	20	-	2.304±1.465	28.78±11.32
Figure 28 c: increasing gelatin and PEGDA in the same time.	10	10	0.5	20	-	17.07±2.257	81.74±16.4
	20	20	0.5	20		19.76±4.403	90.17±41.59
Figure 30 a: different type of gelatin	10	10	0.5	20	type B gelatin	3.603±0.7107	37.68±1.197
	10	10	0.5	20	GelMA	17.77±3.083	87.57±8.839
Figure 30 b: increasing the concentration of PI	10	10	0.01	20		26.42±5.52	121.7±46.85
	10	10	0.1	20		22.88±0.9415	126.2±17.84
	10	10	0.3	20		16.46±3.875	94.52±7.485
	10	10	1	20		6.252±2.615	45.18±27.48
Figure 30 c: increading curing time	10	10	0.5	10		5.961±0.9333	47.78±5.31
	10	10	0.5	40		9.755±0.9982	68.72±6.498
	10	10	0.5	60		9.15±1.384	54.31±10.89
Figure 31 a: effect of Solvent pH in G10%_P10%	10	10	0.5	20	pH 5	39.24±26.39	100±21.14
	10	10	0.5	20	pH 9	27.14±4.951	146.2±56.46
Figure 31 b: effect of Solvent pH in G10%_P10% with type B gelatin	10	10	0.5	20	pH 5 - type B gelatin	8.341±4.645	46.5±20.14
	10	10	0.5	20	pH 9 - type B gelatin	3.76±1.747	28.13±7.903
Figure 31 c: effect of Solvent pH in G15%_P5%	15	5	0.5	20	pH 5	13.12±2.029	50.78±3.898
	15	5	0.5	20	pH 7	16.65±14.45	76.87±44.8
	15	5	0.5	20	pH 9	16.59±3.912	92.86±47.57
Figure 31 d: effect of Solvent pH in G5%_P15%	5	15	0.5	20	pH 5	4.829±1.336	38.99±2.255
	5	15	0.5	20	pH 7	5.027±0.2794	38.96±12.66
	5	15	0.5	20	pH 9	2.76±1.022	22.61±4.104

6. Constructing a macro-micro vascular network

This chapter, the pivotal component of this PhD research, focuses on developing a macro-micro vascular network. It is organised into two main sections. In the first section, gelatin/PEGDA material (from Chapter 5) was used with rotational printing techniques (Chapter 4) to fabricate small-diameter tubes (0.7mm, 1.4mm, and 2mm). Among these, the 0.7mm diameter tubes were selected for further analysis, where DAPI staining revealed the formation of a microvascular network by cultivating HUVECs along these tubular structures.

The second section introduces the fabrication of even smaller pipe structures, with diameters as low as 0.07mm, created using extrusion printing with a DNA hydrogel provided by Tsinghua University. This study thus spans a range of pipe sizes (0.07-2mm), addressing dimensions often overlooked in prior research due to material or technical limitations. Together, these findings contribute to advancing the field of tissue-engineered vascular structures.

6.1 Microvasculature in tissue engineering

Microvasculature, in tissue engineering, microvasculature is commonly regarded as describing lumenised structures with a diameter under 100 um. However, in biology, microvasculature refers to the micro-vessels within which solute exchanges take place between the blood and surrounding tissues. This is mainly done through the endothelium, and as a biologically-regulated function, is one of the main limitations of purely engineered micro-vessels. Therefore, in this research, the link between artificial vasculature and the biological vasculature network was established.

Microvasculature—including arterioles, capillaries, and venules—plays a crucial role in cellular health by enabling the exchange of oxygen, carbon dioxide, nutrients, endocrine signals, and waste products with surrounding cells. This continuous exchange supports cellular function across tissues; cells can become dysfunctional or die without sufficient microvasculature. Given the need for this intricate network to permeate tissues fully, replicating microvasculature in vitro has posed significant challenges, but its successful development holds enormous potential for tissue engineering, organ repair, and drug screening.

Traditionally, microvasculature in vitro has been created using microfluidic devices, which rely on standard microfabrication techniques like thin-film deposition, lithography, and etching. One approach with microfluidics involves seeding endothelial cells in microchannels to form simple microvascular structures. However, constructing a 3D microvasculature network often requires a time-intensive layer-by-layer assembly process, which is prone to structural issues like delamination. An

alternative strategy is to emulate physiological environments within microfluidic devices by perfusing culture medium through parallel microchannels, encouraging the assembly of endothelial cells in a hydrogel matrix between them. Yet, this approach has limitations: the resulting microvasculature structure lacks control, and the hydrogels used are often restricted to natural options like fibrin and collagen, which limit customizability.

A different, innovative approach to creating microvasculature utilises sacrificial printing techniques. Here, rigid filaments—made from materials like gelatin, sugar, shellac, PNIPAM, and Pluronic F127—are printed within a hydrogel matrix and later removed, leaving hollow channels to serve as rudimentary microvascular structures. The flexibility of 3D printing enables a variety of designs; however, these techniques traditionally involve a two-step process: forming the hollow channels first, followed by cell seeding (Seymour et al., 2022). This sequence introduces challenges in spatial and density control of cells within channels. Additionally, perfusing cells into these microchannels can lead to low reproducibility due to poor cell adhesion and structural integrity issues, especially when fabricating endothelialised microvasculature with diameters under 100 μm.

This research begins with investigating improvements in the mechanical strength of gelatin/PEGDA hydrogels by dual freeze-drying crosslinking. To validate their potential for tissue engineering, the biocompatibility was evaluated. Then, using rotational bioprinting, small vascular structures with a 0.7mm diameter was fabricated and cultured, achieving a robust macro-micro vascular structure. These findings advance the field of engineered vascular systems, bringing us closer to replicating functional, integrated microvasculature in tissue constructs.

6.2 Method to prepare gelatin/PEGDA

6.2.1 Material preparation

In this chapter, materials were selected based on optimized findings from Chapter 5, where a total polymer weight percentage of 20% was determined to be ideal. Various ratios of gelatin and PEGDA were prepared to examine the effects of different polymer compositions on material properties. Formulations included extremes such as G19%_P1%, with predominantly gelatin content, and G1%_P19%, with predominantly PEGDA, to capture a range of assay conditions and better understand the behaviour of these materials. Across all groups, the photoinitiator Irgacure 2959 was consistently used at a concentration of 0.1% w/v, a concentration validated by Chapter 5 for effective crosslinking.

Hydrogel samples were initially prepared as the hydrogel solution, then gelled, then frozen and freeze-dried to ensure stability and structural consistency with a slow and stable decreased temperature. This process began with cooling each sample at 4°C for 10 minutes, followed by freezing at -20°C overnight to facilitate even solidification. The samples were then lyophilised under a vacuum pressure of 0.05 mbar at -80°C, a protocol adapted from Chapter 5. One sample from the G1%_P19% group

fractured during lyophilisation and was therefore excluded from subsequent analyses. Finally, all samples were exposed to 20 minutes of UV curing to complete the hydrogel crosslinking. This curing duration was established in Chapter 5 as optimal for achieving consistent crosslinking and ensuring reproducible mechanical and biochemical properties across all sample groups.

In this chapter, since the gelatin/PEGDA matrix is used as a biomaterial, all samples were tested after reaching the water equilibrium. The mechanical test, the gelatin release, the degradation and the water swelling ratio were conducted in Chapter 3.

6.2.2 Seeding human umbilical vein endothelial cells (HUVECs)

Three groups of gelatin/PEGDA matrix were chosen for the biological test. G10%_P10% represents the high mechanical property; G15%_P5% represents the high ratio of gelatin; G5%_P15% represents the high ratio of PEGDA. The samples were prepared as a film of 1mm X 1mm X 0.2mm and autoclaved in freeze-dried and UV-cured conditions. After the autoclave, the samples were placed in a 24 well plate and immersed in a cell culture medium for cell seeding. $1X10^6$ cells per well were seeded upon the samples. After one day of culturing, the samples were removed into a new well-plate for further culture. Several samples were prepared for different culture time. The DAPI staining was used for HUVECs.

6.2.3 Rotational dipping of gelatin/PEGDA solution

According to the mechanical properties and the biological results, G10%_P10% was chosen for fabricating the small vascular structure. The process of fabricating the small vascular structure of gelatin/PEGDA is described as follows Figure 33. The G10%_P10% solution was prepared as in Chapter 5 and kept at 37°C. According to Chapter 4, 1V of the voltage of the motor (around 500 rpm) was tested. The needle was loaded into the motor and immersed in the gelatin/PEGDA solution for 5 minutes (Fig 33 a). After this, the needle was removed from the solution and kept at 4°C for 10 minutes (Fig 33 b). The needles covered by gelatin/PEGDA material were frozen at -20°C overnight and freeze-dried at -80°C under 0.05 bar for 24 hours (Fig 33 c). After freeze-drying, the gelatin/PEGDA tubular structure was easily removed from the needle and exposed to 365nm UV light for 10 minutes on each side. The tubular structure can be stored in a dry state for further use. For biological test, the HUVECs cells were seeded around the tube and cultured for 7 day for DAPI staining.

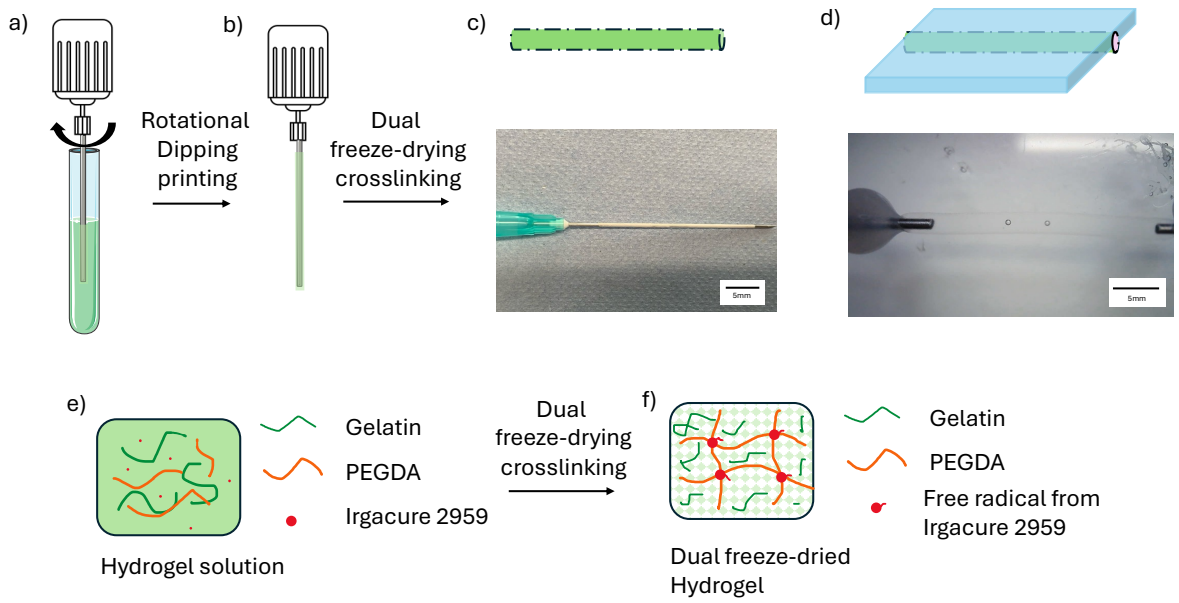

Figure 33 Process and Structural Representation of Gelatin-PEGDA Hydrogel Formation and Characterization.

6.3 Results of small vascular structure

6.3.1 Mechanical properties

Upon examination of the stress-strain curve, it is evident that the sample with high ratio of gelatin to PEGDA exhibited a lower strain at failure, suggesting a brittle material characteristic. Conversely, the sample with high ratio of PEGDA to gelatin demonstrated a significantly higher strain at failure, indicating enhanced ductility and suggesting that increased PEGDA content correlates with more excellent material elasticity. Matched with the result of Chapter 5, the hydrogel exhibited balanced mechanical properties when the ratio of gelatin/EPGDA was 1:1.

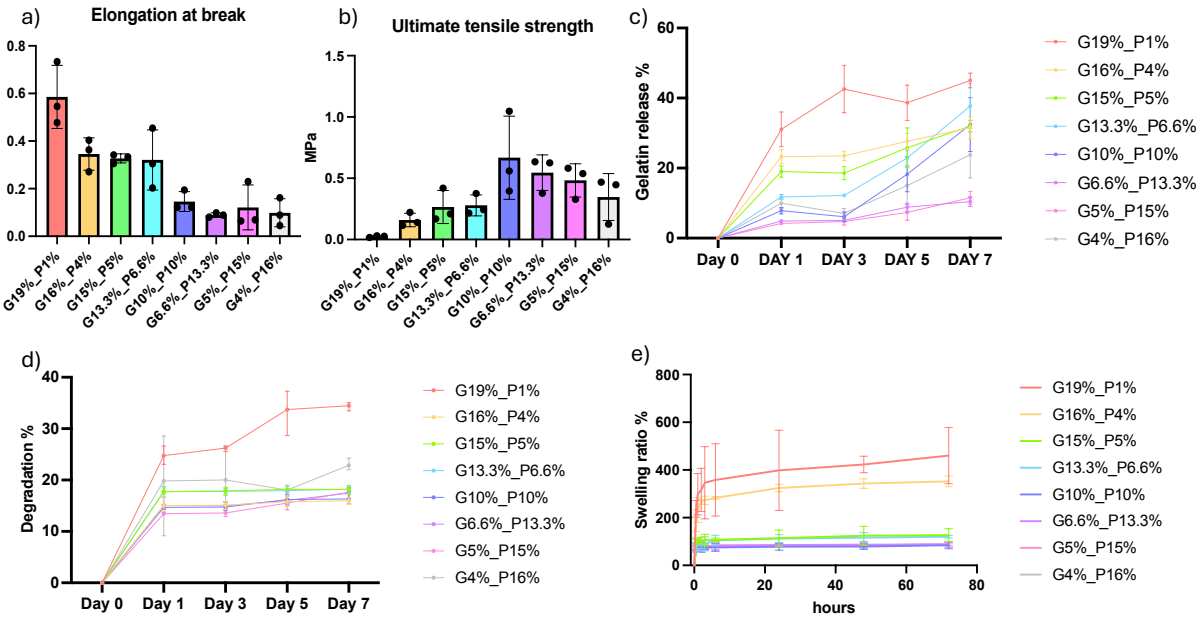

Figure 34 Mechanical and Swelling Properties of Gelatin/PEGDA Hydrogels at Varying Compositional Ratios.

In gelatin release, the result shows all formulations experience an increase in release over time, with a rapid initial phase that slows after Day 3. The G19%_P1% sample, represented by the red line, exhibits the highest release rate, reaching nearly 50% by Day 7, suggesting that higher gelatin content promotes faster release. In contrast, the G4%_P16% sample, shown in gray, maintains the lowest release profile, staying below 20% across the study period, indicating that higher PEGDA percentages slow the release rate. Other formulations display intermediate release patterns, generally slowing as PEGDA content rises, likely due to increased crosslink density that restricts gelatin diffusion. There is a similar trend in degradation and swelling ratio. The higher ratio of gelatin, the degradation and swelling ratio is higher.

Three groups of gelatin/PEGDA matrix were chosen for the microscope and SEM (Fig 35). G10%_P10% represents the high mechanical property; G15%_P5% represents the high ratio of gelatin; G5%_P15% represents the high ratio of PEGDA. Combining the microscopy and SEM results, it can be seen that the group with a high gelatin percentage presents a larger and more porous structure, and conversely, the group with a high PEGDA percentage presents a tightly packed pore structure. This was also responded in the subsequent cell implantation.

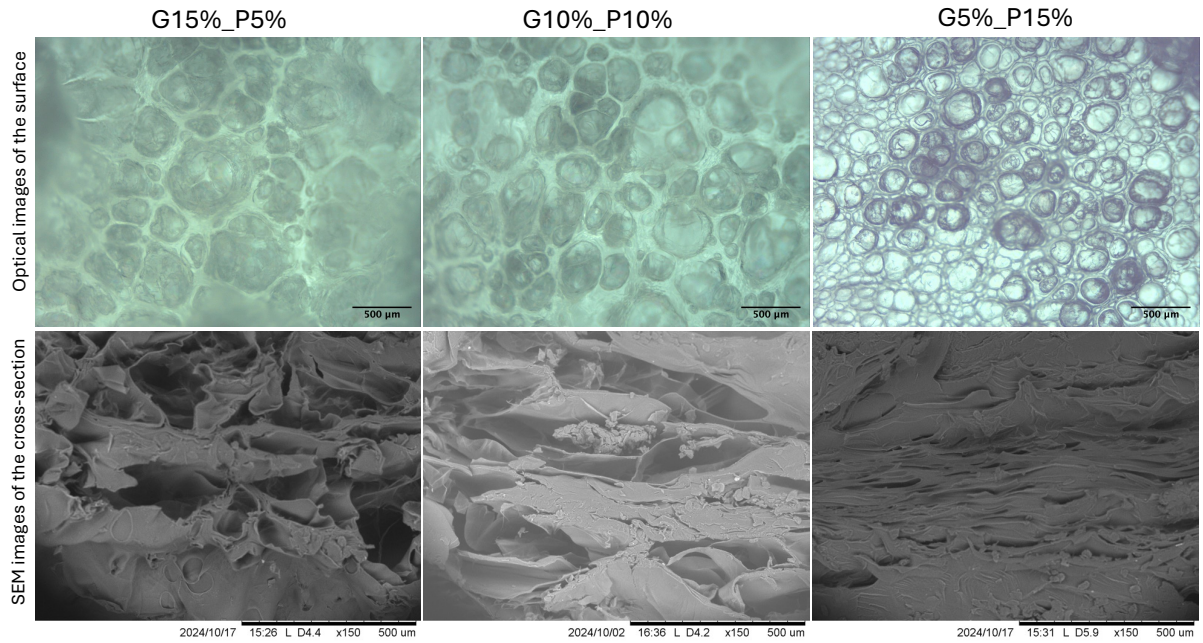

Figure 35 Three representative gelatin/PEGDA groups were selected for further research. The optical and SEM images show their different porosity.

6.3.2 Biological test

Due to the low mechanical strength of the G19%_P1% group, fully-degradation after 14 days, it was excluded from the next biological test. For the rest of the group, three groups was selected: G15%_P5% as the representative of the group with high concentration of the gelatin; G10%_P10 as the representative of the ratio of gelatin and PEGDA is 1:1 and also the highest mechanical properties; G5%_P15% as the representative of the high concentration of the PEGDA. The figure 36, 37 and 38 provided illustrates the condition of human umbilical vein endothelial cells (HUVECs) following a 3, 5, and 7 day culture period on hydrogel scaffolds with varying concentrations of gelatin (G) and poly(ethylene glycol) diacrylate (PEGDA). Analysis of the images was conducted to assess cellular viability, density, and morphology. Brightfield microscopy images show the scaffold structure, providing context for the distribution and morphology of the cultured cells. Fluorescein diacetate (FDA) staining indicates live cells with green fluorescence, while propidium iodide (PI) staining marks dead cells with red fluorescence. The merged images allow for a simultaneous visualisation of live and dead cells in relation to the hydrogel structure.

At day 3, the hydrogels with higher gelatin content (G15%_P5% and G10%_P10%) demonstrate a substantial number of live cells, as evidenced by the fluorescent green staining (Fig 36). The absence of significant propidium iodide (PI) staining in the provided images could be attributable to non-adherence of dead cells to the hydrogel matrices, leading to their subsequent removal during media changes or culture maintenance. In vitro, non-viable cells often lose membrane integrity and may detach from the substrate, which could result in an underestimation of cell death when analysing

adherent cell populations. This suggests that the hydrogel matrices support HUVEC adhesion and survival effectively in the initial stages of culture.

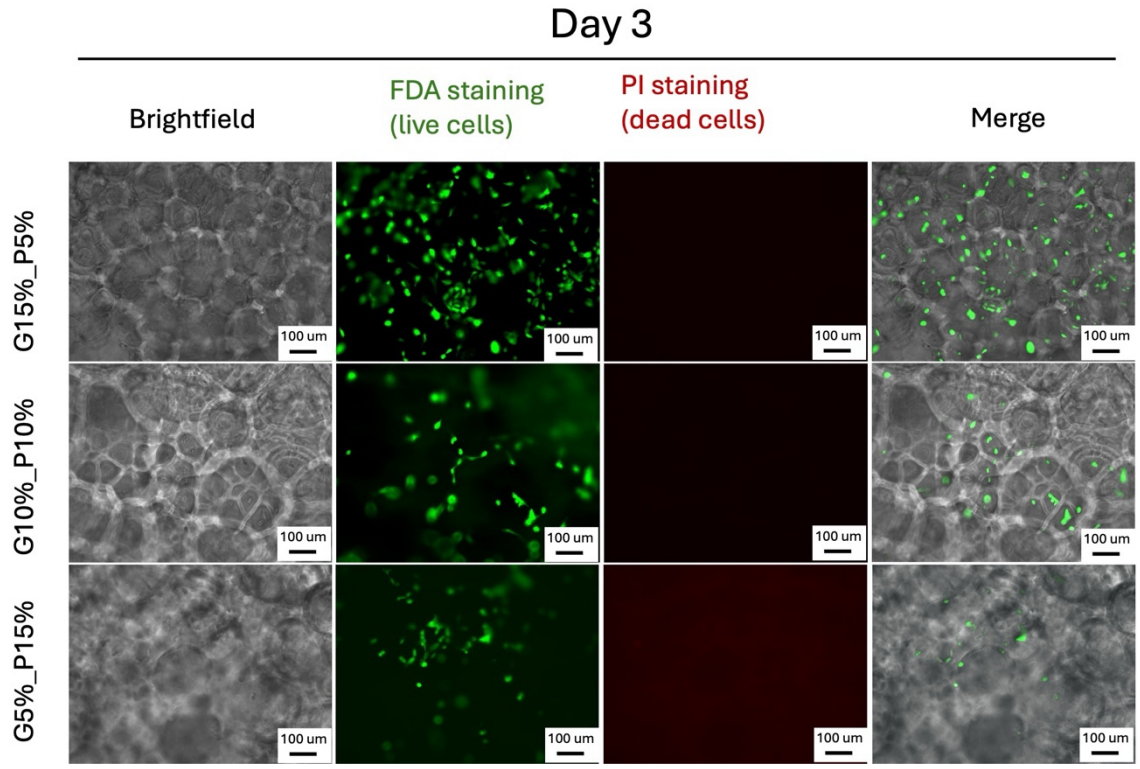

Figure 36 Day 3 HUVECs culturing on the three groups of gelatin/PEGDA matrix in brightfield, green channel, red channel and merge.

By day 5, the continuity of cell viability is observed, with a prevalence of live cells and low levels of cell mortality across all compositions (Fig 37). Notably, the density of live cells appears to be higher in the G15%_P5% and G10%_P10% samples compared to the G5%_P15% sample, possibly indicating improved cell proliferation. Upon review of the G15%_P5% group, an increase in cell number is apparent, suggesting successful proliferation. However, the morphology of the endothelial cells in this group exhibits some deformation, which could be indicative of a suboptimal interaction between the cells and the scaffold material at this particular concentration ratio. The deformation may influence cell function and could be attributed to mechanical stress or irregularities in the substrate. For the G10%_P10% and G5%_P15% groups, the cell density also appears to have increased, with a predominance of live cells as demonstrated by the green fluorescence. Minimal red fluorescence is observable, indicating a low incidence of cell death. The endothelial cells in these groups maintain a more regular morphology, which may reflect a more favourable microenvironment provided by these scaffold compositions for endothelial cell culture.

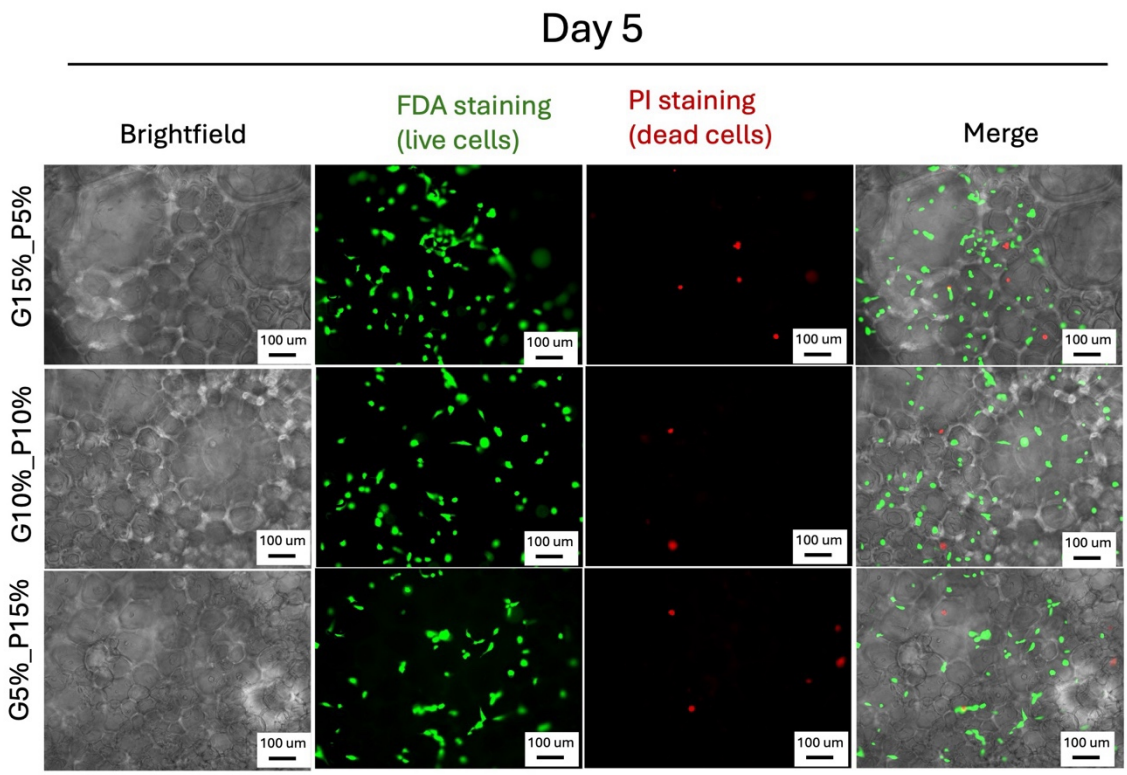

Figure 37 Day 5 HUVECs culturing on the three groups of gelatin/PEGDA matrix in brightfield, green channel, red channel and merge.

On day 7, Observation of the G15%_P5% % and G10%_P10% % groups reveal a proliferation of cells that appear to be extending and aligning with the underlying pore-like structure of the material, suggesting that the scaffold's architecture is conducive to cellular attachment and spreading (Fig 38). The morphology of these cells is indicative of healthy endothelial cell behaviour, typically characterised by elongation and formation of network-like structures, which are essential for the establishment of vascular-like tissues. In contrast, the G5%_P15% group exhibits a considerably lower cell density, which could be a consequence of several factors including suboptimal cell-material interactions, reduced mechanical stability, or less favourable biochemical cues for HUVEC adhesion and growth. The PI staining in this group is not prominently visible, which suggests that the lower cell number is not due to increased cell death but possibly due to inadequate cell proliferation or initial cell attachment. The merged images highlight the contrast between the thriving cell populations in the first two groups and the sparse cell presence in the last group. The extension of cells following the material's porous structure in the G15%_P5% and G10%_P10% scaffolds may also indicate the formation of cellular networks, which are vital for creating functional endothelial layers.

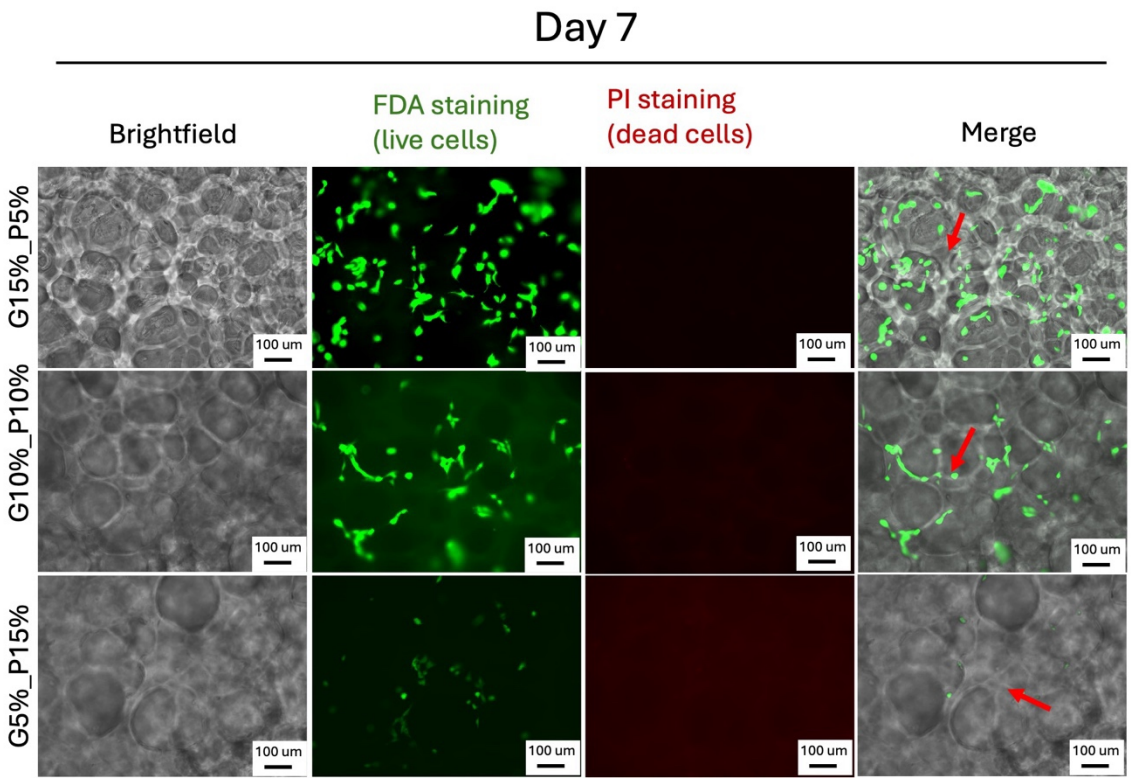

Figure 38 Day 7 HUVECs culturing on the three groups of gelatin/PEGDA matrix in brightfield, green channel, red channel and merge.

In summary, the results suggest that higher gelatin content promotes better adhesion, proliferation, and alignment, though an optimal balance is crucial to prevent adverse morphology changes due to mechanical stress. This balance is pivotal in designing scaffolds that support cell viability without compromising cell functionality. Unlike the control HUVECs described in Chapter 2, very few dead cells were detected in the gelatin/PEGDA cultures on day 3 or day 7. This likely reflects the scaffold's porous structure: nonviable cells fail to adhere and are removed during daily medium changes, while only a small fraction become trapped within the hydrogel's voids. Consequently, dead-cell counts alone do not accurately reflect the biocompatibility of the gelatin/PEGDA scaffold; instead, assessment should focus on the number and morphology of viable cells. The porous architecture observed in the G15%_P5% and G10%_P10% scaffolds supports cell spreading and network formation, a promising outcome for vascular graft applications where the establishment of endothelial cell networks is essential. The interconnected pores in the G15%_P5% group, in particular, could significantly enhance cell proliferation by facilitating the diffusion of nutrients and oxygen throughout the scaffold (Diao et al., 2019). For the following test, G10%_P10% was selected as the main material of its high tensile strength and its compatibility.

6.3.3 Fabrication of the vascular structure of gelatin/PEGDA with rotational dipping

Three different needle sizes were used to fabricate the tubular structure with diameters from 2mm to 0.7mm. The length of all the tubes depends on the needle length. After adjusting, the length of the tubes is 9-11 cm (Fig 39 a & b). All groups showed a uniform and consistent wall thickness, unaffected by different needle sizes—unlike the alginate tubular structure in Chapter 4, which was altered by freeze-drying and caused the gelatin/PEGDA walls appeared compressed and thinned length (Fig 39 c, d & e).

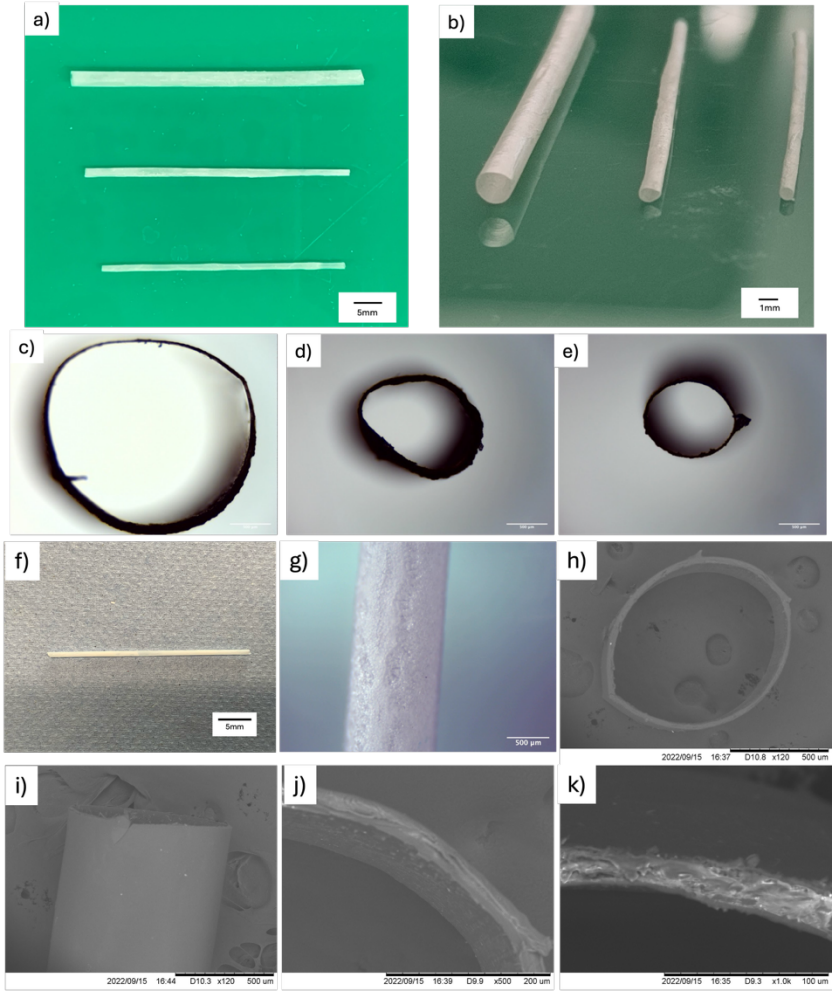

Figure 39 Fabrication of the vascular structure of gelatin/PEGDA with rotational dipping with top view a) and side view b). Cross-section of small vascular structure with a diameter of 2mm c), 1.5mm d), and 0.7mm e). The small vascular structure with a diameter of 0.7mm was chosen for the biological test f). It has a smooth surface g) and a fine edge h & i). The wall has a porous structure j &k).

The smallest size of the tubular structure (0.72mm) was selected as the main object to match the small vascular tissue. The SEM (Fig 39, h-k) shows the porosity of the cross-section of the tube wall, which could be beneficial for nutrition exchange in further biological research.

6.3.4 Seeding the HUVECs above the vascular structure

Multiple figs were spliced together to show a full view of HUVECs throughout the pipeline. Figures 40 and 41 consist of multiple smaller images to show the complete structure of the blood vessels, resulting in slightly different shades of light and dark. The cells are detailed in Figure 42. As mentioned previously, HUVECs were planted throughout the tubular structure as a way to observe the behaviour of HUVECs tubular structure. DAPI staining was used as an assay for the activity of HUVECs after 7 days of culturing in medium.

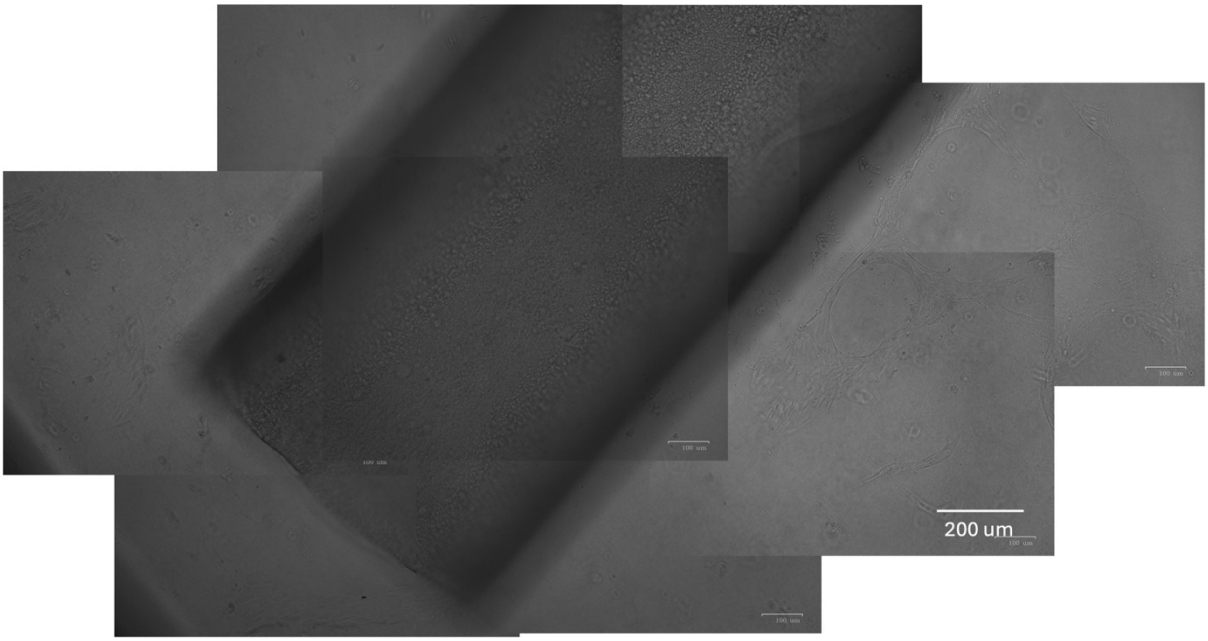

Figure 40 A full view of HUVECs attached gelatin/PEGDA small vascular tissue under brightfield. This figure is combined with multiple figures.

In DAPI staining, the fluence images show that HUVECs surrounded the small vascular structure. Five sites were selected to display the details. a) aligned the tube; b) near the tube; c) at the

end of the tube; d) near the corner of the tube; e) above the tube.

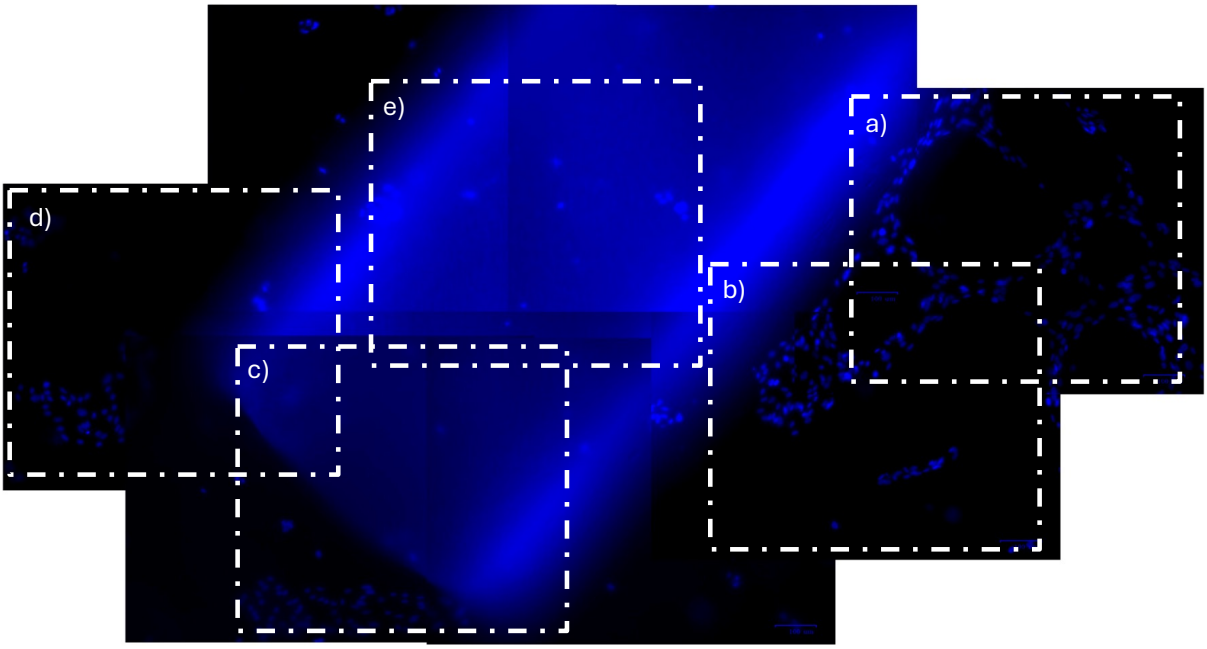

Figure 41 A full view of HUVECs attached gelatin/PEGDA small vascular tissue with DAPI staining. This figure is combined with multiple figures. The zoom-in details is in Fig 42.

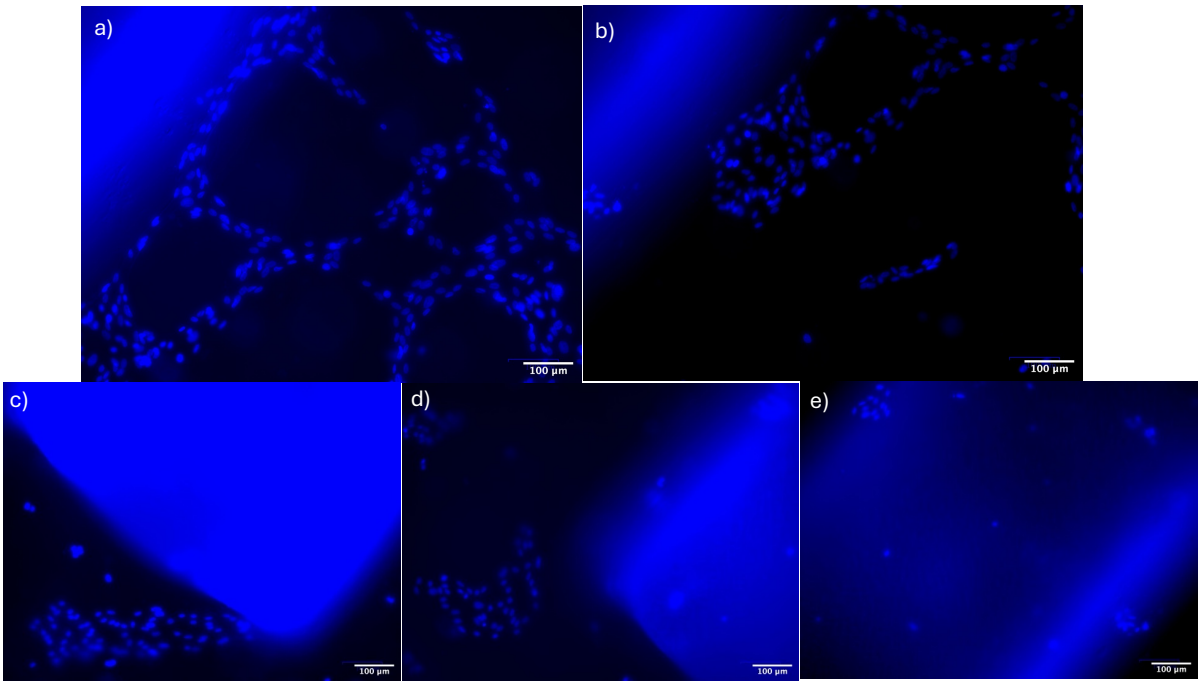

Figure 42 Detailed small vascular tissue with DAPI staining. a) aligned the tube; b) near the tube; c) at the end of the tube; d) near the corner of the tube; e) above the tube.

DAPI staining reveals that HUVECs have successfully formed a continuous endothelial cell network surrounding and also along the tube structure, extending partway into the tube itself (Fig 42). This suggests that with future integration of a perfusion system, it may be possible to connect small vascular tissues with 0.7 mm in diameter to the broader endothelial network within the construct. In

this study, direct seeding of HUVECs within the tube's interior has not yet been achieved. However, some endothelial cells have been observed proliferating along the tube's surface and extending bi-directionally, validating the compatibility of HUVEC attachment to the gelatin/PEGDA (polyethylene glycol diacrylate) material used in this scaffold.

Further research is needed to optimize HUVEC seeding within the tube's interior. Technical challenges include determining how to inject cells uniformly into the tube's lumen, understanding the effects of compressive forces on endothelial cell viability, and facilitating effective cell proliferation within a three-dimensional tubular structure. These issues are critical to advancing the use of gelatin/PEGDA materials in small vessel tissue engineering and may contribute significantly to developing functional, perfusable microvascular networks.

*6.4 Micro**vascular** structure printed with DNA hydrogel*

Moving from small vascular structures to microvascular structures and overcoming the smallest limitations, we developed a novel PRINting Cell Embedded Sacrificial Strategy (PRINCESS), designed to embed microvasculature directly within tissue constructs. Unlike the traditional sacrificial approach, where cells are added after hollow channels are formed, PRINCESS directly prints viable cells within a sacrificial biolubricant. As illustrated in Figure 43, endothelial cells encapsulated in a degradable biolubricant are printed first and then encased by tissue cells in a supporting gel. When the biolubricant degrades, it leaves a microvascular network of embedded endothelial cells within the tissue construct. This method requires careful control over the degradation process to protect cell viability and ensure structural integrity.

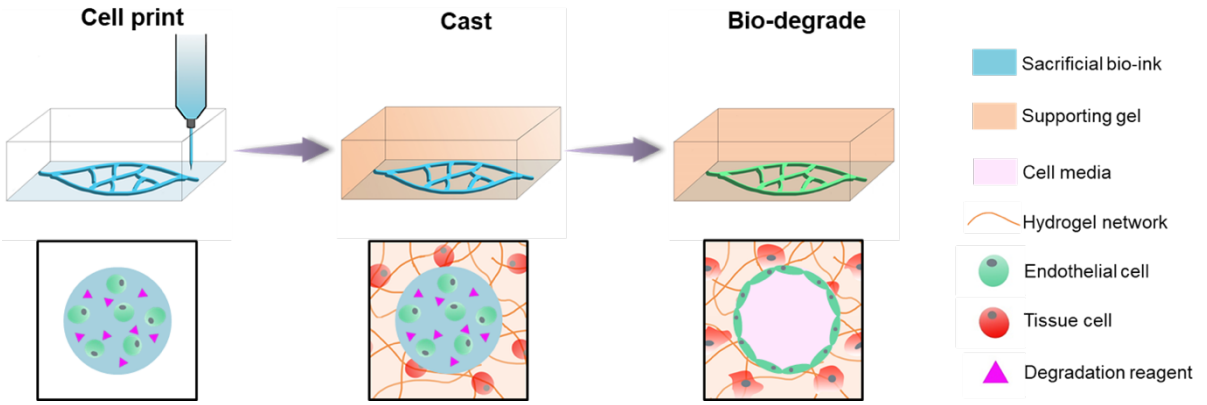

Figure 43 Illustration of PRINting Cell Embedded Sacrificial Strategy (PRINCESS). A sacrificial bio-ink which is embedded with endothelial cells and degradation reagents is bioprinted into the desired microvasculature structure at high resolution. A supportive hydrogel is then cast over the sacrificial structure, which itself can contain cells. Bio-degradation occurs within the sacrificial filaments under controlled conditions, leaving an appropriately endothelialised lumen.

6.4.1 Preparation of DNA hydrogel

Tsinghua University kindly offered the DNA hydrogel. DNA hydrogel is formed by mixing two construction units, as illustrated in Figure 44 a & b. One is Y-scaffold formed of three single DNA strands, and the other is a linear duplex linker. The "sticky ends" of the Y-scaffold and linker are complementary so it will lead to hydrogel formation very quickly when they are mixed. After mixing and gelation, the mechanical strength of DNA hydrogel was characterised using a shear rheometer. The live/dead staining shows that HUVECs keep a high cell viability in DNA hydrogel (Fig 44 c). Besides, Exo III was used for biodegradation of DNA hydrogel as a sacrificial material (Fig 44 d).

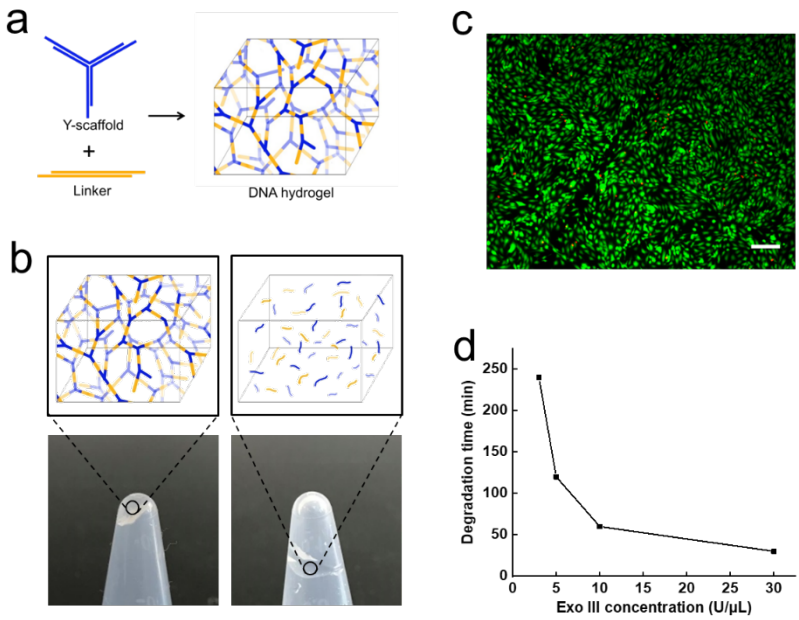

Figure 44 Gelation and degradation of DNA hydrogel. a. Gelation of DNA hydrogel by mixing two building blocks (Y-scaffold and Linker); b. Enzymatic degradation of DNA hydrogel by Exo III; c. Live/dead staining image of HUVECs in 24-well plate with 150U Exo III after 3d culture. Scale bar 200 μm; d. Degradation time of DNA hydrogel with different Exo III concentration.

6.4.2 Extrusion printing of DNA hydrogel

All the structures were printed using a custom-built, three-axis (X-Y-Z), bioextrusion-based 3D cell printer. Briefly, the printer runs by coordinating the motion of a mechanically driven syringe. Biolubricant was loaded in the syringe and printed on a stationary Z-platform, which moves downwards, allowing the structures to be printed layer-by-layer from the bottom up. Before printing, all equipment was sterilised by wiping it down with 70% ethanol, and sterility was maintained during the printing process by placing the bioprinter in a laminar flow cabinet.

Engineered tissue constructs were produced by printing sacrificial DNA hydrogel and cast with GelMA. Initially, 15 μL Exo III-laden Y-scaffold and 15 μL HUVECs-laden linker were loaded in a 100 μL glass syringe (Hamilton company) alternating every 5 μL and mixed thoroughly to form the

DNA hydrogel biolubricant. The glass capillary with varying diameters was attached to the glass syringe through a 1mm compression fitting (55750-01, Hamilton Company). Then, the syringe was loaded into the bioprinter, and the 3D structures were printed onto a coverslip. After printing, the HepaRG-laden GelMA supporting gel was deposited on the printed vascular structure and the entire structure was exposed to UV light (UV LED curing system, 365 nm, 60 s) for GelMA crosslinking.

6.4.3 results of microvascular structure

The printability of the DNA hydrogel was explored. Utilising the shear-thinning property of DNA hydrogels as a novel sacrificial, cell-laden biolubricant, we can print a 70-μm endothelialised microvasculature, breaking the limit of 100 μm. This is the smallest endothelialised microvasculature that has never been achieved so far. The mechanical strength of DNA hydrogel was first characterised using a shear rheometer. Figure 45 a shows that the shear-storage modulus G' is significantly higher than the shear-loss modulus G'' when the strain is below 10%, indicating that the hydrogel formation is verified as designed. When the strain increases, G' decreases and G'' increases dramatically, and G'' becomes higher than G' as the strain exceeds 31.6%, showing the hydrogel has great shear-thinning property and can be used for high-resolution printing. Due to this shear-thinning property, different structures of DNA hydrogel were printed using a custom-built extrusion-based 3D bioprinter. This bioprinter represents an adapted, extrusion-based version of a previously developed microvalve-based bioprinter used to bioprint human cells including human induced pluripotent stem cells. In order to print thin filaments, a glass capillary is connected to the printer and used as the nozzle. As shown in Figure 45 b, designed diameters (from 10 μm to 80 μm) can be obtained by pulling the glass tube using a P-1000 Micropipette puller (Sutter Instrument) and cutting the glass capillary at a certain position. Using the printer, vascular structures were printed in a six-well plate (Figure 45 c).

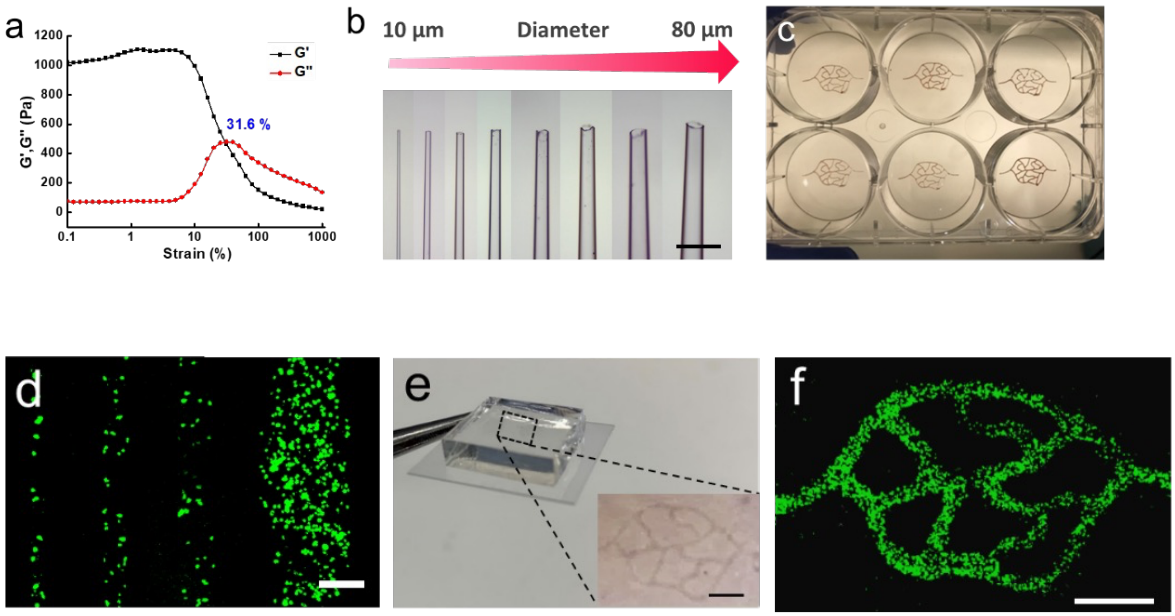

Figure 45 Printability of the DNA hydrogel. a) Rheological characterisation of 3.8 wt% DNA hydrogel in 1×PBS buffer with different strains; b) Glass capillaries with different diameters (10, 20, 30, 40, 50, 60, 70, 80 µm); c) Printed vascular structure in six-well; d) Confocal epifluorescence images of HUVECs with different diameters (50, 100, 200, 400 µm). Scale bar 200 µm; e) Pictures of printed tissue construct. Zoom-in picture is printed branched vascular structure using 3.8 wt% DNA hydrogel (with 2×10^7cells/mL HUVECs) cast by 15 wt% GelMA. Scale bar 1 mm; f) Confocal epifluorescence images of HUVECs within the branched vascular structure. Scale bar 1 mm.

To visualise the fate of the HUVECs in the sacrificial ink after bioprinting, CellTracker™ Green CMFDA Dye was used to stain HUVECs before printing. Then, printed DNA hydrogel with 2×10^7/mL embedded HUVECs was printed into the microvascular structure and cast with 15% GelMA. Figure 3d shows the HUVECs filaments printed had controllable diameters, from 50 µm to 400 µm (Fig 45 d). It is notable that the cells were lined in a near single-cell manner in the 50 µm filament. Branched vascular structures are also printed using HUVECs (Figure 45e, f), and the confocal epifluorescence images (Figure 45f) show that the cells aligned along the printed structure homogeneously. These results indicate our strategy is readily applicable to bioprinting.

Finally, to form an endothelialised microvasculature, Exo III and HUVECs were simultaneously embedded in the DNA hydrogel before printing. Exo III was mixed with linear duplex linker; HUVECs was mixed with Y scaffold. Then these two components were mixed as embedded DNA hydrogel for printing microvasculature. After casting with GelMA, the construct was incubated overnight for DNA degradation and cell adhesion to the supporting gel. During this incubation, the DNA hydrogel was slowly degraded by Exo III and the embedded HUVECs settled to the bottom of the construct. The structure was then turned upside down and placed in the incubator again for 24 hours to ensure that cells adhered to both the top and the bottom of the microvascular channel. Finally, non-adherent cells, DNA fragments, and Exo III were removed by aspirating the sacrificial structure (Figure 46 a). As shown in Figure 46 b-c, the number of HUVECs decreases slightly after removing the non-

adherent cells, indicating that most cells had already attached to the channel. Figure 46 d shows the 3D fluorescent images of HUVECs in the microvascular channel. As can be observed, HUVECs adhered to the channel walls nearly confluently and formed a hollow lumen structure, which confirms the endothelialisation of the microvasculature. Moreover, a 70 µm microvasculature with numerous HUVECs attached has been fabricated using this strategy (Figure 46 e). Endothelialised microvasculature with such high resolution (< 100µm) has rarely been reported in previous research

To fabricate a cell-laden tissue construct with branched microvasculature, the derived cell line HepaRG was encapsulated in GelMA. CellTracker™ Red CMTPX Dye was used to stain HepaRG for visualisation. After bio-degradation, cell adhesion and removal of non-adherent cells, a microvascularised liver tissue construct is formed and characterised by confocal epifluorescence microscopy using an image-mosaic technique (Figure 46 f). Fabrication of microvascularised tissue construct provides a platform for pharmacological and toxicology testing, as well as proof of concept for fabricating complicated vascularised organs with multiple cell types.

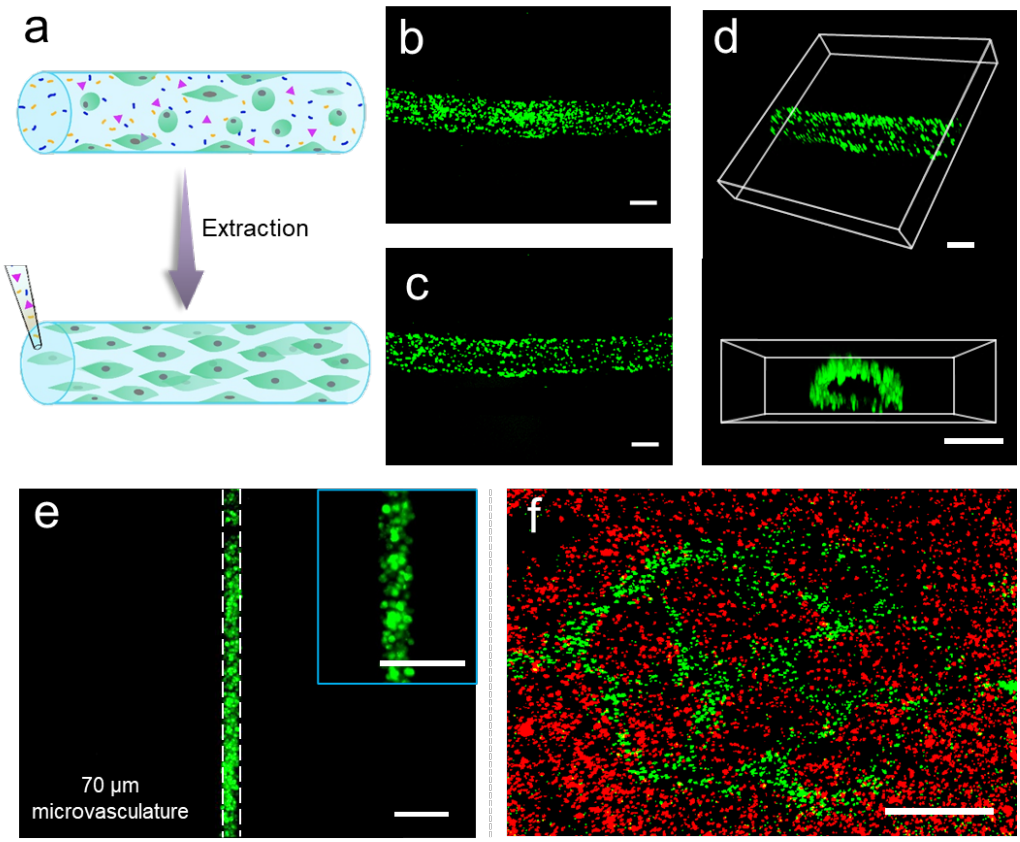

Figure 46 Preparation of branched microvasculature. a) Scheme of extraction process; b and c) Fluorescent images of HUVECs before (b) and after (c) removing non-adherent cells. Scale bar 200 µm; d) 3D confocal epifluorescence images of HUVECs cells lining the microchannel walls. Scale bar 200 µm; e) Fluorescent image of HUVECs in 70 µm microvasculature. Inserted picture is a zoom-in image of microvasculature. Scale bar 200 µm; f) Confocal epifluorescence images of liver tissue construct with branched microvasculature. Red: CellTracker Red CMTPX dye labelled HepaRG cells. Green: CellTracker Green CMFDA dye labelled HUVEC cells. Scale bar 1 mm.

6.5 Discussion

In tissue engineering, the fabrication of microvascular tissue generally refers to the concept of a tubular structure made of biomaterial. One primary purpose of this fabrication is to mimic human blood vessels. This study explored diverse printing techniques and materials to construct structures ranging from small-diameter blood vessels to complex microvascular networks. Through careful adaptation of each printing method to meet specific material and design requirements, the successful fabrication of small blood vessels, with diameters varying from 2 mm to 0.07 mm, was achieved. Notably, these fabricated vessels were integrated into microvascular networks, establishing vital interconnections to optimise vascular functionality.

A significant strength of this study is the effective combination of printing technologies and crosslinking techniques for materials. Although 3D bioprinting has stringent limitations on material selection due to its specific criteria, using a more adaptable printing technology expands the range of suitable materials. This chapter builds on the insights from Chapters 4 and 5 by integrating the rotational dipping printing method confirmed in Chapter 4 with dual freeze-drying crosslinked gelatin/PEGDA systems in Chapter 5. In practice, creating small vascular structures necessitates careful manipulation by the operator. Notably, the freeze-dried and crosslinked small tubular structures developed here can be easily managed—picked up, moved, cut, and stored—without rehydration. This practical attribute significantly alleviates operational challenges for researchers and increases the potential for industrial application of the technology. Furthermore, the capacity for long-term stable preservation is vital for advancing these methods from laboratory research to industrial-scale use.

7. Discussion and future work

7.1 Research review and discussion

This research aimed to fabricate small vascular tissue by developing an innovative method to enhance the mechanical strength of biomaterials while maintaining the integrity of pure gelatin. To achieve this, a straightforward and rapid rotational dipping printing technique was employed, enabling the successful fabrication of small vasculature tissues with diameters ranging from 0.7 mm to 2 mm. Additionally, a collaborative activities focused on creating microvascular channels as narrow as 0.07 mm by employing a smart DNA hydrogel as a sacrificial material in conjunction with extrusion-based 3D printing.

The rotational dipping method is a promising approach in the field of tissue-engineered small-diameter blood vessels (SDBVs), offering fast and precise small tubular construction that closely mimics the natural structure of blood vessels. By adjusting the rotational speed, this method enables the alignment of alginate or gelatin with other biomaterials within the hydrogel matrix. This circumferential alignment can significantly enhance the mechanical properties, replicating the natural alignment of smooth muscle cells and the structural integrity required for blood vessels. This rotational speed decrease the effect of gravity applying on materials, thus improving reliability and clinical translation potential. Setting up simple and easy equipment saves both time and money. Besides, this research proves that at least two biomaterials (alginate and gelatin) can be applied in this rotational dipping, which can expand material choices and remove barriers for smaller research labs. The rotational dipping method holds considerable potential for creating vascular grafts with complex, biomimetic properties, crucial for treating cardiovascular diseases. By incorporating advancements in bioinks and automation, this method could produce highly customizable vasucalr structure that align well with patient-specific requirements, supporting both research applications and clinical translation.

This research's innovative dual-freezing crosslinking approach for gelatin and PEGDA addresses a critical gap in the field. Previous studies have typically classified gelatin-PEGDA crosslinking as physical due to the material's tendency to lose mechanical integrity upon reaching water equilibrium—a fundamental drawback for biomaterial applications. Researchers have largely concentrated on enhancing gelatin's strength through various chemical crosslinking methods and modifications, yet these approaches compromise gelatin's inherent bioactivity, which is particularly beneficial for cell biology applications.

The dual-freezing crosslinking method described here enables the use of pure, unmodified gelatin, overcoming its traditional strength limitations without sacrificing its biocompatibility. This

approach preserves gelatin's advantages for cellular interaction and biocompatibility and opens up opportunities for its broader application in tissue engineering, where mechanically robust yet bioactive scaffolds are essential. This breakthrough suggests that pure gelatin, once it overcomes its weak mechanical properties, can now be considered a viable and versatile material for cell-based applications across biomedical fields. The dual freeze-drying crosslinking method, an innovative form of free radical polymerisation without a solvent, presents significant potential in tissue engineering. This approach resembles a compelling fusion of raw hydrogels with polymeric materials, bypassing the limitations imposed by organic solvents. As water is a critical component in hydrogels that supports cell compatibility, it underlies the extensive use of hydrogels in tissue engineering. Traditional polymerisation methods often require organic solvents, which are unsuitable for cell culture environments; consequently, many polymers with promising mechanical or functional properties are generally excluded from biomaterials due to biocompatibility concerns.

This study effectively demonstrates the application of various 3D bioprinting techniques for engineering small-diameter blood vessels, addressing the unique fabrication challenges associated with decreasing vessel size. As structural size diminishes in tissue engineering, technical constraints become more pronounced, especially when balancing biocompatibility with mechanical strength. 3D bioprinting has emerged as a viable solution to these challenges, yet past studies have struggled to produce artificial vessels around 1 mm in diameter that also meet the necessary mechanical requirements. Although electrospinning has recently enabled the fabrication of vessels with diameters as small as 1 mm and sufficient mechanical strength, the resulting constructs consist of extremely fine filaments that deviate from the matrix composition found in natural tissues.

The innovative cross-linking method presents a significant advancement by reinforcing the mechanical strength of natural hydrogels, which are traditionally too soft for small vessel tissue engineering. This approach allows the creation of small vessel structures using a simpler rotational dipping method, achieving structural properties comparable to electrospun vessels but with enhanced biocompatibility. Notably, this study successfully constructs small vessel tissues seeded with HUVECs at diameters ranging from 0.07 mm to 0.7 mm. This range not only demonstrates the flexibility of the method but also provides a foundational step towards developing an integrated small vessel network, which is crucial for the advancement of functional tissue engineering and vascular graft applications.

Table 6 Overview of the project

Main Result of This Research	Contribution	Future Work
Chapter 4: Rotational Dipping Printing	Confirms and expands upon prior research by addressing the influence of rotational speed on structural formation.	Develop automated design systems to explore additional biomaterials and enhance the fabrication of multilayered small vascular tissues.
Chapter 5: A Novel Dual Freeze-Drying Crosslinking Method	Achieves crosslinking of pure gelatin with PEGDA for the first time, resulting in a biomaterial with enhanced mechanical properties.	Conduct further research on underlying mechanisms and explore alternative free radical polymerization techniques.
Chapter 6: Fabrication of Small Vascular Tissue Structures (0.07-2mm) through Diverse 3D Bioprinting Techniques	Demonstrates a breakthrough in producing microvascular structures as small as 0.07mm, facilitating connections between small (2mm) and microvascular structures.	Investigate the potential for perfusion from small vessels (2mm) to microvascular networks and evaluate in vivo grafting feasibility for gelatin/PEGDA small vascular structures.

7.2 Future work

While my current investigation has elucidated the static tensile properties and endothelial cell–scaffold interactions of gelatin-based small-diameter vascular constructs, translating these promising materials into clinical applications will require a broader suite of evaluations. In upcoming studies, we will extend our mechanical characterisation into the dynamic viscoelastic behaviour and probe the rheological performance of gelatin/PEGDA scaffold to optimise print fidelity. We will also examine the interfacial properties of luminal coatings under arterial shear to ensure hemocompatibility and validate the surgical robustness of graft walls through standardised suture retention testing. Besides, the concept of freeze-drying with free radical polymerisation can be applied into other polymers.

Dynamic mechanical analysis (DMA) was conducted in accordance with ISO 6721-10:2021 (“Plastics – Dynamic mechanical properties – Part 10: Shear rheology”). Rectangular specimens (10 mm × 5 mm × wall thickness) were sectioned from the tubular grafts and mounted between the tension clamps. After equilibrating the test chamber at 37 °C, a sinusoidal strain of 0.1 % amplitude was applied over a frequency sweep from 0.1 to 10 Hz. Storage modulus (E'), loss modulus (E''), and loss factor ($\tan\delta = E''/E'$) were recorded continuously as functions of frequency. Emphasis was placed on E' values at 1–2 Hz—corresponding to the human blood pressure range—and these were benchmarked against native arterial E' ($\approx$ 0.5–1.5 MPa). Tan δ values were confirmed to lie within 0.05–0.15, indicating sufficient viscous damping. This viscoelastic profiling is essential for small-diameter vascular structures to ensure adequate buffering of physiological pulsatile loads, closely matching arterial

compliance, and minimising pulse-wave reflections and shear stresses that can compromise long-term graft patency.

Oscillatory shear rheometry was performed in accordance with ASTM D2196-19 (Standard Test Methods for Rheological Properties of Non-Newtonian Materials by Rotational Viscometer) to evaluate shear-thinning behaviour and structural recovery of the hydrogel bioinks. After hydrogels or cell-laden bioinks were loaded onto a 25 mm, 1° cone-and-plate geometry at 25 °C, a flow sweep from 0.01 to 100 s^{-1} was applied to characterise the apparent viscosity (η_{app}) as a function of shear rate ($\dot{\gamma}$). Thereafter, a thixotropy loop was conducted by imposing high shear (100 s^{-1}) for 60 s followed by low shear (0.1 s^{-1}) for 300 s to assess recovery of the material's viscoelastic network. Apparent viscosity versus shear rate and oscillatory moduli (storage, G′, and loss, G″) before shear, during high-shear, and after recovery were continuously recorded. Power-law fitting ($\eta_{app} = K \cdot \dot{\gamma}^{n}$) was used to extract the flow-index n (target < 0.7) and consistency K, and modulus recovery was quantified, with ⩾ 90 % recovery within 60 s set as the acceptance criterion. Such rheological profiling is critical for small-diameter vascular constructs to ensure that bioinks flow easily through narrow nozzles without damaging encapsulated cells, yet rapidly rebuild solid structure upon deposition, thereby maintaining lumen integrity and enabling high-resolution fabrication of small vessels.

Suture retention testing was conducted in accordance with ISO 7198:2016 ("Cardiovascular implants – Tubular vascular prostheses") to evaluate the resistance of the graft wall to suture pull-out. Tubular graft segments (~20 mm length) were mounted horizontally in custom grips on an Instron 5943 tensile tester fitted with a 10 N load cell. A single 7-0 polypropylene monofilament suture loop was passed through the graft wall 1 mm from the cut edge, and the loop ends were secured to the upper grip. At room temperature, a crosshead speed of 12 mm/min was applied until the suture tore through the wall. Peak force at failure (N) was recorded automatically for each of five specimens per formulation. Mean suture retention strength was then compared against a clinical benchmark of 2.0 N; grafts with an average pull-out force ⩾ 2.0 N were considered to provide sufficient tear resistance for reliable small-vessel anastomosis. This assessment is critical for small-diameter vascular constructs to ensure that surgical handling does not compromise graft integrity during implantation.

Besides, in this thesis, in the process of analysis of the biological images, the standard 8-bit RGB merges in Fiji/ImageJ compress the original 12/16-bit channels, which leads to an apparent reduction in fluorescence. To overcome this, future experiments will utilise hyperstack composites to maintain full bit-depth or implement automated macros to fix Brightness/Contrast windows across all channels prior to overlay and explore commercial and open-source platforms (e.g. Imaris, CellProfiler) that preserve quantitative dynamic range through to final images export (Dunn et al., 2011; Schindelin et al., 2012).

By enabling free radical polymerisation in the absence of solvents, this method opens up the possibility of integrating a wider variety of macromolecules into hydrogels. One GelMA was tested in Chapter 5 as a comparison group of gelatin/PEGDA. Modified with the methacrylate group, GelMA can polymerise under similar conditions to PEGDA. Therefore, GelMA is a suitable component with PEGDA as reported (Mamaghani et al., 2018). Some pre-tests were conducted in Chapter Appendices, but more systematic studies need to be carried out, such as whether there is a competition between the UV-initiated free radicals of GelMA and PEGDA, their reaction rates, etc., in the same system. Compared with gelatin, GelMA can provide more cross-linking network, and GelMA/PEGDA scaffold may have higher mechanical strength than gelatin/PEGDA after freeze-drying cross-linking. This not only broadens the selection of biomaterials but also enhances the applicability of hydrogels across a wider range of biomedical contexts, from tissue scaffolding to drug delivery. In summary, the dual freeze-drying crosslinking technique holds the promise of making more macromolecules viable for biomaterial applications, potentially revolutionising the development of robust, biofriendly hydrogels for diverse applications in regenerative medicine and beyond.

8. Appendices

8.1 Fibroblast cell in gelatin/PEGDA matrix

In this investigation, the attachment and morphological characteristics of fibroblast cells expressing red fluorescent protein (RFP) were explored when cultured on hydrogel scaffolds with variable gelatin (G) and poly(ethylene glycol) diacrylate (PEGDA) ratios. The utilization of RFP-expressing cells enables non-invasive live-cell imaging, providing insights into cell viability and morphology without the requirement for additional staining procedures that could compromise cell integrity. Fibroblasts play a crucial role in vessel repair and regeneration by contributing to the extracellular matrix and supporting the function of endothelial cells. The expression of RFP in these fibroblasts allows for real-time, non-destructive monitoring of cell behaviour and interaction with the scaffold materials. All red-channel fluorescence in the HDF study derives from constitutive expression of RFP within the cytosol of the fibroblasts. No additional nuclear or cytoskeletal stains were applied. Because RFP expression levels and microscope illumination can vary across the field of view, all live-cell images were processed prior to any quantitative measurements. This investigation, focused on the first day of culture, provides critical insights into the early-stage cell-scaffold dynamics essential for designing materials for vascular tissue engineering. The findings will inform the optimisation of scaffold composition to promote vascularisation and tissue integration in long-term vessel research. Because these cells proliferate rapidly and generate highly non-uniform fluorescence by Day 6, flat-field correction and background normalisation were not applied; consequently, data are presented qualitatively (representative fluorescence micrographs only). This pre-test guided the optimisation of scaffold formulations.

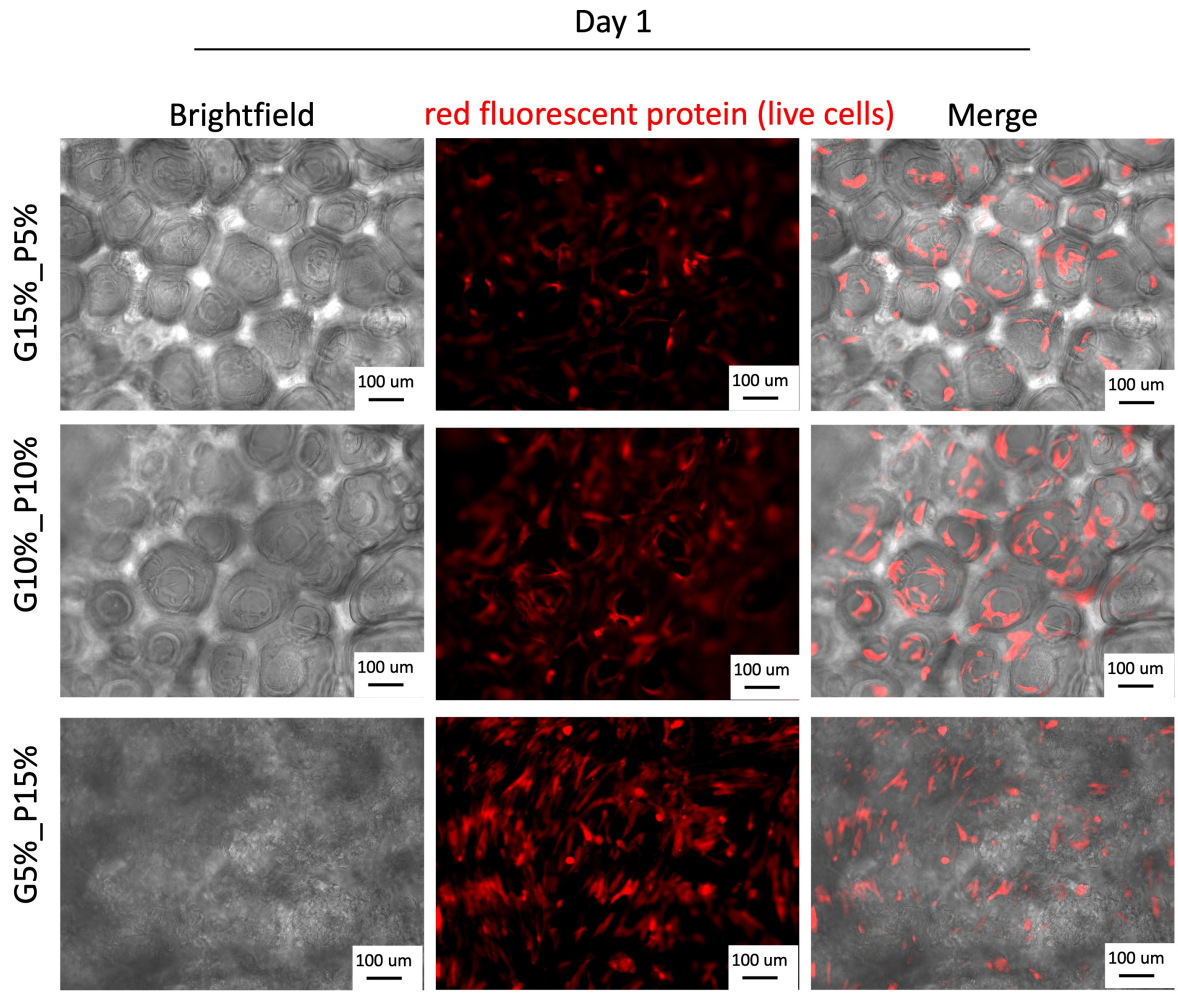

Figure 47 HDF seeded in gelatin/PEGDA in Day 1

In the first day after seeding, upon examination of the G15%_P5% scaffold, cells exhibit a propensity for attachment and exhibit elongated morphologies, suggesting effective initial interactions with the scaffold. The cells appear to be aligning with the scaffold's structure, which may be indicative of favourable cell-material communication and initial stages of matrix deposition. Similarly, The G10%_P10% scaffold shows results with robust cell attachment and a prominent display of elongated cells. This elongation is characteristic of healthy epithelial cells that are engaging with the substrate, potentially forming early contact points for subsequent proliferation. In contrast, the G5%_P15% scaffold, while showing successful cell attachment, exhibits a more disorganized cell distribution and morphology. The cells do not display the same degree of elongation as seen in the higher gelatin content scaffolds, which may suggest less optimal cell-scaffold interactions. The initial attachment of fibroblast cells expressing RFP to the hydrogel scaffolds is successful across all tested groups. However, the degree of cell elongation and alignment with the scaffold structure differs, with higher gelatin content scaffolds (G15%_P5% and G10%_P10%) showing more favourable conditions for cell attachment.

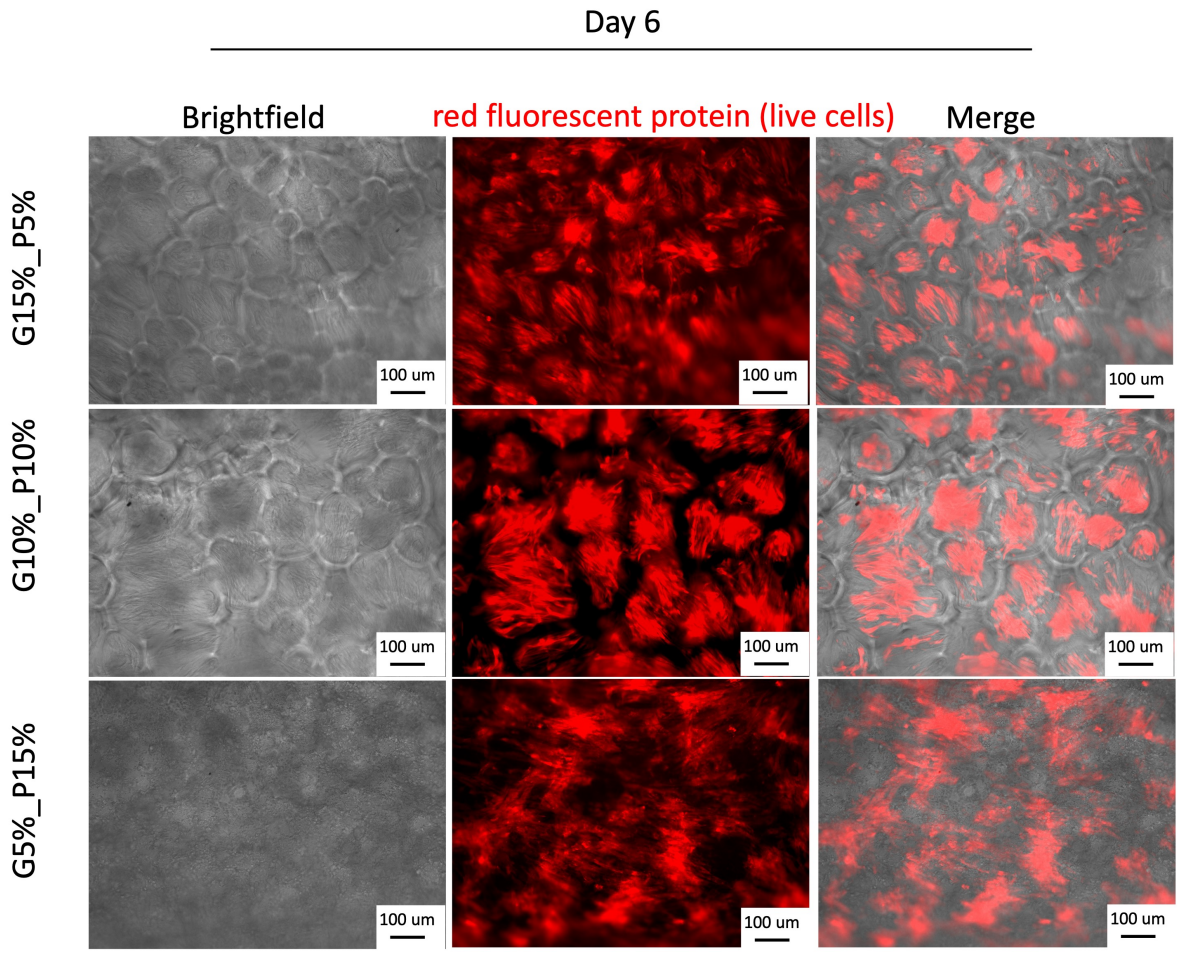

Figure 48 HDF seeded in gelatin/PEGDA in day 6

At 6 days, the G15%_P5% and G10%_P10% groups show a marked increase in cell density, indicating robust proliferation. The fibroblasts in these groups have expanded to occupy the interstitial spaces of the scaffold's pore-like structure, suggesting not only favourable conditions for cell growth but also the cells' active role in matrix remodelling and space-filling behaviour. The confluent monolayer of fibroblasts, as seen in the merge images, reveals a homogeneous distribution and substantial coverage of the scaffold surface. This is indicative of an environment that supports cellular adhesion, spreading, and the establishment of a fibroblast network, which are essential for effective tissue integration and scaffold vascularisation. In contrast, the G5%_P15% group exhibits a less dense cell population, with cells failing to completely fill the scaffold's pores. This may reflect a less optimal scaffold composition for supporting fibroblast proliferation and coverage, potentially due to mechanical properties or biochemical cues that are less conducive to cell adhesion and growth.

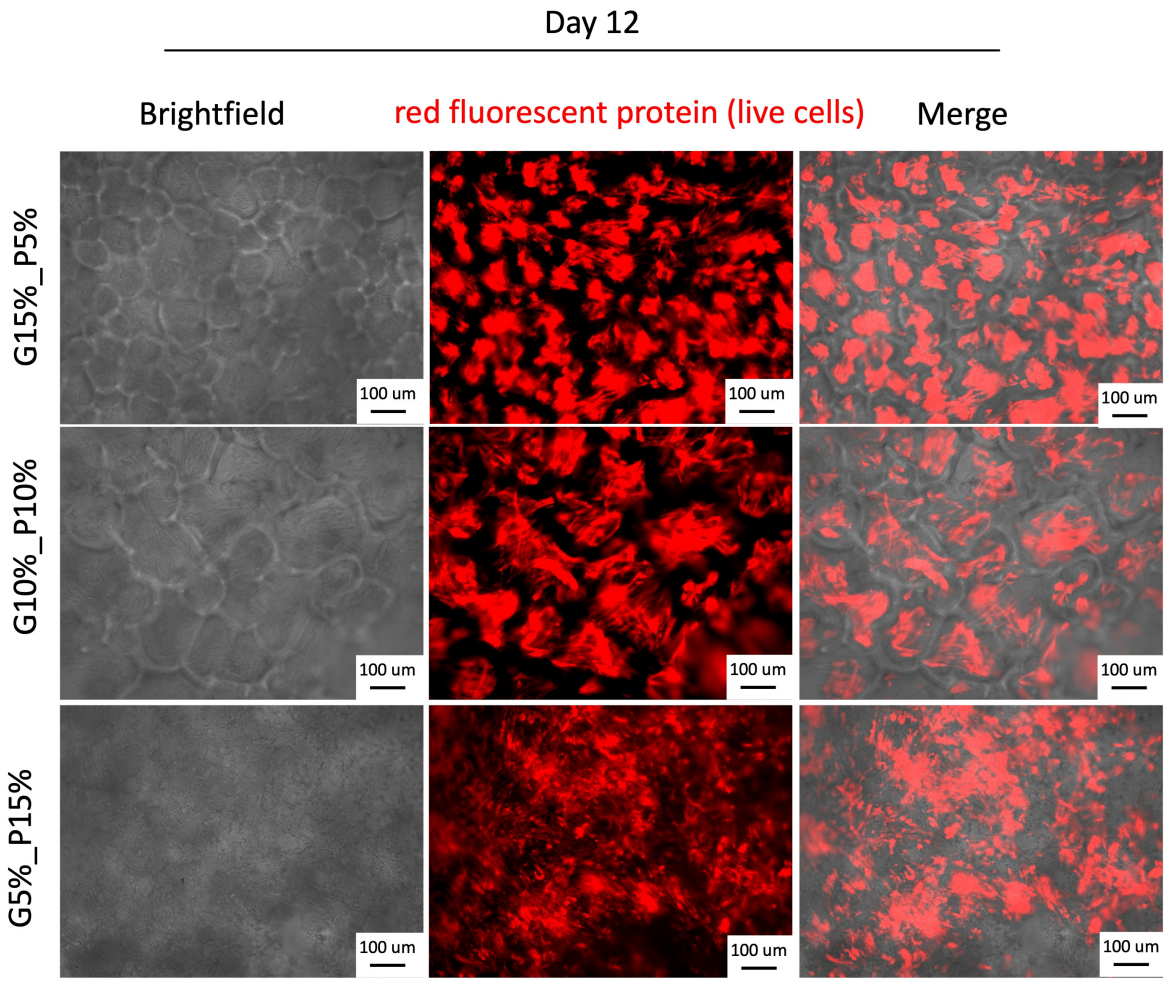

Figure 49 HDF seeded in gelatin/PEGDA scaffold in day 12

In the 12 day, in the G15%_P5% group, fibroblasts have proliferated extensively, creating dense cellular networks that envelop the material's structure. The G10%_P10% sample also demonstrates significant cell proliferation, with fibroblasts adopting an elongated morphology and displaying a well-organised distribution. The consistency in cell shape and the formation of interconnected cellular structures suggest an optimal environment for fibroblast activity and potential tissue formation. Conversely, the G5%_P15% group reveals a markedly different scenario. The scaffold appears less populated, but the fibroblasts show a more heterogeneous morphology with less organisation. This could be due to the lower gelatin content, which might not provide the same level of support for cell adhesion and spreading as seen in the scaffolds with higher gelatin percentages.

In summary, after 12 days of culture, the hydrogel scaffolds with higher gelatin content (G15%_P5% and G10%_P10%) are more effective in supporting fibroblast proliferation, organisation, and scaffold coverage. In contrast, the scaffold with the highest PEGDA content (G5%_P15%) does not seem to support the fibroblast culture to the same extent, which may have implications for its

application in tissue engineering. These findings reinforce the importance of scaffold composition in regulating fibroblast behaviour and suggest that a higher gelatin content may be beneficial for applications requiring extensive cell growth and matrix formation.

8.2 Human osteosarcoma (HOS) cells in gelatin/PEGDA matrix

In an extension of our biomaterial research, we transitioned from fibroblast cultures to an evaluation of human osteosarcoma (HOS) cells to assess the material's suitability for supporting a different cell type. Osteosarcoma cells, given their unique characteristics and requirements, serve as a relevant model for bone-related tissue engineering. The experiment was conducted over a three-day period to observe early cell-material interactions, which are indicative of the scaffold's potential to support cell attachment, viability, and initial proliferation. This phase of the study provides crucial insights into the hydrogel's performance in a bone cancer cell context and contributes to a broader understanding of its applicability across various cell types. The following analysis details the initial findings of HOS cell behaviour when cultured on hydrogel scaffolds with variable gelatin (G) to poly(ethylene glycol) diacrylate (PEGDA) ratios.

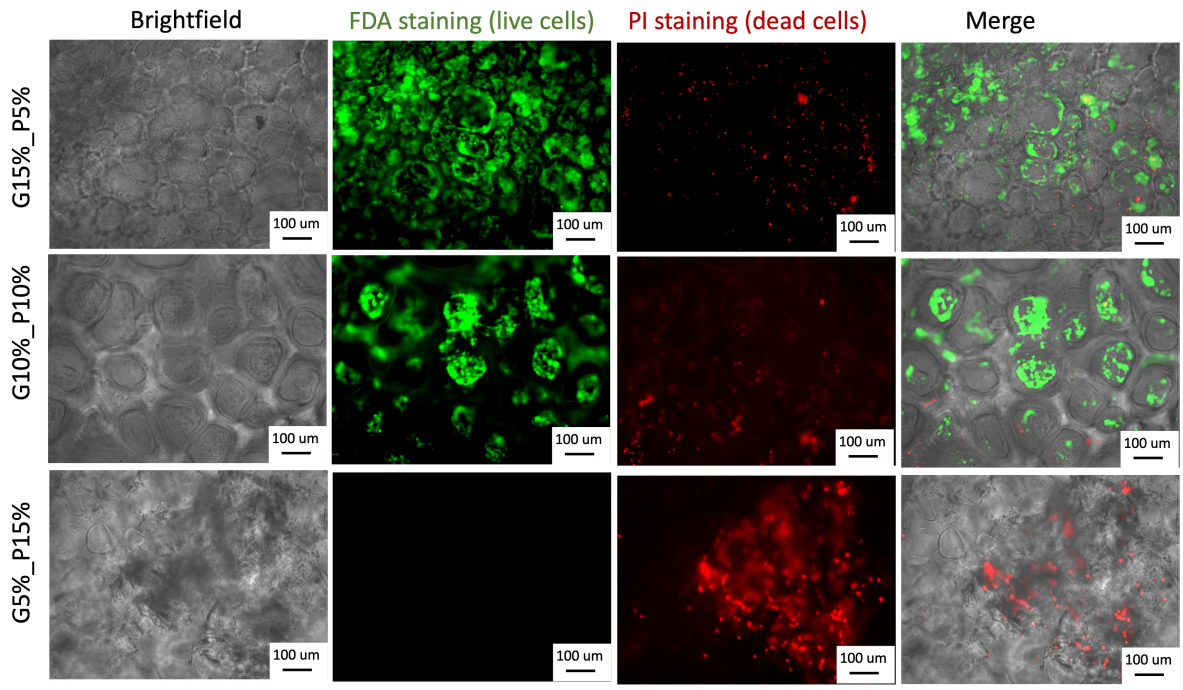

Figure 50 HOSs seeded in gelatin/PEGDA in day 3

The provided micrographs feature human osteosarcoma (HOS) cells cultured on hydrogel scaffolds of varying gelatin (G) to poly(ethylene glycol) diacrylate (PEGDA) compositions, after three days of incubation. The brightfield images allow for the examination of the scaffold morphology, the fluorescein diacetate (FDA) staining indicates viable cells in green, and the propidium iodide (PI)

staining identifies non-viable cells in red. The merged images offer a holistic view of cell viability and distribution in relation to the scaffold structure.

After 3 day culturing, in the G15%_P5% group, a high density of HOS cells can be observed with a predominance of green fluorescence, indicating a significant number of live cells. There are also discrete red fluorescent spots, suggesting some cell mortality, but the proportion of live cells appears to dominate, reflecting a conducive environment for cell growth and viability. The G10%_P10% scaffold displays a heterogeneous cell population with a mixture of live and dead cells. The FDA staining shows clusters of live cells, while the PI staining indicates a higher presence of dead cells compared to the G15%_P5% group. This could suggest that the environment provided by this composition is less optimal for HOS cell viability. The G5%_P15% group exhibits a substantial amount of red fluorescence, indicating a considerable number of dead cells, which dominate the visual field. The live cells, as evidenced by green staining, are sparsely distributed. This suggests that the hydrogel composition may not support the survival and proliferation of HOS cells as effectively as the other compositions.

In summary, the initial culture results indicate that the composition of the hydrogel scaffold significantly impacts the viability and morphology of HOS cells. The G15%_P5% composition demonstrates a favourable environment for HOS cell survival and proliferation after three days of culture. In contrast, the G10%_P10% and G5%_P15% compositions exhibit an increased number of dead cells, with the highest PEGDA content scaffold showing the least favourable conditions for HOS cell culture. These findings are critical for the design and optimisation of hydrogel scaffolds for applications involving osteosarcoma cell growth or bone tissue engineering. Further investigation is required to understand the mechanisms affecting cell viability and to optimise the hydrogel properties for enhanced cellular compatibility.

In addition to the effects of materials on cells, the above cell studies also revealed the interaction between cell cultures and the scaffold's material. can indeed impact the apparent pore-like structure of the material. As cells adhere to and proliferate within the scaffold, they can deposit extracellular matrix components, which may alter the scaffold's architecture. This cell-scaffold interaction can lead to several observations:

1. Pore occlusion: As cells proliferate, they can fill the pores and reduce the visible porosity of the material, making the scaffold appear less porous than it initially was. Shown in fibroblast day 6 and day 12.

2. Matrix remodeling: Cells can remodel the scaffold by secreting matrix metalloproteinases that degrade the scaffold material, potentially enlarging the pores or changing their shape.

3. Selective adherence: Cells may preferentially attach to certain areas within the scaffold based on pore size, shape, or the distribution of adhesive ligands, leading to a non-uniform distribution of cells within the material. Shown in HUVECs in day 7.

4. Cell bridging: Over time, cells may span across pores, creating bridges that can give the appearance of smaller or less defined pore structures. Shown in fibroblast day 12.

These cellular behaviours are critical considerations in scaffold design for tissue engineering, as they influence not only the mechanical properties of the scaffold but also the transport of nutrients and waste, cell signalling, and ultimately the success of tissue formation.

8.3 Dual freeze-drying crosslinking GelMA/PEGDA

Building upon our foundational work with gelatin and PEGDA hydrogels, this research has progressed to explore the properties of GelMA (Gelatin methacryloyl) in combination with PEGDA. GelMA is well-known for its improved bioactivity and photo-crosslinking abilities. When combined with PEGDA, it is expected to produce hydrogels featuring enhanced mechanical strength and adjustable physical properties. This novel blend aims to leverage GelMA's cell-friendly features and PEGDA's structural support to create a biomaterial that could potentially offer improved outcomes in tissue engineering applications.

The forthcoming study will mirror the methodological framework established in our initial gelatin-PEGDA investigations, applying similar cell viability and morphology assays. By conducting a parallel study with GelMA-PEGDA hydrogels, the research aims to draw comparative conclusions about the material's performance in supporting various cell types, including osteosarcoma and fibroblast cells. This research will be instrumental in determining the suitability of GelMA-PEGDA hydrogels for clinical applications, such as bone regeneration and cancer research, and in guiding the development of next-generation biomaterials.

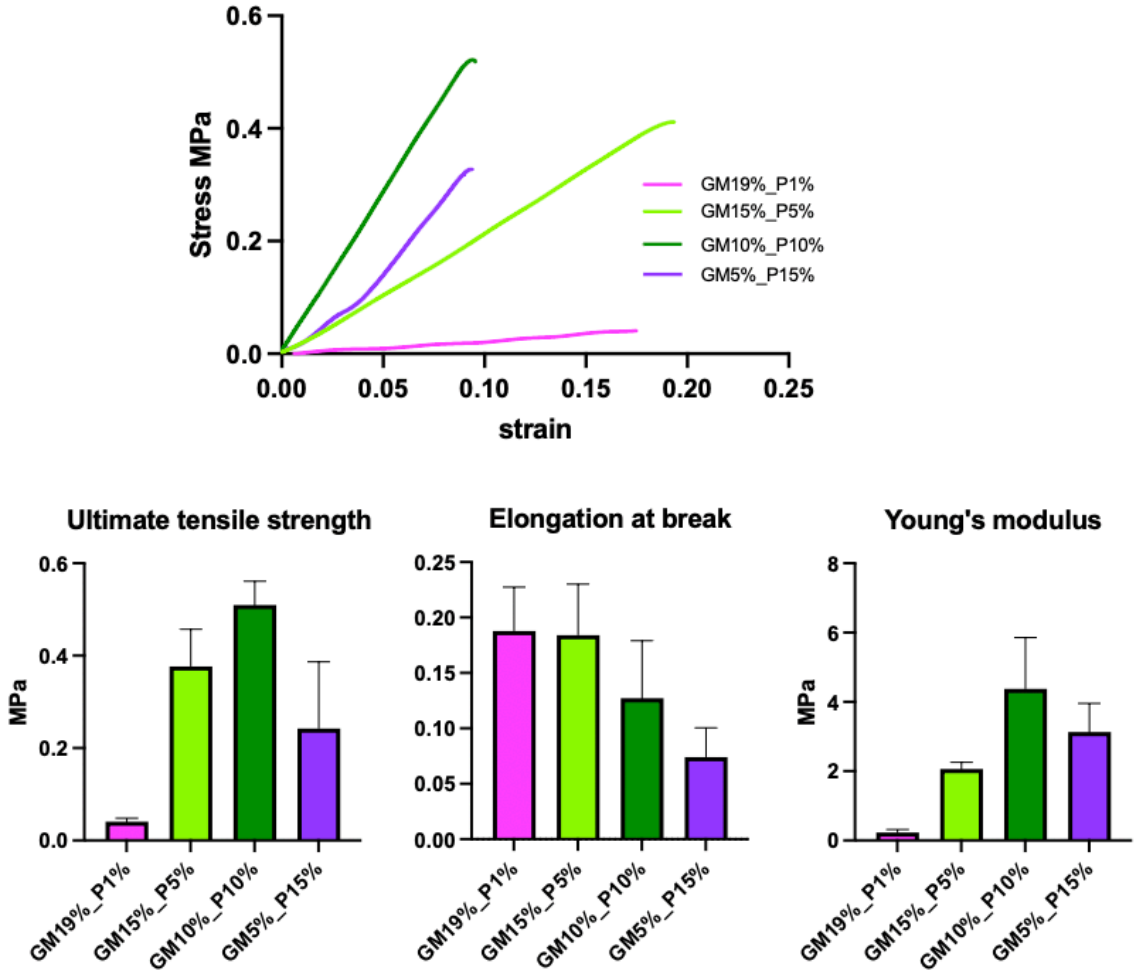

Figure 51 The mechanical analysis of hydrogel formulations composed GelMA and PEGDA at varying concentrations.

The figure presents a mechanical analysis of hydrogel formulations composed GelMA and PEGDA at varying concentrations. The upper panel depicts stress-strain curves, while the lower panel provides bar graphs for ultimate tensile strength, elongation at break, and Young's modulus for each formulation. From the stress-strain curves, it is evident that the GelMA-PEGDA hydrogels exhibit distinct mechanical behaviours under tensile loading. The GM19%_P1% formulation demonstrates minimal strain before rupture, indicative of a brittle material. In contrast, the GM5%_P15% composition shows significantly greater elasticity, as evidenced by the higher strain values at failure. The ultimate tensile strength (UTS) bar graph reveals that the GM19%_P1% hydrogel possesses the lowest UTS, while the GM15%_P5% and GM10%_P10% group exhibit a marked increase in tensile strength. Notably, the GM5%_P15% composition, despite its enhanced elasticity, presents a decrease in UTS compared to GM15%_P5% and GM10%_P10%, suggesting a trade-off between elasticity and tensile strength. Elongation at break data further corroborate these findings, with the GM19%_P1% showing the least elongation, and the GM5%_P15% exhibiting the highest, consistent with its elastic nature. The intermediate formulations (GM15%_P5% and GM10%_P10%) display moderate

elongation capabilities. Lastly, Young's modulus, a measure of stiffness, is highest for the GM15%_P5% hydrogel and decreases for hydrogels with higher PEGDA content. The GM5%_P15% hydrogel exhibits the lowest Young's modulus, aligning with its more elastic behaviour.

In summary, the mechanical properties of GelMA-PEGDA hydrogels are highly dependent on the specific ratios of the two components. A higher GelMA concentration tends to result in increased stiffness and tensile strength, while higher PEGDA content confers greater elasticity but at the cost of reduced tensile strength.

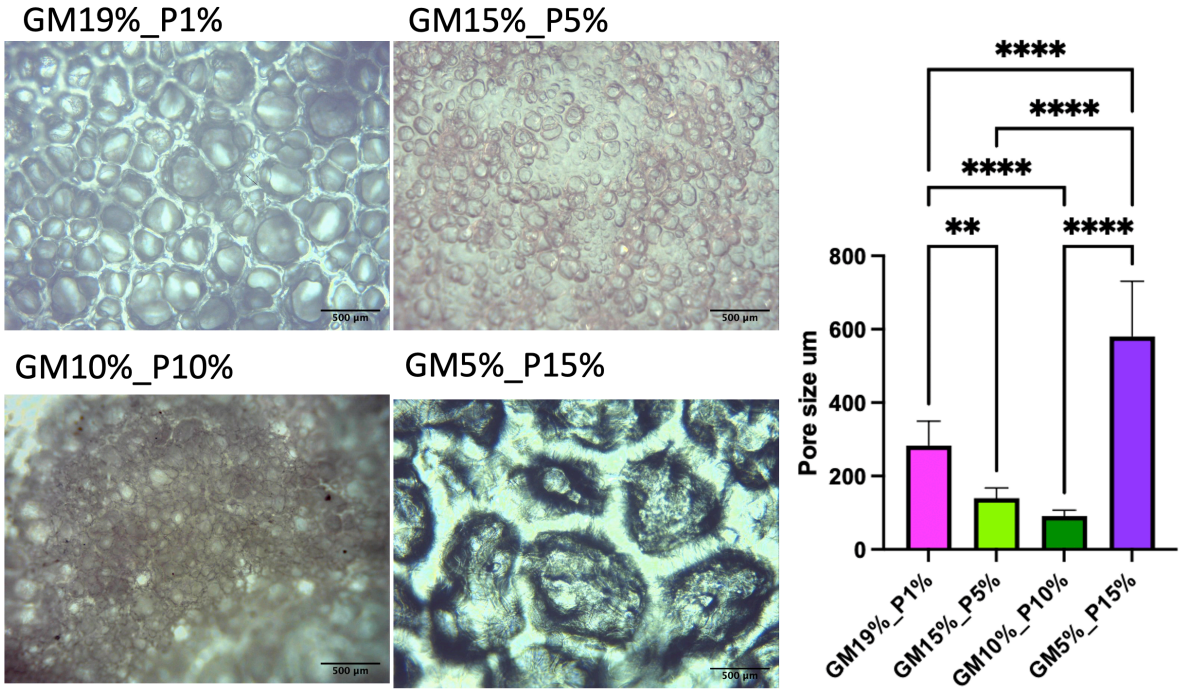

Figure 52 The porous structures of hydrogels formulated with different concentrations of GelMA and PEGDA, as observed under optical microscopy.

The figure presents a comparative analysis of the porous structures of hydrogels formulated with different concentrations of GelMA and PEGDA, as observed under optical microscopy. The right panel of the figure displays a bar chart quantifying the average pore sizes within each hydrogel composition. Observation under optical microscopy reveals that the GM19%_P1% hydrogel exhibits a highly porous network with relatively uniform pore distribution. In contrast, the GM15%_P5% sample shows less defined porosity with smaller and more irregular pore shapes. The GM10%_P10% composition has a more closed network with significantly reduced visible porosity, whereas the GM5%_P15% hydrogel presents a markedly different structure with large, well-defined pores. The quantitative analysis aligns with these observations, where the GM5%_P15% hydrogel exhibits the largest average pore size, substantially greater than the other formulations, as denoted by the tallest bar in the graph. This is in stark contrast to the GM19%_P1% and GM15%_P5% hydrogels, which

demonstrate significantly smaller pore sizes. Statistical analysis reveals that the differences in pore sizes between these formulations are highly significant, with p-values indicating a less than 0.01% probability that these differences are due to random chance (**p<0.01; ****p<0.0001).

These structural variations are critical as the pore architecture of hydrogels directly influences their mechanical properties and their potential for cellular infiltration, nutrient diffusion, and waste removal in tissue engineering applications. The GM5%_P15% hydrogel, with its larger pores, could be particularly suited for applications requiring rapid cell migration and extensive extracellular matrix deposition. Conversely, the smaller-pored hydrogels may be more appropriate for applications demanding a finer control over cell and nutrient distribution. In summary, the GelMA-PEGDA hydrogels display a range of pore structures that are highly dependent on the specific ratios of GelMA to PEGDA. The tunability of pore size through the adjustment of these ratios suggests the potential for customising hydrogel scaffolds to meet the requirements of various biomedical applications, from tissue engineering to controlled drug release systems.

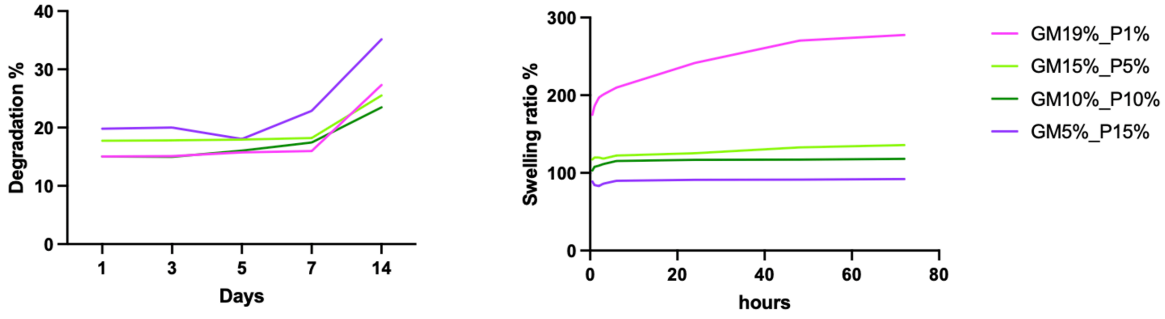

Figure 53 Degradation percentage, and swelling ratio, for GelMA and PEGDA at different concentrations.

The figure provides two critical physical properties, degradation percentage, and swelling ratio, for GelMA and PEGDA at different concentrations. The degradation graph demonstrates the temporal stability of the hydrogels. It reveals that the GM19%_P1% hydrogel exhibits a relatively stable profile with the least degradation over 14 days, indicating a potential for long-term applications. The GM5%_P15% hydrogel, however, shows a marked increase in degradation, particularly after day 7, suggesting a less stable network that might be more suitable for applications where faster material resorption is desired. The swelling ratio graph delineates the capacity of hydrogels to absorb water. The steep increase in the swelling ratio for the GM19%_P1% hydrogel within the initial hours indicates a rapid water uptake, which plateaus thereafter, signifying the saturation point. The other hydrogels exhibit more moderate swelling behaviours, with the GM5%_P15% hydrogel showing a gradual and consistent increase over the duration of the test, which could correlate with the higher degradation observed, possibly due to its higher water content facilitating the hydrolytic process. In summary, the GelMA-PEGDA hydrogels' mechanical stability

and water absorption capability are highly dependent on their composition ratios. The GM19%_P1% hydrogel presents characteristics suitable for applications requiring minimal swelling and slow degradation. In contrast, the GM5%_P15% hydrogel's higher swelling and faster degradation rates may be advantageous in scenarios where quicker material turnover is beneficial. These findings illustrate the importance of material composition in designing hydrogels for specific biomedical applications, with the potential to tailor these properties according to the desired rates of swelling and degradation.

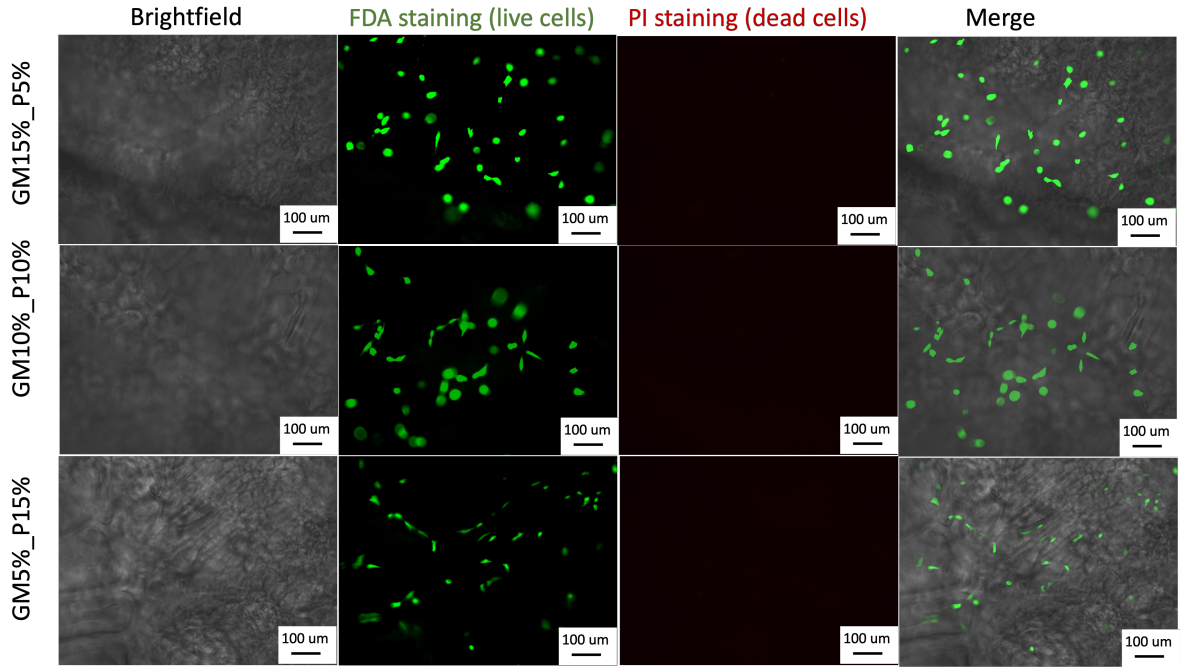

Figure 54 HUVECs seeded in GelMA-PEGDA after day 3

The series of micrographs displays endothelial cells following a three-day incubation period on GelMA-PEGDA hydrogel scaffolds with varying concentrations. The images capture the early cell-scaffold interactions, critical for assessing the biocompatibility and cellular response to the materials. Brightfield images reveal the scaffold morphology, offering a background context for cellular behaviour. FDA staining highlights viable cells in bright green, indicating metabolic activity, while PI staining marks non-viable cells in red, signalling compromised membrane integrity.

In the G15%_P5% group, endothelial cells are sparsely distributed, with the FDA staining showing isolated clusters of viable cells and no significant PI staining, indicating low cell mortality. The cells appear to maintain their characteristic morphology, suggesting that the scaffold provides a suitable environment for endothelial cell attachment and viability at this stage. The G10%_P10% group shows a similar pattern of viable cell distribution with a slightly higher density of cells, and again, negligible PI staining is observed. This suggests that the material supports a healthy cellular

environment conducive to endothelial cell survival. The G5%_P15% scaffold exhibits the least amount of visible cell attachment, as indicated by the sparse presence of FDA-positive cells. Notably, this composition displays no PI staining, suggesting that while cell attachment may be lower, the cells that do adhere remain viable.

In conclusion, the endothelial cells demonstrate viability across all GelMA-PEGDA hydrogel compositions after three days of culture, with variations in cell attachment and density that could be attributed to differences in hydrogel composition. These preliminary findings suggest that all tested hydrogel formulations provide a non-toxic environment for endothelial cell culture. Further analysis is needed to investigate cell proliferation, morphology, and functionality over a longer culture period to fully understand the potential of these hydrogels for vascular tissue engineering applications.

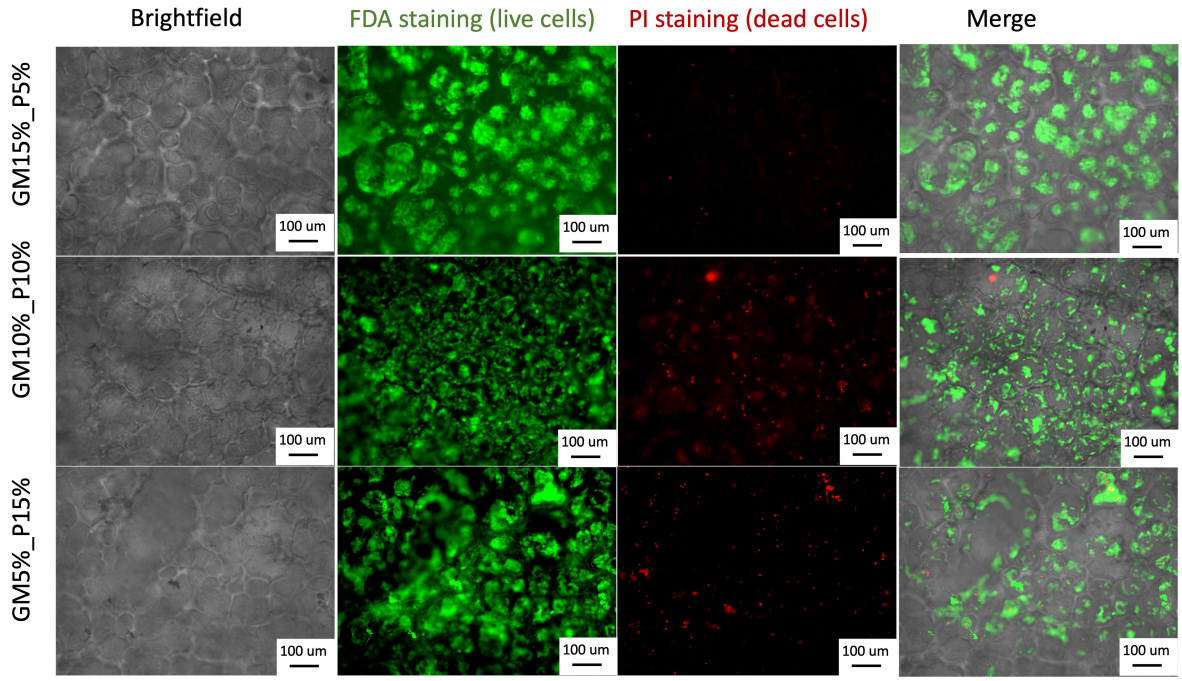

Figure 55 HOSs seeded in GelMA-PEGDA after day 3

The image series provides a visual assessment of human osteosarcoma (HOS) cells after three days of culture on GelMA-PEGDA hydrogel scaffolds with different compositions. The brightfield images offer a view of the hydrogel morphology, while the fluorescent staining provides insights into cell viability: FDA for live cells in green and PI for dead cells in red. The merged images integrate both sets of data, revealing the overall cell distribution and viability. For the G15%_P5% hydrogel, the FDA staining shows a uniform presence of live cells, with minimal PI staining, suggesting high viability and uniform cell distribution across the scaffold. The cells appear to be well-adhered and distributed, with the hydrogel providing a supportive environment for HOS cell growth. The G10%_P10% composition reveals a dense population of live HOS cells, as indicated by the widespread green fluorescence. The

presence of red-stained cells is more pronounced than in the G15%_P5% sample, indicating some cell mortality. However, the majority of cells are viable, displaying healthy cell-matrix interactions within the scaffold. In contrast, the G5%_P15% hydrogel exhibits less green fluorescence, indicating a sparser population of live cells. The PI staining suggests a higher degree of cell death, which could be attributed to less favourable cell-material interactions or potentially to the mechanical properties of the scaffold that may not be optimal for HOS cell attachment and proliferation. The merged images for the G5%_P15% scaffold show significant areas without green fluorescence, corroborating the observation of lower cell density and suggesting that this composition may be suboptimal for supporting HOS cell growth compared to the other hydrogel formulations.

In summary, the GelMA-PEGDA hydrogel demonstrates varying degrees of support for HOS cell culture over a three-day period, with the G15%_P5% and G10%_P10% scaffolds showing more favourable outcomes in terms of cell viability and distribution. The G5%_P15% scaffold, with a higher PEGDA content, appears to be less conducive to cell survival. These findings underscore the importance of optimising hydrogel composition to improve cell viability and suggest potential avenues for enhancing material properties to support osteosarcoma cell culture and bone tissue engineering applications. Further studies are required to elucidate the specific interactions between HOS cells and the hydrogel scaffolds to optimise cell growth and functionality.

Expanding upon our exploratory research into the biocompatibility and mechanical properties of GelMA-PEGDA hydrogels, we embarked on a longitudinal study to monitor the morphology and behaviour of self-fluorescent red fibroblasts over an extended period of 12 days. Fibroblasts, key players in tissue regeneration, provide a model system to evaluate the interaction between cellular processes and scaffold environments. The inherent red fluorescence of these cells affords continuous, non-invasive observation of cell morphology, allowing for real-time monitoring without the need for exogenous staining that could interfere with cellular function. This study aims to deepen our understanding of the dynamic relationship between fibroblast activity and the GelMA-PEGDA scaffold, which is crucial for the development of advanced biomaterials tailored for regenerative medicine and tissue engineering applications. The findings will contribute valuable insights into scaffold design parameters that support robust fibroblast function and long-term cell viability.

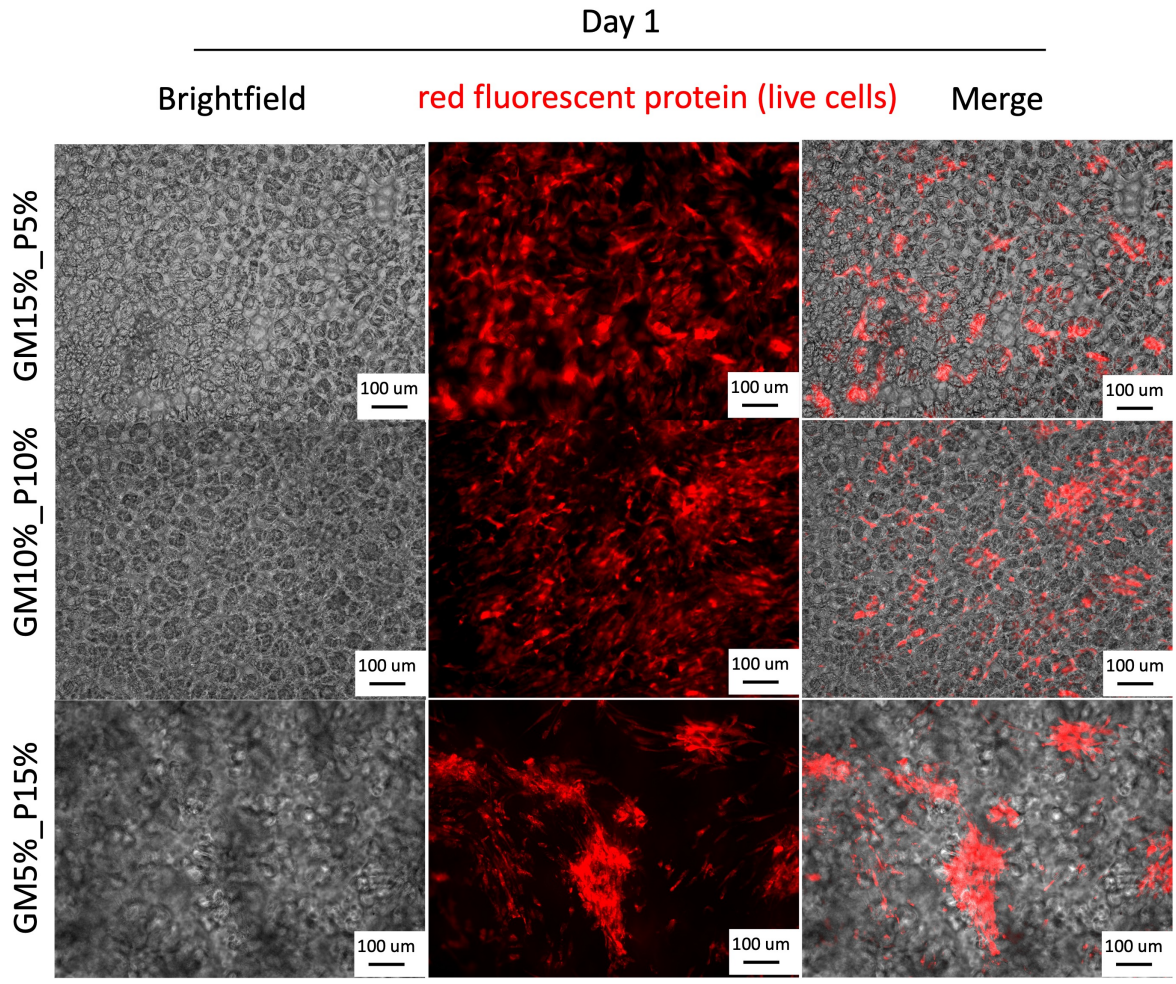

Figure 56 HDFs seeded in GelMA-PEGDA after day 1

The provided images offer a visual examination of fibroblast cells expressing red fluorescent protein (RFP), cultured on GelMA-PEGDA hydrogel scaffolds with varying compositions, captured on the first day of the experiment. In the G15%_P5% scaffold, a homogenous distribution of fibroblasts is evident, with the cells exhibiting strong red fluorescence, indicating robust viability. The cells appear to be uniformly adherent to the scaffold, which is suggestive of favourable initial cell-material interaction. The G10%_P10% hydrogel displays a similar pattern of cell attachment with live cells evenly distributed across the scaffold. The red fluorescence is less intense compared to the G15%_P5% scaffold, suggesting either a lower cell density or less intense RFP expression. For the G5%_P15% composition, the fibroblast cells show a more clustered pattern of attachment, with certain areas of higher cell density. The red fluorescence in this group is more intense in localised regions, indicating that while cell attachment occurs, it may not be as evenly distributed as in the other hydrogel formulations. The initial attachment of fibroblast cells across all GelMA-PEGDA hydrogel compositions is successful. The differences in cell distribution and fluorescence intensity may be

reflective of the varying degrees of cell affinity for each hydrogel type, influenced by the specific GelMA to PEGDA ratios.

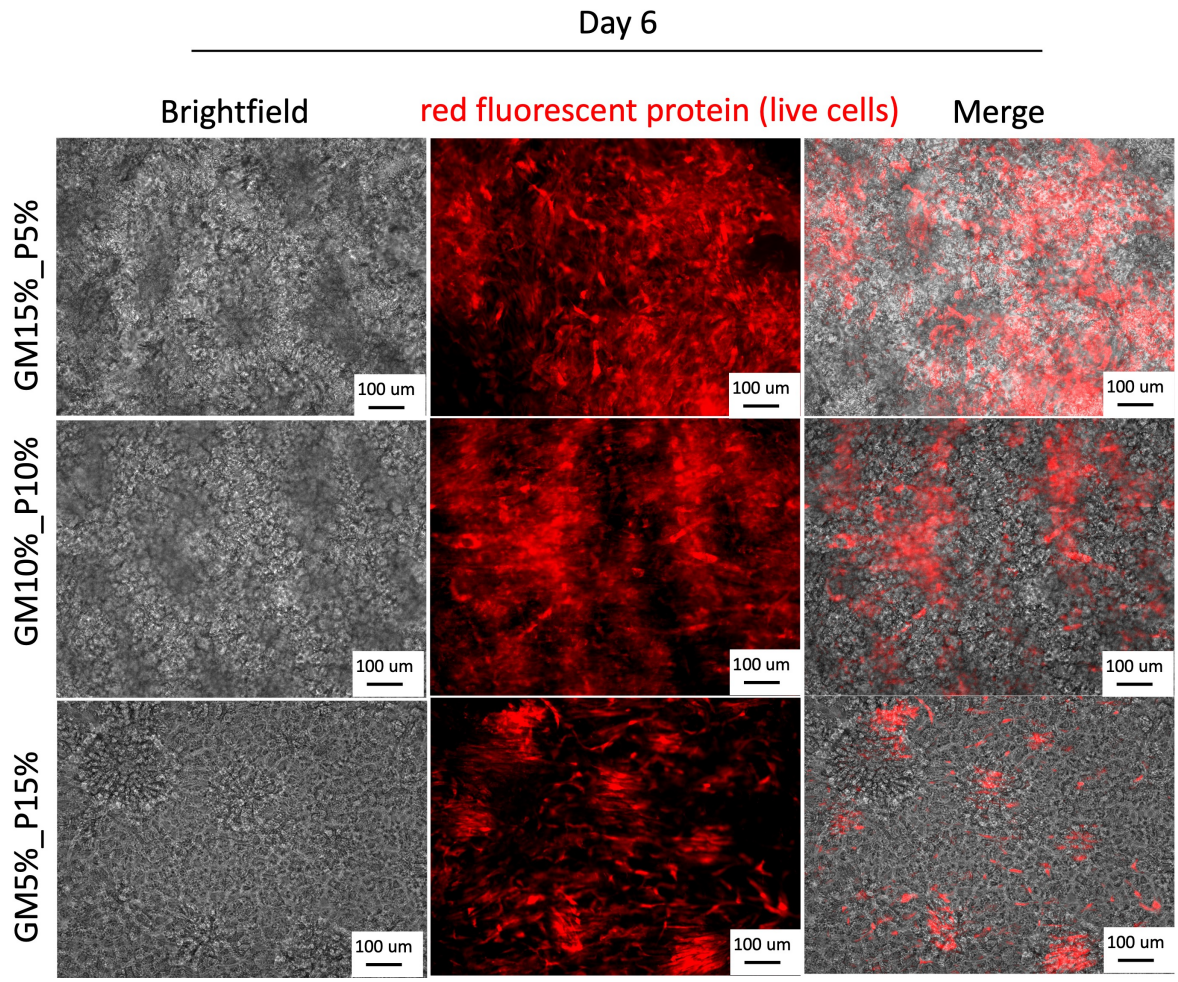

Figure 57 HDF seeded in GelMA-PEGDA after day 6

After 6 days culturing, fibroblast numbers increased in all groups. In the G15%_P5% scaffold, fibroblast cells exhibit a dispersed distribution, with individual cells and small clusters clearly visible in the red fluorescent images. The merged view suggests that the cells are well-integrated with the scaffold structure, which appears to support cell survival and maintain an open porosity that allows for cell-material interactions. The G10%_P10% hydrogel shows a more confluent layer of fibroblasts, indicating higher cell proliferation compared to the G15%_P5% composition. The cells display a network of connectivity, and the red fluorescence suggests robust cellular activity. In the merged image, cells can be seen occupying the spaces within the hydrogel matrix, indicating a favourable environment for cell growth. For the G5%_P15% composition, the fluorescence images reveal a dense aggregation of cells, suggesting a potential preference for certain areas of the scaffold or a higher degree of cell clustering. The brightfield and merged images reveal that these clusters are localised, with areas of the scaffold exhibiting less cell coverage. The collection of images represents fibroblast cells tagged with red fluorescent protein, cultured on hydrogel scaffolds composed of GelMA and PEGDA, as observed

at the 12-day mark. The images provide a multi-faceted view of the cells and the scaffolds, combining brightfield and fluorescent modalities.

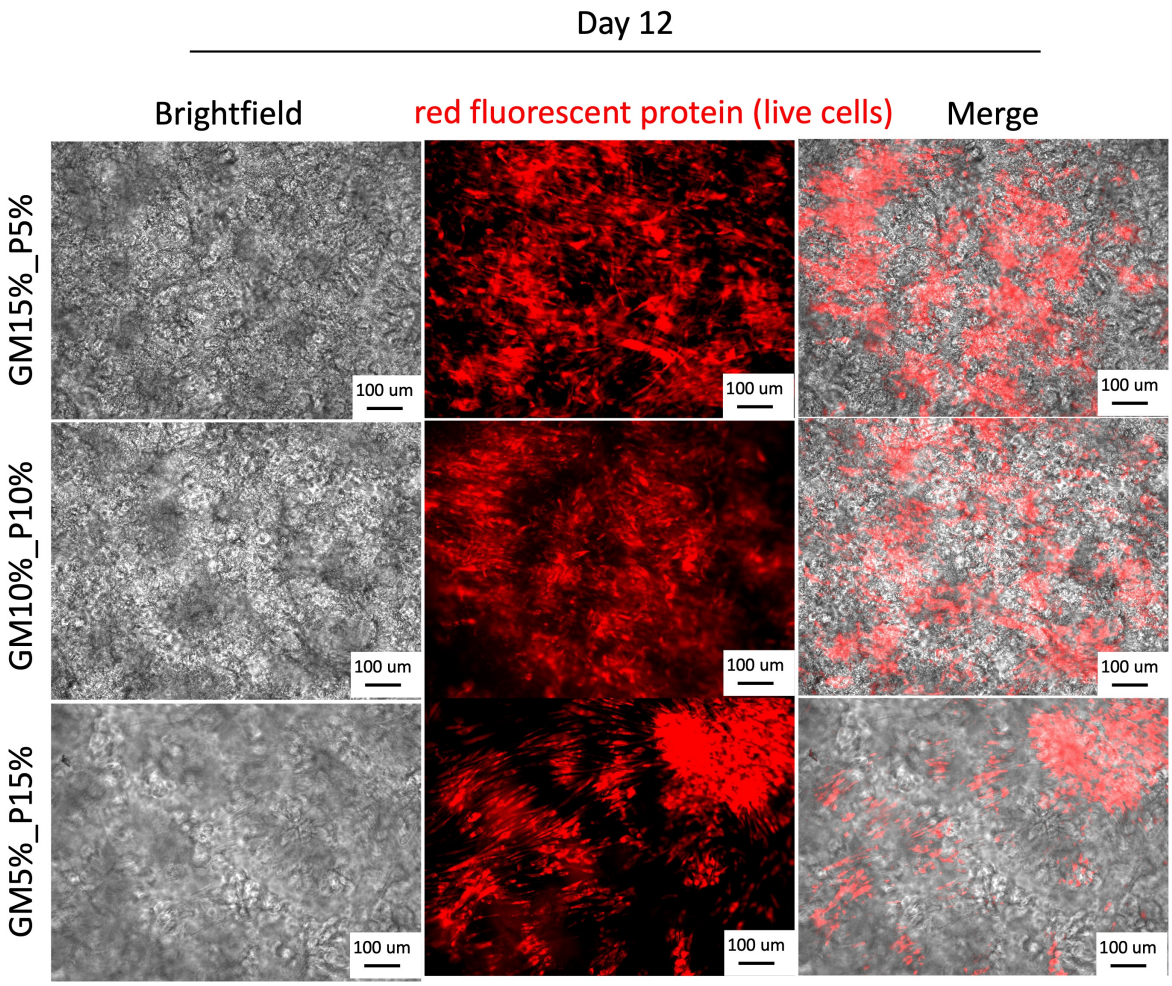

Figure 58 HDF seeded in GelMA-PEGDA after day 12

On day 12, the G15%_P5% scaffold exhibits a network of fibroblast cells, as indicated by the red fluorescence. The cells appear to be well-spread across the scaffold, with the red fluorescence indicating a mature and potentially interconnected cell network. The brightfield image shows that the scaffold maintains its integrity, and the merged image suggests good compatibility between the cells and this hydrogel composition. The G10%_P10% hydrogel shows a dense matrix of cells, with the fluorescence suggesting a high level of cellular activity. There is a homogeneous distribution of cells throughout the scaffold, and the merged image reveals that the cells are well integrated with the hydrogel, indicating a favourable environment for cell growth and matrix development. In the G5%_P15% sample, the fluorescence reveals a highly dense and perhaps overconfluent culture of fibroblasts, with cells exhibiting significant morphological changes. The brightfield image indicates that the scaffold structure is less distinct, potentially due to the overgrowth of cells. The merged image confirms the extensive coverage of the scaffold by the cells, which may indicate a highly permissive environment for fibroblast proliferation. These observations collectively suggest that the

GelMA/PEGDA hydrogel composition greatly influences fibroblast behaviour over time. The more balanced ratios (G15%_P5% and G10%_P10%) appear to provide a supportive environment for sustained cell growth and matrix formation. In contrast, the G5%_P15% scaffold, while supportive of cell proliferation, may lead to overly dense cell cultures which could impact the long-term functionality of the cells and the integrity of the scaffold. These findings have significant implications for the design of GelMA/PEGDA scaffolds in tissue engineering applications, emphasising the need to balance scaffold composition to achieve optimal cell growth and function.

8.4 Patent Published

(12) INTERNATIONAL APPLICATION PUBLISHED UNDER THE PATENT COOPERATION TREATY (PCT)

(19) World Intellectual Property Organization
International Bureau

(43) International Publication Date
13 February 2025 (13.02.2025)

WIPO | PCT

(10) International Publication Number
WO 2025/032337 A1

(51) International Patent Classification:
A61L 31/04 (2006.01) *A61L 31/14* (2006.01)

(21) International Application Number:
PCT/GB2024/052096

(22) International Filing Date:
08 August 2024 (08.08.2024)

(25) Filing Language: English

(26) Publication Language: English

(30) Priority Data:
2312148.6 08 August 2023 (08.08.2023) GB

(71) Applicant: **UNIVERSITY OF STRATHCLYDE** [GB/GB]; McCance Building , 16 Richmond Street, Glasgow G1 1XQ (GB).

(72) Inventors: **SHU, Wenmiao**; Department of Biomedical Engineering, University of Strathclyde, Wolfson Centre, 106 Rottenrow, Glasgow G4 0NW (GB). **WAN, Yifei**; Department of Biomedical Engineering, University of Strathclyde, Wolfson Centre, 106 Rottenrow, Glasgow G4 0NW (GB).

(74) Agent: **MARKS & CLERK LLP**; The Beacon, 176 St Vincent Street, Glasgow G2 5SG (GB).

(81) Designated States *(unless otherwise indicated, for every kind of national protection available)*: AE, AG, AL, AM, AO, AT, AU, AZ, BA, BB, BG, BH, BN, BR, BW, BY, BZ, CA, CH, CL, CN, CO, CR, CU, CV, CZ, DE, DJ, DK, DM, DO, DZ, EC, EE, EG, ES, FI, GB, GD, GE, GH, GM, GT, HN, HR, HU, ID, IL, IN, IQ, IR, IS, IT, JM, JO, JP, KE, KG, KH, KN, KP, KR, KW, KZ, LA, LC, LK, LR, LS, LU, LY, MA, MD, MG, MK, MN, MU, MW, MX, MY, MZ, NA, NG, NI, NO, NZ, OM, PA, PE, PG, PH, PL, PT, QA, RO, RS, RU, RW, SA, SC, SD, SE, SG, SK, SL, ST, SV, SY, TH, TJ, TM, TN, TR, TT, TZ, UA, UG, US, UZ, VC, VN, WS, ZA, ZM, ZW.

(84) Designated States *(unless otherwise indicated, for every kind of regional protection available)*: ARIPO (BW, CV, GH, GM, KE, LR, LS, MW, MZ, NA, RW, SC, SD, SL, ST, SZ, TZ, UG, ZM, ZW), Eurasian (AM, AZ, BY, KG, KZ, RU, TJ, TM), European (AL, AT, BE, BG, CH, CY, CZ, DE, DK, EE, ES, FI, FR, GB, GR, HR, HU, IE, IS, IT, LT, LU, LV, MC, ME, MK, MT, NL, NO, PL, PT, RO, RS, SE, SI, SK, SM, TR), OAPI (BF, BJ, CF, CG, CI, CM, GA, GN, GQ, GW, KM, ML, MR, NE, SN, TD, TG).

Published:
— *with international search report (Art. 21(3))*

(54) **Title:** METHOD FOR PREPARING A HYDROGEL

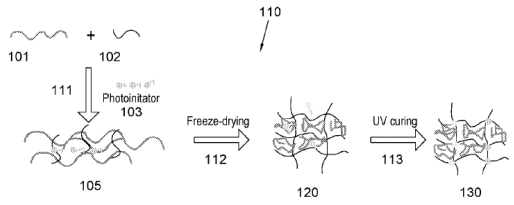

FIG. 1

(57) **Abstract:** A method of manufacturing a hydrogel comprises: (i) providing a polymerizable or crosslinkable hydrogel material (101,102); (ii) freeze-drying (112) the hydrogel material (105); and (iii) polymerizing or crosslinking (113) the hydrogel material (120) in solid state.

WO 2025/032337 A1

Bibliography

Aikaeli, F., Njim, T., Gissing, S., Moyo, F., Alam, U., Mfinanga, S.G., Okebe, J., Ramaiya, K., Webb, E.L., Jaffar, S., Garrib, A., 2022. Prevalence of microvascular and macrovascular complications of diabetes in newly diagnosed type 2 diabetes in low-and-middle-income countries: A systematic review and meta-analysis. PLOS Glob Public Health 2, e0000599. https://doi.org/10.1371/journal.pgph.0000599

Amini, M., Zayeri, F., Salehi, M., 2021. Trend analysis of cardiovascular disease mortality, incidence, and mortality-to-incidence ratio: results from global burden of disease study 2017. BMC Public Health 21, 401. https://doi.org/10.1186/s12889-021-10429-0

Amiri Heydari, H., Kazemi Ashtiani, M., Mostafaei, F., Alipour Choshali, M., Shiravandi, A., Rajabi, S., Daemi, H., 2024. Functional Efficacy of Tissue-Engineered Small-Diameter Nanofibrous Polyurethane Vascular Grafts Surface-Modified by Methacrylated Sulfated Alginate in the Rat Abdominal Aorta. ACS Appl. Mater. Interfaces 16, 67255–67274. https://doi.org/10.1021/acsami.4c13925

Andreazza, R., Morales, A., Pieniz, S., Labidi, J., 2023. Gelatin-Based Hydrogels: Potential Biomaterials for Remediation. Polymers 15, 1026. https://doi.org/10.3390/polym15041026

Barrulas, R.V., Corvo, M.C., 2023. Rheology in Product Development: An Insight into 3D Printing of Hydrogels and Aerogels. Gels 9, 986. https://doi.org/10.3390/gels9120986

Bergmeister, H., Schreiber, C., Grasl, C., Walter, I., Plasenzotti, R., Stoiber, M., Bernhard, D., Schima, H., 2013. Healing characteristics of electrospun polyurethane grafts with various porosities. Acta Biomaterialia 9, 6032–6040. https://doi.org/10.1016/j.actbio.2012.12.009

Bertassoni, L.E., Cecconi, M., Manoharan, V., Nikkhah, M., Hjortnaes, J., Cristino, A.L., Barabaschi, G., Demarchi, D., Dokmeci, M.R., Yang, Y., Khademhosseini, A., 2014. Hydrogel bioprinted microchannel networks for vascularization of tissue engineering constructs. Lab Chip 14, 2202–2211. https://doi.org/10.1039/C4LC00030G

Chan, B.P., Leong, K.W., 2008. Scaffolding in tissue engineering: general approaches and tissue-specific considerations. Eur Spine J 17, 467–479. https://doi.org/10.1007/s00586-008-0745-3

Chen, Z., Hu, X., Lin, Z., Mao, H., Qiu, Z., Xiang, K., Ke, T., Li, L., Lu, L., Xiao, L., 2023. Layered GelMA/PEGDA Hydrogel Microneedle Patch as an Intradermal Delivery System for Hypertrophic Scar Treatment. ACS Appl. Mater. Interfaces 15, 43309–43320. https://doi.org/10.1021/acsami.3c06800

Cheng, X., Chen, Q., Ren, Q., Ma, H., Zhao, Y., Jiao, S., 2024. Total cerebral small vessel disease burden and stroke outcomes in large vessel occlusion stroke receiving endovascular treatment: A systematic review and meta-analysis. Journal of Clinical Neuroscience 123, 179–185. https://doi.org/10.1016/j.jocn.2024.04.003

Cui, H., Zhu, W., Huang, Y., Liu, C., Yu, Z.-X., Nowicki, M., Miao, S., Cheng, Y., Zhou, X., Lee, S.-J., Zhou, Y., Wang, S., Mohiuddin, M., Horvath, K., Zhang, L.G., 2019. *In vitro* and *in vivo* evaluation of 3D bioprinted small-diameter vasculature with smooth muscle and endothelium. Biofabrication 12, 015004. https://doi.org/10.1088/1758-5090/ab402c

Ding, H., Hou, X., Gao, Z., Guo, Y., Liao, B., Wan, J., 2024. Challenges and Strategies for Endothelializing Decellularized Small-Diameter Tissue-Engineered Vessel Grafts. Adv Healthcare Materials 13, 2304432. https://doi.org/10.1002/adhm.202304432

Dunn, K.W., Kamocka, M.M., McDonald, J.H., 2011. A practical guide to evaluating colocalization in biological microscopy. American Journal of Physiology-Cell Physiology 300, C723–C742. https://doi.org/10.1152/ajpcell.00462.2010

Echave, M.C., Burgo, L.S., Pedraz, J.L., Orive, G., 2017. Gelatin as Biomaterial for Tissue Engineering. CPD 23. https://doi.org/10.2174/0929867324666170511123101

Emslie, A.G., Bonner, F.T., Peck, L.G., 1958. Flow of a Viscous Liquid on a Rotating Disk. Journal of Applied Physics 29, 858–862. https://doi.org/10.1063/1.1723300
Fowler, M.J., 2008. Microvascular and Macrovascular Complications of Diabetes. Clinical Diabetes 26, 77–82. https://doi.org/10.2337/diaclin.26.2.77
Freeman, S., Ramos, R., Alexis Chando, P., Zhou, L., Reeser, K., Jin, S., Soman, P., Ye, K., 2019. A bioink blend for rotary 3D bioprinting tissue engineered small-diameter vascular constructs. Acta Biomaterialia 95, 152–164. https://doi.org/10.1016/j.actbio.2019.06.052
Fukunishi, T., Lui, C., Ong, C.S., Dunn, T., Xu, S., Smoot, C., Smalley, R., Harris, J., Gabriele, P., Santhanam, L., Lu, S., Hibino, N., 2022. Extruded poly (glycerol sebacate) and polyglycolic acid vascular graft forms a neoartery. J Tissue Eng Regen Med 16, 346–354. https://doi.org/10.1002/term.3282
Gao, G., Kim, H., Kim, B.S., Kong, J.S., Lee, J.Y., Park, B.W., Chae, S., Kim, J., Ban, K., Jang, J., Park, H.-J., Cho, D.-W., 2019. Tissue-engineering of vascular grafts containing endothelium and smooth-muscle using triple-coaxial cell printing. Applied Physics Reviews 6, 041402. https://doi.org/10.1063/1.5099306
Gao, Q., He, Y., Fu, J., Liu, A., Ma, L., 2015. Coaxial nozzle-assisted 3D bioprinting with built-in microchannels for nutrients delivery. Biomaterials 61, 203–215. https://doi.org/10.1016/j.biomaterials.2015.05.031
Ghanizadeh Tabriz, A., Mills, C.G., Mullins, J.J., Davies, J.A., Shu, W., 2017. Rapid Fabrication of Cell-Laden Alginate Hydrogel 3D Structures by Micro Dip-Coating. Front. Bioeng. Biotechnol. 5. https://doi.org/10.3389/fbioe.2017.00013
GhavamiNejad, A., Ashammakhi, N., Wu, X.Y., Khademhosseini, A., 2020. Crosslinking Strategies for 3D Bioprinting of Polymeric Hydrogels. Small, 无 16, 2002931. https://doi.org/10.1002/smll.202002931
Gong, W., Lei, D., Li, S., Huang, P., Qi, Q., Sun, Y., Zhang, Y., Wang, Z., You, Z., Ye, X., Zhao, Q., 2016. Hybrid small-diameter vascular grafts: Anti-expansion effect of electrospun poly ε-caprolactone on heparin-coated decellularized matrices. Biomaterials 76, 359–370. https://doi.org/10.1016/j.biomaterials.2015.10.066
Goudie, K.J., McCreath, S.J., Parkinson, J.A., Davidson, C.M., Liggat, J.J., 2023. Investigation of the influence of pH on the properties and morphology of gelatin hydrogels. Journal of Polymer Science 61, 2316–2332. https://doi.org/10.1002/pol.20230141
Guarino, V., Alvarez-Perez, M.A., Borriello, A., Napolitano, T., Ambrosio, L., 2013. Conductive PANi/PEGDA Macroporous Hydrogels For Nerve Regeneration. Adv Healthcare Materials 2, 218–227. https://doi.org/10.1002/adhm.201200152
Hasan, A., Memic, A., Annabi, N., Hossain, M., Paul, A., Dokmeci, M.R., Dehghani, F., Khademhosseini, A., 2014. Electrospun scaffolds for tissue engineering of vascular grafts. Acta Biomaterialia 10, 11–25. https://doi.org/10.1016/j.actbio.2013.08.022
Jiang, Y.-C., Jiang, L., Huang, A., Wang, X.-F., Li, Q., Turng, L.-S., 2017. Electrospun polycaprolactone/gelatin composites with enhanced cell–matrix interactions as blood vessel endothelial layer scaffolds. Materials Science and Engineering: C 71, 901–908. https://doi.org/10.1016/j.msec.2016.10.083
Khalili, A., Ahmad, M., 2015. A Review of Cell Adhesion Studies for Biomedical and Biological Applications. IJMS 16, 18149–18184. https://doi.org/10.3390/ijms160818149
Kolesky, D.B., Homan, K.A., Skylar-Scott, M.A., Lewis, J.A., 2016. Three-dimensional bioprinting of thick vascularized tissues. Proc. Natl. Acad. Sci. U.S.A. 113, 3179–3184. https://doi.org/10.1073/pnas.1521342113
Konig, G., McAllister, T.N., Dusserre, N., Garrido, S.A., Iyican, C., Marini, A., Fiorillo, A., Avila, H., Wystrychowski, W., Zagalski, K., Maruszewski, M., Jones, A.L., Cierpka, L., De La Fuente, L.M., L'Heureux, N., 2009. Mechanical properties of completely autologous human tissue engineered blood vessels compared to human saphenous vein and

mammary artery. Biomaterials 30, 1542–1550. https://doi.org/10.1016/j.biomaterials.2008.11.011
Langer, R., Vacanti, J.P., 1993. Tissue Engineering. Science 260, 920–926. https://doi.org/10.1126/science.8493529
Liu, W., Heinrich, M.A., Zhou, Y., Akpek, A., Hu, N., Liu, X., Guan, X., Zhong, Z., Jin, X., Khademhosseini, A., Zhang, Y.S., 2017. Extrusion Bioprinting of Shear-Thinning Gelatin Methacryloyl Bioinks. Adv Healthcare Materials 6, 1601451. https://doi.org/10.1002/adhm.201601451
Liu, Y., Cheong Ng, S., Yu, J., Tsai, W.-B., 2019. Modification and crosslinking of gelatin-based biomaterials as tissue adhesives. Colloids and Surfaces B: Biointerfaces 174, 316–323. https://doi.org/10.1016/j.colsurfb.2018.10.077
Lu, Q., Ganesan, K., Simionescu, D.T., Vyavahare, N.R., 2004. Novel porous aortic elastin and collagen scaffolds for tissue engineering. Biomaterials 25, 5227–5237. https://doi.org/10.1016/j.biomaterials.2003.12.019
Madaghiele, M., Salvatore, L., Demitri, C., Sannino, A., 2018. Fast synthesis of poly(ethylene glycol) diacrylate cryogels via UV irradiation. Materials Letters 218, 305–308. https://doi.org/10.1016/j.matlet.2018.02.048
Maillard, M., Bleyer, J., Andrieux, A.L., Boujlel, J., Coussot, P., 2016. Dip-coating of yield stress fluids. Physics of Fluids 28, 053102. https://doi.org/10.1063/1.4947473
Major, R., Wilczek, G., Więcek, J., Gawlikowski, M., Plutecka, H., Kasperkiewicz, K., Kot, M., Pomorska, M., Ostrowski, R., Kopernik, M., 2022. Hemocompatibile Thin Films Assessed under Blood Flow Shear Forces. Molecules 27, 5696. https://doi.org/10.3390/molecules27175696
Maleki, S., Shamloo, A., Kalantarnia, F., 2022. Tubular TPU/SF nanofibers covered with chitosan-based hydrogels as small-diameter vascular grafts with enhanced mechanical properties. Sci Rep 12, 6179. https://doi.org/10.1038/s41598-022-10264-2
Mamaghani, K.R., Naghib, S.M., Zahedi, A., Rahmanian, M., Mozafari, M., 2018. GelMa/PEGDA containing graphene oxide as an IPN hydrogel with superior mechanical performance. Materials Today: Proceedings 5, 15790–15799. https://doi.org/10.1016/j.matpr.2018.04.193
Mancuso, L., Gualerzi, A., Boschetti, F., Loy, F., Cao, G., 2014. Decellularized ovine arteries as small-diameter vascular grafts. Biomed. Mater. 9, 045011. https://doi.org/10.1088/1748-6041/9/4/045011
Montini-Ballarin, F., Calvo, D., Caracciolo, P.C., Rojo, F., Frontini, P.M., Abraham, G.A., V. Guinea, G., 2016. Mechanical behavior of bilayered small-diameter nanofibrous structures as biomimetic vascular grafts. Journal of the Mechanical Behavior of Biomedical Materials 60, 220–233. https://doi.org/10.1016/j.jmbbm.2016.01.025
Norotte, C., Marga, F.S., Niklason, L.E., Forgacs, G., 2009. Scaffold-free vascular tissue engineering using bioprinting. Biomaterials 30, 5910–5917. https://doi.org/10.1016/j.biomaterials.2009.06.034
Pinter, D., Enzinger, C., Fazekas, F., 2015. Cerebral small vessel disease, cognitive reserve and cognitive dysfunction. J Neurol 262, 2411–2419. https://doi.org/10.1007/s00415-015-7776-6
Piszko, P., Kryszak, B., Szustakiewicz, K., 2022. Influence of cross-linking time on physico-chemical and mechanical properties of bulk poly(glycerol sebacate). Acta Bioeng Biomech 24. https://doi.org/10.37190/ABB-02208-2023-04
Quéré, D., 1999. FLUID COATING ON A FIBER. Annu. Rev. Fluid Mech. 31, 347–384. https://doi.org/10.1146/annurev.fluid.31.1.347
Radke, D., Jia, W., Sharma, D., Fena, K., Wang, G., Goldman, J., Zhao, F., 2018. Tissue Engineering at the Blood-Contacting Surface: A Review of Challenges and Strategies in

Vascular Graft Development. Adv Healthcare Materials 7, 1701461. https://doi.org/10.1002/adhm.201701461
Ren, X., Feng, Y., Guo, J., Wang, H., Li, Q., Yang, J., Hao, X., Lv, J., Ma, N., Li, W., 2015. Surface modification and endothelialization of biomaterials as potential scaffolds for vascular tissue engineering applications. Chem. Soc. Rev. 44, 5680–5742. https://doi.org/10.1039/C4CS00483C
Rocha Neto, J.B.M., Copes, F., Chevallier, P., Vieira, R.S., Da Silva, J.V.L., Mantovani, D., Beppu, M.M., 2022. Polysaccharide-based layer-by-layer nanoarchitectonics with sulfated chitosan for tuning anti-thrombogenic properties. Colloids and Surfaces B: Biointerfaces 213, 112359. https://doi.org/10.1016/j.colsurfb.2022.112359
Schindelin, J., Arganda-Carreras, I., Frise, E., Kaynig, V., Longair, M., Pietzsch, T., Preibisch, S., Rueden, C., Saalfeld, S., Schmid, B., Tinevez, J.-Y., White, D.J., Hartenstein, V., Eliceiri, K., Tomancak, P., Cardona, A., 2012. Fiji: an open-source platform for biological-image analysis. Nat Methods 9, 676–682. https://doi.org/10.1038/nmeth.2019
Seifu, D.G., Purnama, A., Mequanint, K., Mantovani, D., 2013. Small-diameter vascular tissue engineering. Nat Rev Cardiol, 无 10, 410–421. https://doi.org/10.1038/nrcardio.2013.77
Seymour, A.J., Westerfield, A.D., Cornelius, V.C., Skylar-Scott, M.A., Heilshorn, S.C., 2022. Bioprinted microvasculature: progressing from structure to function. Biofabrication 14, 022002. https://doi.org/10.1088/1758-5090/ac4fb5
Shanjani, Y., Pan, C.C., Elomaa, L., Yang, Y., 2015. A novel bioprinting method and system for forming hybrid tissue engineering constructs. Biofabrication 7, 045008. https://doi.org/10.1088/1758-5090/7/4/045008
Skardal, A., Zhang, J., McCoard, L., Xu, X., Oottamasathien, S., Prestwich, G.D., 2010. Photocrosslinkable Hyaluronan-Gelatin Hydrogels for Two-Step Bioprinting. Tissue Engineering Part A 16, 2675–2685. https://doi.org/10.1089/ten.tea.2009.0798
Syedain, Z.H., Meier, L.A., Lahti, M.T., Johnson, S.L., Tranquillo, R.T., 2014. Implantation of Completely Biological Engineered Grafts Following Decellularization into the Sheep Femoral Artery. Tissue Engineering Part A 20, 1726–1734. https://doi.org/10.1089/ten.tea.2013.0550
Vlachopoulos, J., Polychronopoulos, N., 2011. Basic Concepts in Polymer Melt Rheology and Their Importance in Processing, in: Kontopoulou, M. (Ed.), Applied Polymer Rheology. Wiley, pp. 1–27. https://doi.org/10.1002/9781118140611.ch1
Wang, Z., Kumar, H., Tian, Z., Jin, X., Holzman, J.F., Menard, F., Kim, K., 2018. Visible Light Photoinitiation of Cell-Adhesive Gelatin Methacryloyl Hydrogels for Stereolithography 3D Bioprinting. ACS Appl. Mater. Interfaces 10, 26859–26869. https://doi.org/10.1021/acsami.8b06607
Wang, Z., Zhang, M., Liu, L., Mithieux, S.M., Weiss, A.S., 2024. Polyglycerol sebacate-based elastomeric materials for arterial regeneration. J Biomedical Materials Res 112, 574–585. https://doi.org/10.1002/jbm.a.37583
Weinberg, C.B., Bell, E., 1986. A Blood Vessel Model Constructed from Collagen and Cultured Vascular Cells. Science 231, 397–400. https://doi.org/10.1126/science.2934816
Wilkens, C.A., Rivet, C.J., Akentjew, T.L., Alverio, J., Khoury, M., Acevedo, J.P., 2016. Layer-by-layer approach for a uniformed fabrication of a cell patterned vessel-like construct. Biofabrication 9, 015001. https://doi.org/10.1088/1758-5090/9/1/015001
Xu, L., Varkey, M., Jorgensen, A., Ju, J., Jin, Q., Park, J.H., Fu, Y., Zhang, G., Ke, D., Zhao, W., Hou, R., Atala, A., 2020. Bioprinting small diameter blood vessel constructs with an endothelial and smooth muscle cell bilayer in a single step. Biofabrication 12, 045012. https://doi.org/10.1088/1758-5090/aba2b6
Yang, L., Wang, X., Xiong, M., Liu, X., Luo, S., Luo, J., Wang, Y., 2024. Electrospun silk fibroin/fibrin vascular scaffold with superior mechanical properties and

biocompatibility for applications in tissue engineering. Sci Rep 14, 3942. https://doi.org/10.1038/s41598-024-54638-0
Yurdagul, A., Finney, A.C., Woolard, M.D., Orr, A.W., 2016. The arterial microenvironment: the where and why of atherosclerosis. Biochemical Journal 473, 1281–1295. https://doi.org/10.1042/BJ20150844
Zhang, Z., Salamatin, A., Peng, F., Kornev, K.G., 2022. Dip coating of cylinders with Newtonian fluids. Journal of Colloid and Interface Science 607, 502–513. https://doi.org/10.1016/j.jcis.2021.08.181
Zhao, D., Liu, J., Wang, M., Zhang, X., Zhou, M., 2019. Epidemiology of cardiovascular disease in China: current features and implications. Nat Rev Cardiol 16, 203–212. https://doi.org/10.1038/s41569-018-0119-4